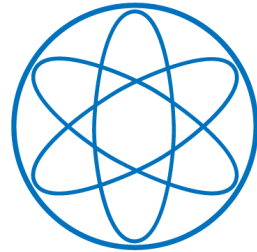


LEHRSTUHL E15
PHYSIK - DEPARTMENT



Identification of Cosmogenic
Background Signals in the
Neutrino Experiment Borexino

DIPLOMA THESIS

QUIRIN MEINDL
20TH OF FEBRUARY 2008



TECHNISCHE UNIVERSITÄT
MÜNCHEN

Abstract

The Borexino experiment is a 300 t liquid-scintillator detector designed for the real-time detection of solar neutrinos in the sub-MeV energy range. It is located at the underground site of the *Laboratori Nazionali del Gran Sasso* (LNGS) in Italy. As a result of the expected low signal rate of solar neutrinos, the design of the Borexino detector is based on the requirement of high radio-purity levels of the scintillator and construction material. In August 16th 2007, Borexino published the first real-time spectral measurement of ${}^7\text{Be}$ neutrinos ($47 \pm 7_{\text{stat}} \pm 12_{\text{sys}} \text{ counts day}^{-1} (100 \text{ t})^{-1}$) and proved its excellent capability to perform spectroscopy on solar neutrino fluxes.

Effort is currently directed to the determination of the remaining solar neutrino fluxes, i.e. from the pp and pep fusion processes, the three neutrino emissions of the CNO cycle as well as the low energy part of the ${}^8\text{B}$ branch. However, the detection of the high-energetic regions of the pep , CNO and ${}^8\text{B}$ neutrino spectra are affected by radionuclides induced by the residual atmospheric muon flux at the LNGS site. These muon-induced radionuclides form the so-called cosmogenic background in the Borexino experiment. Especially cosmogenic ${}^{11}\text{C}$ exceeds the expected signal of pep - and CNO - ν by an order of magnitude. Cosmogenic ${}^{10}\text{C}$ affects mainly the measurement of ${}^8\text{B}$ - ν .

The main part of this work is dedicated to the *Three-Fold-Coincidence* (TFC) technique, which is the only known method to reject the cosmogenic background caused by these two Carbon isotopes. Therefore, the efficiency of this method in the Borexino experiment is of great interest.

The TFC is based on the coincidence of muons and neutrons ejected from ${}^{12}\text{C}$ in the process of cosmogenic radionuclide production. By means of Borexino's offline data processing software *Echidna*, data taken by the detector is analyzed on correlations between the particles neutron, muon, and ${}^{11}\text{C}$. Each correlation contributes to an overall picture of the reliability of the TFC technique in Borexino. Neutron properties, like effective mean free path and mean capture time, as well as the ${}^{11}\text{C}$ decay time and production rates are objects of study. Also the reliability of the muon track reconstruction algorithm used in the analysis is tested by means of these correlations. However, data analysis is complicated by inefficiencies in reconstruction of muons and neutrons, as well as neutron detection. Furthermore,

artificial effects of data analysis have to be considered. Especially the time profile of ^{11}C with respect to neutrons and muons is significantly distorted. For this purpose, a model of the ^{11}C time profile is developed in this thesis, to correctly determine the decay time and total ^{11}C rate in Borexino on basis of the TFC technique.

For data analysis, it is essential that the data is taken by a calibrated and fully functional detector. In the frame of this work, a pulser system to monitor the electronics status of the *Outer Detector* (OD) has been constructed and implemented into the electronics read-out chain. The newly installed pulser system injects a reference signal into the OD electronics and thereby checks its operational reliability for each run. By now, this pulser system is an inherent part of calibration and maintenance work of the Borexino detector.

Contents

1	Introduction	1
1.1	Neutrinos within the Standard Model	1
1.2	Neutrinos beyond the Standard Model	2
1.2.1	Neutrino oscillations in vacuum	2
1.2.2	Neutrino oscillations in matter	4
1.2.3	Intrinsic neutrino parameters	4
1.3	The Sun as neutrino source	5
1.3.1	The Standard Solar Model	5
1.3.2	Fusion processes	6
1.3.3	Solar neutrino fluxes	8
1.4	Solar neutrino detectors	11
1.4.1	Radiochemical detectors	11
1.4.2	Cherenkov detectors	12
1.4.3	Liquid Scintillator detectors	14
2	The Borexino experiment	17
2.1	ν -detection principle	18
2.2	Physics goals	18
2.3	Detector design	20
2.3.1	The Inner Detector	20
2.3.2	The Outer Detector	23
2.4	First real time detection of ${}^7\text{Be}$ solar neutrinos	24
3	Data acquisition and structure	27
3.1	Trigger system	27
3.1.1	Main Trigger System	27
3.1.2	Analogue Neutron Trigger	28

3.2	Implementation of the Outer Detector pulser system	29
3.2.1	Outer Detector electronics	29
3.2.2	Pulser system installation	32
3.3	Echidna data structure	34
3.3.1	Event processing	34
3.3.2	Software parameters of analysis	35
4	Solar neutrino fluxes and cosmogenic background	41
4.1	The pp/pep , CNO and 8B solar neutrino fluxes	41
4.1.1	Physics goals	41
4.1.2	Signal and background sources	43
4.2	Cosmogenic radionuclide background	45
4.2.1	Muon beam experiment at CERN	45
4.3	The Three-fold Coincidence technique	47
4.3.1	Tagging of ${}^{11}C$ and ${}^{10}C$	47
4.3.2	Background suppression	48
4.4	Signatures of muons and neutron capture gammas within DAQ	49
4.4.1	Muons	49
4.4.2	Neutron capture gammas	53
5	Analysis and results	55
5.1	Data set preparation	56
5.2	Event selection	57
5.2.1	General criterion	57
5.2.2	Criteria for muon identification	57
5.2.3	Criterion for neutron / neutron capture γ identification	58
5.2.4	Criteria for radionuclide candidate identification	58
5.3	Neutron analysis	62
5.3.1	Neutron multiplicity	63
5.3.2	Nomenclature	65
5.3.3	Neutron rate	66
5.3.4	Badly reconstructed neutrons	66
5.3.5	Neutron energy	66
5.3.6	Spatial neutron-muon correlations	68
5.3.7	Neutron capture mean time	70

5.4	^{11}C analysis	72
5.4.1	^{11}C production channels	73
5.4.2	Correlations in the data analysis	74
5.4.3	Influence of DAQ deadtime	76
5.4.4	Model of the time profile	76
5.4.5	^{11}C -neutron correlations	84
5.4.6	Determination of ^{11}C rate with respect to neutron- ^{11}C distance	88
5.4.7	Spatial ^{11}C -muon correlations	93
5.4.8	Determination of ^{11}C rate with respect to muon- ^{11}C distance	96
5.4.9	Untaggable ^{11}C due to deadtime	98
5.4.10	Reduction of cosmogenic ^{11}C background	100
5.4.11	Discussion on efficiency of analysis	102
6	Prospective ^{10}C analysis	105
6.1	^{10}C production channels	105
6.2	Influence of DAQ deadtime	106
6.3	^{10}C signal and background	106
7	Summary, Outlook and Conclusion	109
7.1	Summary	109
7.2	Outlook	112
7.2.1	Neutron detection	112
7.2.2	Muon track reconstruction	112
7.3	Conclusion	113

Chapter 1

Introduction

For thousands of years, astronomy has relied on detecting electromagnetic radiation of celestial objects to gain information on the physics mechanism in our universe. However, since the famous Homestake experiment of Raymond Davis in the 1970's [1] (sec. 1.4.1), this science has expanded to the field of neutrino physics. Like photons, neutrinos are neutral particles, hence their propagation is not influenced by electromagnetic fields. They maintain their directional information and therefore point directly at the source of their production. As only weakly-interacting particles, neutrinos are barely affected by matter, in contrast to the electromagnetically interacting photons. Therefore, neutrino astronomy provides insight into the interior of several celestial phenomena, e.g. core-collapse supernovae (SN), the Sun, or even Earth itself.

The first measurement of solar electron neutrinos in the Homestake experiment showed less events than expected on basis of the *Solar Standard Model* (SSM). This so-called *Solar Neutrino Problem* (SNP) incited the field of neutrino physics, which has been growing ever since. Now, more than 30 years later, the generally accepted explanation for the detected neutrino deficit is based on intrinsic properties of the neutrino particle beyond the *Standard Model of particle physics* (SM). Neutrino-oscillations provide a consistent solution for the SNP and have been observed in a variety of experiments at different energy scales [2, 3, 4]. Besides being a probe for cosmic processes, the neutrino particle has been always subject of research itself.

1.1 Neutrinos within the Standard Model

In the *Standard Model of particle physics* (SM), leptons and antileptons are divided in three generations, with each generation consisting of a charged lepton and a neutrino of corresponding flavor.

$$\begin{pmatrix} \nu_e \\ e \end{pmatrix} \begin{pmatrix} \nu_\mu \\ \mu \end{pmatrix} \begin{pmatrix} \nu_\tau \\ \tau \end{pmatrix} \quad (1.1)$$

All leptons are subject to the weak interaction, while only the charged leptons also undergo electromagnetic interaction. Since neutrinos are neutral particles, they can solely interact via the weak interaction. The charged current (CC) and neutral current (NC) interactions are procured by the exchange bosons of the weak interaction, i.e. W^\pm and Z^0 bosons, which can only cause lepton conversion within the same generation. Therefore, the number of leptons within each generation is conserved (lepton flavor conservation). In consequence, the total number of leptons is also conserved.

Neutrinos maximally violate parity, and therefore are always in a pure chirality eigenstate, i.e. neutrinos are always left-handed, whereas anti-neutrinos are always right-handed. As a result, neutrinos are massless particles in the SM.

1.2 Neutrinos beyond the Standard Model

Ever since the Homestake experiment performed by Raymond Davis and his collaborators in 1970, solar neutrino experiments detected a deficit in the measured solar ν_e -signal rate compared to the expectation according to the *Standard Solar Model* (SSM). Besides this solar neutrino deficit, also a deficit in the atmospheric ν_μ -signal has been detected by the Super-Kamiokande experiment [5, 2].

Today, a well established explanation for these effects are neutrino-oscillations, i.e. the transition of neutrinos into different flavors ($\nu_e \leftrightarrow \nu_\mu$, $\nu_\mu \leftrightarrow \nu_\tau$, $\nu_e \leftrightarrow \nu_\tau$). All nuclear reactions in the Sun produce ν_e . These can be converted by neutrino-oscillations to $\nu_{\mu,\tau}$. As a result, the solar neutrino flux measured at the Earth is a composition of all three neutrino flavors. Thus, experiments which are most sensitive to ν_e detect a solar neutrino rate less than expected on the basis of absent neutrino-oscillations. Examples of solar neutrino experiments and their detection techniques are outlined in sec. 1.4.

1.2.1 Neutrino oscillations in vacuum

Neutrino flavor eigenstates $|\nu_\alpha\rangle$ ($\alpha = e, \mu, \tau$) can be expressed in the basis of neutrino mass eigenstates $|\nu_i\rangle$ ($i = 1, 2, 3$), which describe stationary solutions of the Schrödinger equation of free particles.

$$\begin{pmatrix} \nu_e \\ \nu_\mu \\ \nu_\tau \end{pmatrix} = \mathbb{U} \begin{pmatrix} \nu_1 \\ \nu_2 \\ \nu_3 \end{pmatrix} \quad (1.2)$$

\mathbb{U} is the unitary *Pontecorvo-Maki-Nakagawa-Sakata* (PMNS) matrix [6], describing the transformation between flavor and mass eigenstates of the neutrinos. The MNS matrix can be written as:

$$\begin{aligned} \mathbb{U} &= \begin{pmatrix} 1 & 0 & 0 \\ 0 & c_{23} & s_{23} \\ 0 & -s_{23} & c_{23} \end{pmatrix} \begin{pmatrix} c_{13} & 0 & s_{13}e^{-i\delta} \\ 0 & 1 & 0 \\ -s_{13}e^{-i\delta} & 0 & c_{13} \end{pmatrix} \begin{pmatrix} c_{12} & s_{12} & 0 \\ -s_{12} & c_{12} & 0 \\ 0 & 0 & 1 \end{pmatrix} \\ &= \begin{pmatrix} U_{e1} & U_{e2} & U_{e3} \\ U_{\mu1} & U_{\mu2} & U_{\mu3} \\ U_{\tau1} & U_{\tau2} & U_{\tau3} \end{pmatrix} \end{aligned} \quad (1.3)$$

In this expression, s_{ij} and c_{ij} stand for $\sin(\theta_{ij})$ and $\cos(\theta_{ij})$ respectively, with the rotation mixing angle θ_{ij} . δ is a possible CP-violating phase. The mass eigenstates of the neutrinos evolve in time according to:

$$|\nu_i\rangle = e^{-iE_i t} |\nu_i\rangle \quad (1.4)$$

Considering ultra-relativistic neutrinos, the energy can be approximated as:

$$E_i = \sqrt{p^2 + m_i^2} \approx E + \frac{m_i^2}{2E} \quad (1.5)$$

Taking a neutrino $|\nu(t)\rangle$ which is produced at time zero in the flavor eigenstate $|\nu_\alpha\rangle$, one can show on the basis of Equations 1.2 - 1.5, that the probability to find an arbitrary flavor eigenstate $|\nu_\beta\rangle$ is

$$P_{\alpha\beta}(t) = \sum_{ij} U_{\alpha i} U_{\alpha j}^* U_{\beta i}^* U_{\beta j} e^{-i(\frac{\Delta m_{ij}^2}{2E})t} \quad (1.6)$$

with $\Delta m_{ij}^2 = m_i^2 - m_j^2$. Considering only the simplified case of two-flavor oscillations between $|\nu_\alpha\rangle$ and $|\nu_\beta\rangle$, one gets an oscillation probability of:

$$P_{\alpha\beta}(t) = 1 - \sin^2(2\theta_{ij}) \cdot \sin^2\left(\frac{\Delta m_{ij}^2}{2E}t\right) \quad (1.7)$$

The probability to detect a given neutrino flavor oscillates in time, and also in space as a result of neutrino propagation ($v \approx c$; c denotes the speed of light). The probability, that a neutrino remains in the same eigenstate is the so-called ‘‘Survival probability’’ ($P_{\alpha\alpha}(t)$).

As one can easily see, the effect of neutrino oscillation is based on massive neutrinos of different masses ($\Delta m_{ij}^2 \neq 0$) as well as a rotation of neutrino flavor eigenstates with respect to the weak eigenstates ($\mathbb{U} \neq 1$).

1.2.2 Neutrino oscillations in matter

If neutrinos propagate in matter, their oscillation behavior is changed with respect to the vacuum oscillations due to the additional interaction with electrons. ν_e can interact with the electrons via CC and NC reactions, whereas ν_μ and ν_τ are only capable of NC interactions in matter. The additional interaction channel of ν_e introduces a phase difference relative to the $\nu_{\mu,\tau}$ and can be parameterized as an effective mass of the ν_e . The matter mass eigenstates of the neutrino are rotated with respect to the vacuum mass eigenstates. This can lead to a flavor conversion resonance effect in case of varying matter densities, enhancing the transition probability maximally. The effect was first pointed out by Mikheyev and Smirnov [7] on the basis of work performed by Wolfenstein [8].

This so-called Mikheyev-Smirnov-Wolfenstein (MSW) effect is one of the most attractive solutions of the SNP. ν_e 's created in the center of our Sun are subject to a slowly decreasing matter density on their way outwards and thus can be converted resonantly to ν_μ by the MSW effect. The effect is energy dependant and expected to contribute significantly for energies above $\sim 2 \text{ MeV}$. Its influence on the solar neutrino spectrum is illustrated in Figure 1.4 and described in sec. 1.3.3. For more detail on the MSW mechanism, see [9].

1.2.3 Intrinsic neutrino parameters

Neutrino oscillations have been investigated and proven in a variety of experiments [2, 3, 4]. Today, they are a well established phenomenon in neutrino physics. As a non-standard physics effects, these oscillations open the window to physics beyond the SM.

First of all, neutrino oscillations clearly violate lepton flavor conservation (see sec. 1.1). Also several intrinsic parameters arise on the basis of these oscillations, which are not covered by the SM. The neutrino mass eigenvalues m_i , the rotation mixing angles θ_{ij} and also a possible CP-violating phase δ are subject of neutrino physics. In addition, the non-vanishing neutrino masses give rise to the question on the nature of the neutrino: Is it a Majorana particle (i.e. a particle which is identical to its anti-particle) or a Dirac-particle? Neutrino oscillations provide an exceptional sensitive tool to determine the mass square difference Δm_{ij}^2 and the mixing angles.

Known oscillation parameters

The current best global values of the oscillation parameters [10] are:

$$\begin{aligned}
\Delta m_{21}^2 &= (8.0 \pm 0.3) \cdot 10^{-5} (eV)^2 \\
\sin^2(2\theta_{21}) &= 0.86^{+0.03}_{-0.04} \\
|\Delta m_{32}^2| &\in [1.9, 3.0] \cdot 10^{-3} (eV)^2 \\
\sin^2(2\theta_{32}) &> 0.92 \\
\sin^2(2\theta_{31}) &< 0.19
\end{aligned} \tag{1.8}$$

Vacuum neutrino oscillations are insensitive to the sign of Δm_{ij}^2 (see eq. 1.7), however, the MSW effect only occurs for $\Delta m_{21}^2 > 0$. As the most attractive solution of solar neutrino oscillations, a positive sign of Δm_{21}^2 is established. The sign of Δm_{32}^2 is still undetermined. Therefore, two possible hierarchies of neutrino mass eigenstates exist: The so-called normal hierarchy ($m_1 > m_2 > m_3$) and the inverted hierarchy ($m_3 > m_2 > m_1$).

1.3 The Sun as neutrino source

The detection of solar neutrinos in 1970 by the pioneering Homestake experiment (sec. 1.4.1) opened the field to neutrino astronomy. Ever since, the Sun has been object of neutrino astronomy. The neutrinos emitted in the fusion processes in our Sun are subject to vacuum oscillations and to the MSW effect. Solar neutrinos are therefore suited to study intrinsic properties of the neutrino particle. In addition the energy production mechanisms in the Sun itself are of great interest. This section provides an overview of the standard model of our Sun, and the production processes of solar neutrinos. Furthermore, the expected solar neutrino fluxes and the influence of neutrino oscillations are presented.

1.3.1 The Standard Solar Model

The *Standard Solar Model* (SSM) is the current best model to describe the structure, dynamic and evolution of the Sun. It is based on the following assumptions:

- **Thermonuclear energy production:**
Energy is produced in the Sun by fusion processes of Hydrogen to Helium. The specific fusion branches are described in more detail in sec. 1.3.2.
- **Energy transport:**
The energy generated in these fusion processes is transported within the solar plasma by radiation (photons and neutrinos), convection, and to a small extent heat conduction.

- **Thermal equilibrium:**

The Sun is expected to be in a quasi-steady state, with the power emitted on its surface being equal the power generated in its interior.

- **Hydrostatic equilibrium:**

In stable stars, the gravitational attraction of the stellar mass compensates the thermal pressure of the solar plasma.

These assumptions form a set of state equations which are iteratively solved within the boundary conditions of the measured solar parameters. These are: radius, surface temperature, luminosity, mass, age, opacities and fusion cross sections. On basis of this model, the fusion processes and their branching ratios can be predicted, as outlined in the next section.

1.3.2 Fusion processes

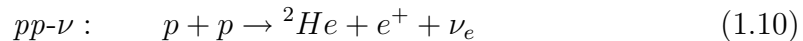
Energy production in a sun-like star is based on two reaction sequences, i.e. the pp chain and the CNO cycle. Both sequences result in the net reaction



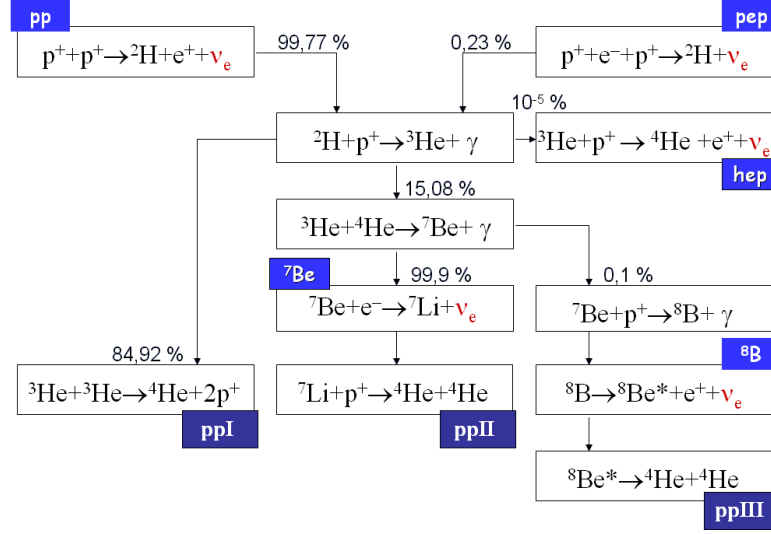
with a total energy release of 26.73 MeV . In our Sun, the pp chain accounts for about 98% of the total energy production, whereas the CNO cycle only makes up 2% of the total energy release. However, the CNO cycle is strongly temperature dependent and is the most dominant energy production process in heavy stars larger than a few solar masses. These reaction chains and the solar neutrinos they produce are outlined in the following.

pp chain

As one can see in Figure 1.1, there are two possible initial reactions for the pp sequence, both producing ν_e :



With respect to particle physics, both reactions are very similar and thus the ratio of their cross sections is known to a high theoretical accuracy. On basis of these initial reactions, several branches are possible in the further course of nuclear fusion, which are presented in Figure 1.1. Particular attention is given to


 Figure 1.1: Schematics of the pp chain [11].

the neutrino production process. Besides the pp and pep reactions, solar neutrinos are also created in the following processes:

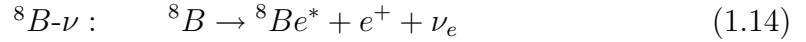
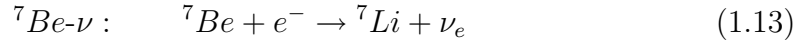
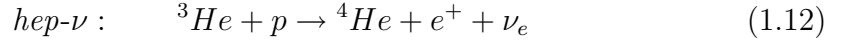
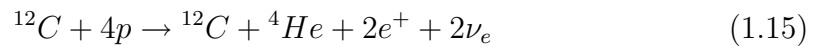


Table 1.1 presents the energies and expected fluxes of all solar neutrinos according to the SSM. In addition, the spectral shapes of these neutrino emission are shown in Figure 1.3.

***CNO* chain**

The *CNO* cycle is named after the participating elements in this reaction sequence: Carbon, Nitrogen and Oxygen. As shown in Figure 1.2, ${}^{12}\text{C}$ serves as a catalyst for the fusion of Hydrogen to Helium in the *CNO-I* cycle. The net reaction can be written as:



The *CNO* cycle is subject to a much higher Coulomb barrier than the pp chain, and therefore requires higher temperatures. At a temperature of $1.5 \cdot 10^7 \text{ K}$

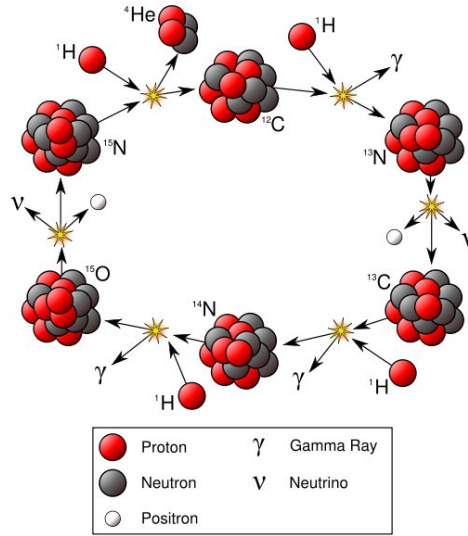


Figure 1.2: Schematics of the *CNO-I* cycle [11].

the *CNO* cycle only contributes about 2% to the total energy production in our Sun. However, due to its strong temperature dependence, the *CNO* cycle would already become the dominant energy production mechanism at temperatures above $\sim 1.8 \cdot 10^7 \text{ K}$. Thus, the *CNO* cycle is predominant in heavy stars. In the process of the *CNO-I* cycle, two neutrinos are emitted according to the reactions:

$$^{13}\text{N}-\nu : \quad ^{13}\text{N} \rightarrow ^{13}\text{C} + e^+ + \nu_e \quad (1.16)$$

$$^{15}\text{O}-\nu : \quad ^{15}\text{O} \rightarrow ^{15}\text{N} + e^+ + \nu_e \quad (1.17)$$

Besides the *CNO-I* cycle there exist also three additional sub-cycles which contribute only to a small extent to solar energy production. *CNO-II*, *CNO-III* and *CNO-IV* mainly contribute in heavy stars.

1.3.3 Solar neutrino fluxes

Neutrinos can only interact via the weak interaction and are therefore hardly affected by matter. As a result, they escape from the Sun ($R \approx 7 \cdot 10^5 \text{ km}$) nearly without interaction and can be detected at the Earth about 8 *min* after production (distance between Sun and Earth: $\sim 1.5 \cdot 10^8 \text{ km}$). Therefore, the detection of solar neutrinos provides a direct, undisturbed, and nearly instantaneous observation of the energy production processes in the center of the Sun. Photons take about 10^6

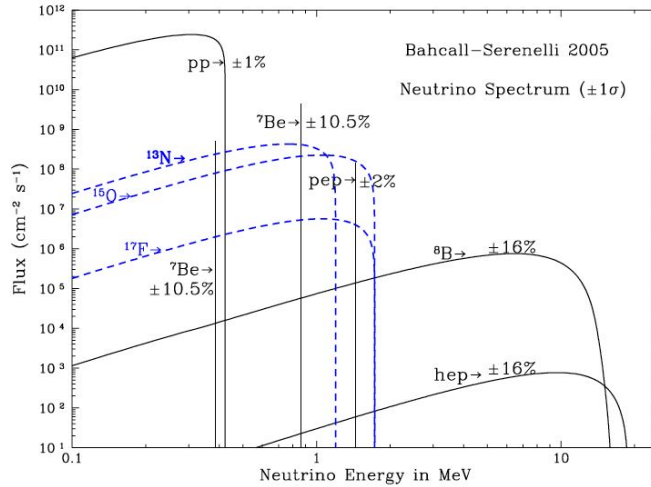


Figure 1.3: Expected neutrino spectrum according to the SSM BS05 [12].

years until they reach the surface of the Sun due to absorption and re-emission processes in the solar plasma.

Assuming a thermal equilibrium in our Sun, the neutrino luminosity can be determined by the solar photon luminosity. Only 2% of the total energy produced in the net reaction (1.9) is applied to the two ν_e . Therefore, one can approximate that about 13 MeV of energy along with each ν_e are released within the Sun. On basis of the solar constant $S = 1367 \text{ W m}^{-2}$, one can estimate the total neutrino flux on Earth:

$$\Phi_{total} \approx \frac{S}{13 \text{ MeV}} = 6.56 \cdot 10^{13} \text{ m}^{-2} \text{ s}^{-1} \quad (1.18)$$

The above estimation of total neutrino luminosity is the most restrictive constraint on the total solar neutrino flux and is known as the *Luminosity Constraint*. All individual neutrino fluxes from the pp and CNO sequences according to the SSM are listed in Table 1.1 and shown in Figure 1.3.

The influence of the MSW effect (sec. 1.2.2) on the solar neutrino spectrum is illustrated in Figure 1.4. The low energy region of the solar neutrino spectrum is dominated by vacuum-oscillations (affecting $pp-\nu$), while higher energetic solar neutrinos (especially ${}^8\text{B}-\nu$) are subject to matter-dominated oscillations. $pep-$ and ${}^7\text{Be}-\nu$ are located in the transition region. For more details, see [14].

Neutrino Branch	$\Phi [\frac{1}{cm^2 s}]$	$E_\nu [MeV]$
pp	$5.99 \cdot 10^{10}$	[0,0.42]
pep	$1.42 \cdot 10^8$	1.44
hep	$1.42 \cdot 10^3$	[0,18.8]
7Be	$4.84 \cdot 10^9$	0.86
7Be	$4.84 \cdot 10^9$	0.38
8B	$5.69 \cdot 10^6$	[0,14.6]
${}^{13}N$	$3.07 \cdot 10^8$	[0,1.2]
${}^{15}O$	$2.33 \cdot 10^8$	[0,1.7]
${}^{17}F$	$5.84 \cdot 10^6$	[0,1.7]

Table 1.1: Expected ν -rates within the three neutrino windows in counts per day and $100t$ according to the SSM [13] The two ${}^7Be-\nu$ branches derive from the ground state and the $487 keV$ excited state of 7Li .

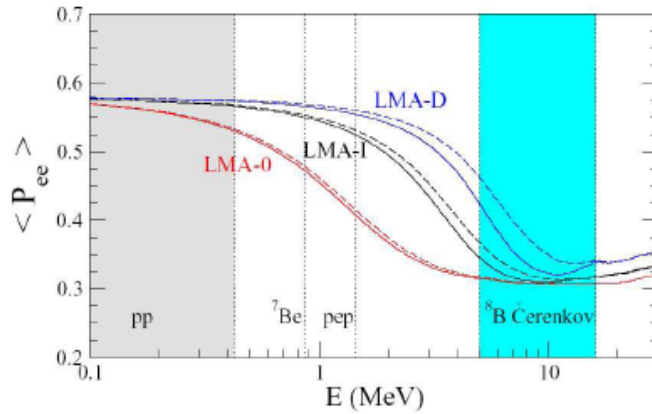


Figure 1.4: Solar neutrino survival probability in the *Large Mixing Angle* (LMA) scenario (black curve) [15]. At energies of a few MeV there is visible the transition between vacuum and matter-enhanced oscillation regimes. LMA-0 and LMA-D are alternative models considered in [16].

1.4 Solar neutrino detectors

With the goal to unravel the SNP, detectors and their detection techniques have evolved since the first detection of solar neutrinos 30 years before. All present solar neutrino experiments can be classified in three categories according to the detection technique applied. These are radiochemical, water Cherenkov and liquid-scintillator detectors. This section will provide an overview of these major detector types and will illustrate representative experiments.

1.4.1 Radiochemical detectors

Radiochemical detectors are based on the CC reaction of solar electron neutrinos on an element A_ZX according to



where A the total number of nucleons and Z the number of protons. Element X is chosen in order to obtain a radioactive element Y and a low energy threshold. After a sufficient exposure time, element Y is filtered by radiochemical means from the target mass and its amount is determined by the number of its radioactive decays. The measurement of the built-up activity of element Y allows a determination of the total ν_e flux. The critical parameters in the selection of a proper target element X are the energy threshold of the reaction (1.19), as well as the mean lifetime of the resulting element Y . Radiochemical detectors provide a time and energy integrated measurement of the solar ν_e flux without directional information of the original ν_e .

The Homestake experiment

The Homestake experiment [1] performed from 1970 until 1996 by Raymond Davis and his collaborators was the first experiment in the field of neutrino astronomy. Located at the Homestake mine in South Dakota (USA), this radiochemical experiment consisted of a tank containing 615 t of liquid perchlorethylene (C_2Cl_4). Solar neutrinos interacted with the Chlorine in the detector according to the reaction



with an 814 keV energy threshold. After a sufficient exposure time, ${}^{37}Ar$ atoms are extracted from the target mass by purging it with a helium carrier gas and passing it through a charcoal filter. The number of ${}^{37}Ar$ atoms is determined by

its radioactive decay ($\tau(^{37}\text{Ar}) = 50.5 d$) using proportional counters. On basis of the *Standard Solar Model* (SSM), a signal rate of

$$R_{\text{expected}} = 7.7_{-1.0}^{+1.2} \text{ SNU} \quad (1.21)$$

was expected for the Homestake experiment ($1 \text{ SNU} = 10^{-36} \text{ counts}/(s \cdot \text{target nucleus})$). After 26 years of data taking, the experiment measured a signal rate of [1]:

$$R_{\text{measured}} = 2.56 \pm 0.22 \text{ SNU} \quad (1.22)$$

This difference between expectations according to the SSM and experimental results gave birth to the *Solar Neutrino Problem* (SNP). Other radiochemical solar neutrino detectors followed the Homestake experiment, i.e. GALLEX/GNO [17, 18] and SAGE [19]. They all confirmed the solar neutrino deficit. For his pioneering work on the field of neutrino astronomy, Raymond Davis was awarded with the Nobel Prize in physics in 2002.

1.4.2 Cherenkov detectors

A charged particle moving in matter (of refractive index n) faster than the speed of light within the given material emits Cherenkov light (Cherenkov condition: $n\beta \geq 1$). In analogy to the Mach cone of supersonic objects, the Cherenkov light is radiated in a cone along the direction of flight. The opening angle is correlated with the particle speed, and therefore can be used to determine its energy. In addition, the characteristic light emission is used to reconstruct the direction of the particle.

Neutrinos are neutral particles and therefore do not produce Cherenkov light by themselves. However, they can scatter on electrons and produce energetic charged particles (see eq. (1.24)). If the charged particle fulfills the Cherenkov condition, the direction and energy of the accelerated particle and also the parent solar neutrino can be observed. Thus, in contrast to radiochemical experiments, Cherenkov detectors provide a real-time spectral detection of solar neutrinos. Due to external background conditions and the relatively low light yield, current Cherenkov detectors possess an energy threshold of about 5 MeV , limiting solar neutrino detection to the higher energetic region of $^8\text{B}-\nu$ (see Figures 1.3 and 1.4).

KamiokaNDE/Super-Kamiokande

In the early '80s, KamiokaNDE (Kamioka Nucleon Decay Experiment) [20] was constructed in the Mozumi mine (Japan) with the purpose to detect nucleon decay.

A mass of 3 kt of pure water was monitored by 1000 photomultiplier tubes (PMT). In 1985 KamiokaNDE was upgraded to a neutrino detector and eventually was the first detector measuring solar neutrinos in real time.

The KamiokaNDE experiment has been replaced by its successor, the Super-KamiokaNDE (SK) [2] detector, which has been commissioned in 1996. Like KamiokaNDE, SK is based on the detection of neutrinos by the Cherenkov light emission of neutrino-scattered electrons. However, due to its larger dimensions, the SK experiment provides higher statistical possibilities than its predecessor.

SK consists of a cylindrical stainless steel tank with a diameter of 39.3 m and a height of 41.4 m , filled with 50 kt of ultra-pure water in total. An additional cylinder in the steel tank separates the experiment in two parts: the inner and the outer detector. The outer detector contains 18 kt of water and is equipped with 1885 PMTs. It serves as shielding for external radioactivity and active veto for muons. The inner detector is filled with 32 kt of water, with a fiducial mass of 22.5 kt observed by 11146 PMTs. In a data taking time of 1496 days, SK measured a ${}^8\text{B}-\nu$ flux [21] of

$$\Phi_{sB} = (2.35 \pm 0.02[\text{stat}] \pm 0.08[\text{syst}]) \cdot 10^6 \text{ cm}^{-2} \text{ s}^{-1} \quad (1.23)$$

This flux accounts only for about 45% of the ${}^8\text{B}-\nu$ expected on basis of the SSM.

SNO

The SNO (Sudbury Neutrino Observatory) experiment [3] has been performed from 1999 to 2006 in the Creighton mine in Sudbury (Canada). The main component of the detector is a transparent acrylic vessel of 12 m diameter, which contains 1 kt of heavy water (D_2O). The detector cavity outside the vessel is filled with pure water to provide buoyancy and shielding against external radioactivity. Due to a high rock coverage of $\sim 2000\text{ m}$ ($\sim 6000\text{ m.w.e.}$) no additional muon veto is necessary. The vessel is monitored by 9600 PMTs mounted on a geodesic sphere surrounding the vessel. The reaction channels used for neutrino detection are:

- Elastic scattering on electrons

$$\nu_x + e^- \rightarrow \nu_x + e^- \quad (1.24)$$

Elastic scattering is sensitive to all neutrino flavors (ν_x) by Neutral Current (NC) interaction. ν_e are also capable of Charged Current (CC) interaction, and thus their cross section is about a factor of 6.6 higher than for ν_μ, ν_τ .

- Deuteron dissociation

$$\text{CC: } \nu_e + D \rightarrow e^- + 2p \quad (1.25)$$

$$\text{NC: } \nu_x + D \rightarrow \nu_x + p + n \quad (1.26)$$

The deuteron dissociation in CC reactions is only sensitive to ν_e . NC dissociation of deuteron is sensitive to all neutrino flavors.

The combination of all three processes yields information on the flux of ν_e and the combined flux of ν_μ, ν_τ in the 8B - ν energy region [22]:

$$\Phi_{sB-\nu_e} = 1.76_{-0.05}^{+0.05}[\text{stat}]_{-0.09}^{+0.09}[\text{syst}] \cdot 10^6 \text{ cm}^{-2} \text{ s}^{-1} \quad (1.27)$$

$$\Phi_{sB-\nu_\mu, \nu_\tau} = 3.41_{-0.45}^{+0.45}[\text{stat}]_{-0.45}^{+0.48}[\text{syst}] \cdot 10^6 \text{ cm}^{-2} \text{ s}^{-1} \quad (1.28)$$

The total sum of the ν -flux is well in agreement with expectations of the 8B - ν according to the SSM. This result demonstrated a confirmation of the SSM, and also proved flavor conversion of solar neutrinos.

1.4.3 Liquid Scintillator detectors

Detectors of this type probe solar neutrinos by their elastic scattering on electrons within a liquid scintillator target mass. The recoil-electron deposits its energy in the detector, exciting the organic scintillator molecules. Eventually, these molecules isotropically emit their excitation energy in the UV-light spectrum. The application of wave length shifters significantly reduces self absorption within the scintillator. Due to the isotropic light emission, no directional information is obtainable.

The high light yield of scintillator detectors allows exceptional energy and position reconstruction of events and enables sub-MeV real-time solar neutrino spectroscopy. However, high radio-purity of the detector material is necessary to measure the low energetic solar neutrino fluxes.

KamLAND

The KamLAND (*Kamioka Liquid scintillator Anti-Neutrino Detector*) detector [23] is situated at the former site of the KamiokaNDE experiment. The detector design of KamLAND is very similar to the Borexino detector, which is described in sec. 2.3. A nylon balloon of 13 m in diameter holds 1 kt of organic liquid scintillator, which is surrounded by buffer oil for buoyancy and shielding. These components are contained in a stainless steel sphere of 18 m in diameter. About 1900 PMTs mounted on the steel sphere monitor the target mass. The steel sphere is surrounded by an external water tank, which is viewed by 225 PMTs. It serves as shielding from external background and as an active muon veto.

The KamLAND experiment was originally designed as a reactor anti-neutrino

detector, however since 2007 a purification campaign is in progress to enlarge the detectors capacities into the field of sub-MeV solar neutrino spectroscopy.

Chapter 2

The Borexino experiment

The scientific importance of a direct measurement of all solar neutrino fluxes led to the foundation of the Borexino collaboration in the early '90s. This international collaboration has been growing ever since and consists by now of more than 15 institutions from seven different countries. With the main goal to unravel the solar neutrino fluxes, the collaboration developed the Borexino experiment [24, 25], a 300 t organic liquid-scintillator detector. On basis of the expected low solar neutrino signal of a few tens of events per day, an extremely low level of radioactive contamination of scintillator and construction material was the central challenge of detector design. In order to test the feasibility of the required high radio-purity levels, a construction of a prototype of the Borexino detector was started in the early '90s, named Counting Test Facility (CTF) [26]. Although reduced in scale with a target mass of about 4 t, this prototype exhibits all main features of the prime detector Borexino. Besides the main purpose of studies on scintillator mixtures and radio-purification, the CTF also performed a wide range of physics studies [27, 28, 29, 30, 31, 32]. An analysis on cosmogenic ^{11}C background performed in the third campaign of the CTF [15, 32, 33] has to be emphasized, as it is important for this thesis. In sec. 4.2.1, those results will be compared with spectral studies on ^{11}C in Borexino. Succeeding in achieving high purification standards by the CTF, the construction of the Borexino detector started in 1996 at the underground site of the INFN *Laboratori Nazionali del Gran Sasso* (LNGS). Borexino has been commissioned on May 16th 2007 and is taking data up to the present day.

This chapter will provide an overview of the liquid-scintillator detector Borexino. First of all, the principle of solar neutrino detection in Borexino is presented, followed by a description of the physics goals and the design of the experiment. In the last section of this chapter, the first real time detection of ^7Be solar neutrinos by Borexino [34] is presented.

2.1 ν -detection principle

Borexino is sensitive to all neutrino flavors by elastic scattering off electrons via neutral current interactions:

$$\nu_x + e^- \rightarrow \nu_x + e^- \quad (2.1)$$

Furthermore, ν_e are capable of interacting with electrons via charged currents and therefore possess a higher cross section than other neutrino flavors. The scattered electron deposits its energy in the scintillator producing light which is detected by an array of photomultiplier tubes (PMT). With a mean free path of at most a few centimeters in the scintillator, the recoil electron is almost a point like light source. Therefore, it provides no directional information on the original neutrino. Moreover, β - and γ -emission from radioactive background in the detector produce signals which are indistinguishable from ν -signals on an event-by-event basis. Therefore an ultra-high level of radio-purity is the main requirement for a determination of solar neutrino fluxes.

2.2 Physics goals

Up to now, the measurement of ${}^7\text{Be}-\nu$ is one of the most urgent requirements in solar astrophysics. The Borexino experiment aims at the measurement of the ${}^7\text{Be}-\nu$ rate with a precision of at least 10%.

By means of the luminosity constraint described in sec. 1.3.3, the ${}^7\text{Be}-\nu$ rate is interconnected with the fundamental $pp-\nu$ flux, which makes up 91% of the total solar neutrino flux. The aimed precision of the determination of ${}^7\text{Be}-\nu$ rate would increase the precision of the pp flux by a factor of ~ 4 .

Moreover, the monoenergetic $862\text{ keV}-{}^7\text{Be}$ neutrinos are located in the vacuum-dominated region of neutrino oscillations according to the MSW-LMA oscillation scenario [14]. A measurement of the ${}^7\text{Be}-\nu$ therefore allows a test of the MSW-LMA model by comparison with the integral neutrino flux in the transition region [17, 18] and matter-dominated oscillation region [21, 22].

Besides the determination of the ${}^7\text{Be}$ neutrino rate, Borexino has various other objectives. The subjects of physics amenable by the Borexino detector are as manifold as the sources of neutrinos. Natural and artificial sources provide insight in specific neutrino production mechanisms as well as in intrinsic properties of the neutrino as a particle. A short overview of different sources of neutrinos accessible by the experiment are outlined in the following:

- **Solar neutrinos**

Up to the start of data taking by Borexino, ${}^8\text{B}$ posed the only solar neu-

trino flux measured in real-time experiments, namely SNO [22] and Super-Kamiokande [21]. Due to the high radioactive background, the 8B - ν spectrum has only been determined at energies above ~ 5.5 MeV. However, the high radio-purity standards realized in Borexino now open the window to real-time detection of neutrino fluxes down to sub-MeV energies. Besides 7Be - ν , also the fluxes of all other solar neutrino production processes are at hand, i.e. the pp / pep , CNO fluxes and the low energetic part of the 8B flux. For more details on these neutrino fluxes see Chapter 4.

Furthermore, non-standard physics mechanisms suggest a non-vanishing magnetic moment of the neutrino. This could lead to a spin flip in the solar magnetic field resulting in a ν_e - $\bar{\nu}_e$ conversion [35]. This hypothesis can be tested by searching for a $\bar{\nu}_e$ contribution to the solar neutrino flux [36].

- **Geoneutrinos**

Geophysical models suggest that about 20 TW of a total of 30-45 TW of Earth's heat dissipation rate originate from progenies of ${}^{238}U$, ${}^{232}Th$ and ${}^{40}K$ decays in Earth [37]. The neutrinos and anti-neutrinos emitted by these decays are called geoneutrinos. The expected rate of geoneutrinos varies for the different Earth composite models. Thus, by detecting geoneutrinos these models can be probed. Especially Uranium and Thorium are of great interest, because their $\bar{\nu}_e$ end-point energies are above the threshold of inverse beta decay on free protons of 1.8 MeV, which is used to detect these geoneutrinos:



The positron annihilates with an electron, while the neutron is eventually captured within the detector. This delayed coincidence is a clear signal of $\bar{\nu}_e$ detection. The expected rate of detected geoneutrinos is of the order of tens per year, depending on the Earth composite model used. Nuclear power plants introduce a background to this measurement due to $\bar{\nu}_e$ emission in the course of thermonuclear energy production. There are no nuclear reactors in Italy, while European power plants are at a mean distance of ~ 800 km to the LNGS. This absence of nearby nuclear power plants benefits the detection of the extremely low signal rate of geoneutrinos.

- **Supernova neutrinos**

A core collapse Supernova (SN) produces a huge amount of neutrinos in the formation of a neutron star or a black hole, but even more by Kelvin-Helmholtz neutrino cooling. All flavors of neutrinos and anti-neutrinos are

emitted in a burst lasting ~ 10 s. These neutrinos can be detected by several reaction channels in Borexino, i.e. elastic scattering on electrons and protons, inverse β -decay on protons, as well as neutrino capture and inelastic scattering on ^{12}C [38]. A reference SN explosion at the center of our galaxy (~ 10 kpc) with a binding energy of $\epsilon = 3 \cdot 10^{53}$ would produce a total event number of ~ 180 -190, mainly due to $\bar{\nu}_e$ [38]. This would provide a test of Supernova models, neutrino mass limits, as well as neutrino oscillations.

- **Neutrino beam**

The CNGS (CERN-Neutrinos-to-Gran-Sasso) project [39] is based on a 20 GeV ν_μ -beam generated at the CERN and directed to the 730km distant LNGS site. The experiments OPERA [40, 41] and ICARUS [42] aim to detect neutrino oscillations within the ν_μ -beam. Especially OPERA is designed for the detection of ν_τ appearance in the ν_μ -beam. Borexino is a target for this long baseline experiment, too. Muon-neutrinos from the beam interact with the surrounding rock at the LNGS site, or the Borexino detector material itself, and produce muons in charged current reactions. These can be detected by Borexino. A beam run recently performed in the time span of 21st till 28th of September resulted in number of about 900 muon events in Borexino.

2.3 Detector design

Due to an expected low signal rate, the design of Borexino is based on the suppression of external background and need for high internal radio-purity. The detector is structured in concentric shells providing graded shielding for the central active detection volume consisting of liquid scintillator. In addition, the radio-purity levels of construction and screening material increase from the outer part to the center of the detector. Figure 2.1 shows the schematics of the Borexino detector. The Borexino experiment consists of two main detector systems interconnected within data acquisition (DAQ), but separated by the *Stainless Steel Sphere* (SSS): the so called *Inner Detector* (ID) and *Outer Detector* (OD). Both detectors are described in detail in the following.

2.3.1 The Inner Detector

The *Inner Detector* (ID) monitors the central active volume and also its surrounding buffer liquid. Neutrino detection in the Borexino experiment is performed by the ID. It is composed of several concentric shells:

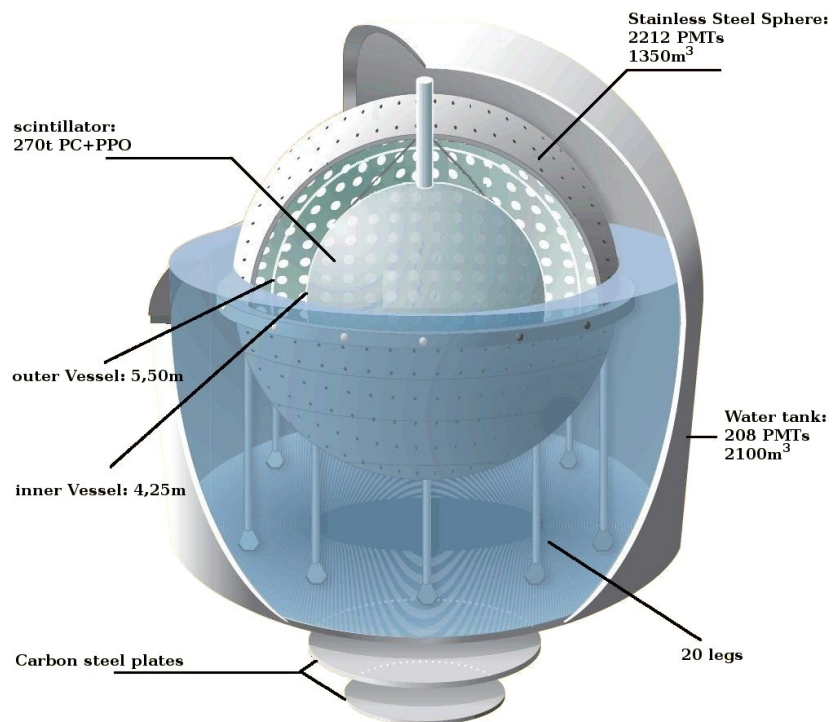


Figure 2.1: Schematics of the Borexino experiment [11].

Liquid Scintillator and Inner Vessel

In the center of the Borexino experiment is the volume of 320 m^3 liquid scintillator corresponding to a mass of 280 t . After tests performed in the CTF, the scintillator mixture was chosen to be pseudocumene (PC, 1,2,4-trimethylbenzene, $C_6H_3(CH_3)_3$) as solvent with PPO (2,5-diphenyloxazole, $C_{15}H_{11}NO$) as wavelength shifter at a concentration of 1.5 g/l . Charged particles traversing the scintillator excite the PC molecules which transfer their excitation energy non-radiatively to PPO. In turn, PPO radiates with a decay time of 1.3 ns at in the optical band centered near 400 nm [34]. At this wavelength the optical attenuation length of the scintillator is $\simeq 7\text{ m}$ [34].

The scintillator mixture is contained in the so-called *Inner Vessel* (IV), a transparent nylon membrane with a radius of 4.25 m and a thickness of $125\text{ }\mu\text{m}$. It is hold in position by an array of nylon strings which are connected to loading cells in order to monitor mechanical stress on the IV. As it is in contact with the active detection volume of Borexino, the IV was subject of intensive radio-purity controls and production standards. However, in order to reject remaining contents of radioactive impurities on the IV as well as background from outside, an analysis cut at 3.276 m defines the so called *Fiducial Volume* (FV) which corresponds to a target mass of 100 t . In the ${}^7\text{Be}$ energy window, the amount of external background contributions within the FV is negligible. Fluid handling of the IV is possible via pipes connected to the upper and lower poles.

Buffer Liquid and Outer Vessel

The IV is enclosed by the *Outer Vessel* (OV), a second nylon membrane of same thickness but at a radius of 5.50 m . The OV itself provides a barrier for radon diffusion toward the IV. It contains a buffer liquid composed of PC and 5.0 g/l DMP (dimethylphthalate) of nearly the same density as the scintillator. Therefore only a small hydrostatic pressure is applied on the IV. The DMP quenches the residual scintillation light produced by the PC by a factor of ~ 20 and therefore guarantees that the dominant signal arises from the interior of the IV. DMP does not influence photon propagation and therefore does not distort the reconstruction of events in the IV [15]. Buffer liquid is also present between the OV and the SSS which is described next. The overall amount of buffer liquid filled in Borexino is 1040 t .

Stainless Steel Sphere

The *Stainless Steel Sphere* (SSS) represents the central support structure of the Borexino experiment. It has a radius of 6.85 m and is mounted on 20 legs to

the floor of the external *Water Tank* (WT). The SSS supports 2212 PMTs on the inside. 1838 of these are equipped with aluminium light concentrators, which focus the field of view on the IV and enlarge the light collection efficiency by a factor of ~ 2 -3. The remaining 374 PMTs without concentrators possess a wider visual field and are therefore more sensitive to events outside the IV. The combination of both types of PMTs provides an excellent identification of muon events traversing the ID (see the so-called *Deutsch parameter* in sec. 3.3.2). The overall geometrical coverage achieved in this way is about 30%. Each PMT is connected with a single submarine cable for signal and high voltage supply, and in addition with an optical fibre for calibration purpose. A laser signal of 394 nm injected simultaneously in these fibres provides a reference signal for the whole ID. The glass of the PMTs emanates a considerable amount of Radon into the buffer liquid. Especially to protect the IV from any Radon emanation the additional OV was introduced to the design of Borexino.

Together with its inner components, the SSS forms the *Inner Detector* system. Furthermore, the SSS supports on its outer surface an array of PMTs which are part of the *Outer Detector* system.

2.3.2 The Outer Detector

Buffer water and external Water Tank

The external *Water Tank* (WT) is a steel dome of 9 m in radius with the highest point of the dome 17 m above the floor, containing the SSS. It is filled with 2400 t of ultrapure water and serves as the outermost shielding of the experiment from external radiation. Whereas the surface flux of atmospheric muons is reduced by a factor of 10^6 , residual muons at the LNGS site can not be screened by this water shield. However they emit a characteristic Cherenkov light cone in the water. Taking advantage of this feature, 208 PMTs are mounted on the outer surface of the SSS and on the floor of the water tank. This *Outer Detector* (OD) serves as an active veto of muon events. The inner walls of the dome and the outer parts of the SSS are covered with highly reflective Tyvek sheets. The PMTs in the OD are calibrated with an array of near-UV LEDs with optical fibres connected to the PMT frame. The optical fibres are connected to LEDs, which are mounted in the LED crates of OD electronics (see sec. 3.2.1). Via the optical fibres each PMT can be addressed separately.

Organ Pipes

The wiring of the ID and OD is fed through steel tubes, the so-called *Organ Pipes*, through the top of the dome. The cables are then directed to the electronics room

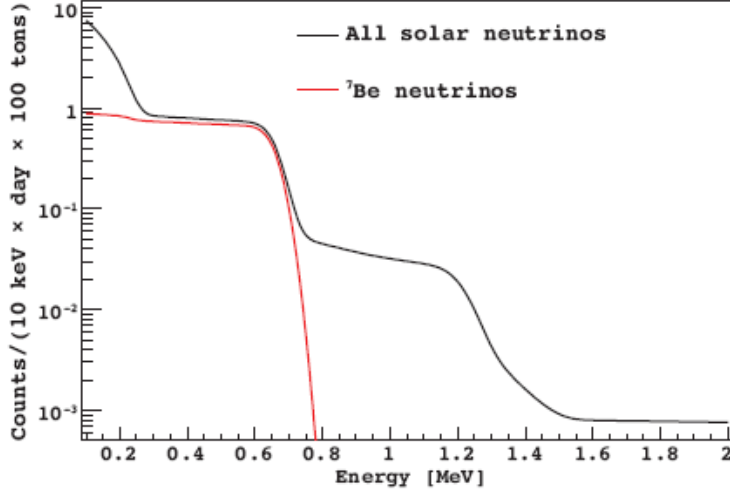


Figure 2.2: Expected electron-recoil spectrum in Borexino considering the detector’s energy resolution. The black line represents the total neutrino signal rate in Borexino according to the most recent predictions of the Standard Solar Model including neutrino oscillations with the MSW-LMA parameters. The red line illustrates the contribution from ${}^7\text{Be}$ neutrinos. pp neutrinos contribute to the spectrum below 0.3 MeV . The edge at 1.2 MeV is due to pep neutrinos (Picture from [34]).

located in a building next to the Borexino experiment. In order to secure temporal correlation of PMT hits, all cables are of the same length of 55 m .

2.4 First real time detection of ${}^7\text{Be}$ solar neutrinos

After three months of data taking, the Borexino collaboration published at the 16th of August 2007 the first real time detection of ${}^7\text{Be}$ solar neutrinos [34].

Figure 2.2 shows the expected signal of solar neutrinos in Borexino. The spectrum of the ${}^7\text{Be}$ recoil electron is highlighted, with the distinctive shoulder of the Compton-like recoil spectrum at 665 keV clearly visible. In Figure 2.3 the spectrum taken by Borexino is shown after application of several cuts in order to reduce background. The following cuts were applied:

- Rejection of muon-correlated background by the OD and several software

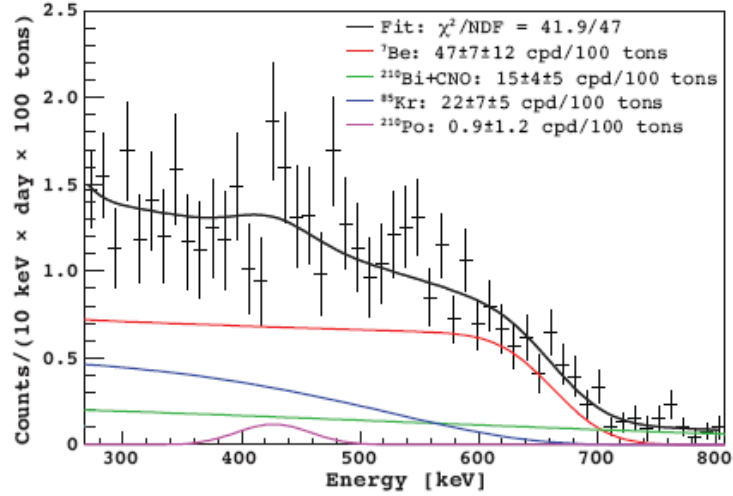


Figure 2.3: Electron-recoil spectrum in the energy region from 270 keV up to 800 keV after the basic selection cuts and a subtraction of Radon daughters and muon-correlated activity. Also a fiducial cut has been applied and a full α/β statistical subtraction of the ${}^{210}\text{Po}$ α -decay peak. The fitted remaining ${}^{210}\text{Po}$ demonstrates the high efficiency of this method. Other relevant radioactive contaminations present in the analyzed energy range are ${}^{85}\text{Kr}$ and ${}^{210}\text{Bi}$. Due to the similar spectral shape of ${}^{210}\text{Bi}$ β -decay and the $\text{CNO-}\nu$ signal, both contributions are combined in the fit. The prominent ${}^7\text{Be-}\nu$ signal (marked in red) is clearly visible at the expected 665 keV (Picture from [34]).

cuts.

- Rejection of external gamma background by a radial cut of 3.276 m , corresponding to the *Fiducial Volume* of 100 t .
- In July 2007, during a temporary refilling procedure due to temperature changes within the detector, ${}^{222}\text{Rn}$ entered the *Inner Vessel* (IV) of Borexino [34]. The liquids were introduced in the upper pole of the IV (sec. 2.3.1). Rejection of ${}^{222}\text{Rn}$ is achieved by a cut in the z -axis of 1.8 m . Daughter elements of Radon are rejected by the identification of ${}^{214}\text{Bi-}{}^{214}\text{Po}$ coincidences.
- Statistical subtraction of the prominent ${}^{210}\text{Po}$ peak by means of an α/β pulse shape discrimination.

For a detailed description of the data analysis performed on ${}^7\text{Be-}\nu$, see [34]. The ${}^7\text{Be}$ shoulder is clearly visible in the data at the expected 665 keV . The expected

rate based on solar models without oscillation is $75 \pm 4 \text{ counts day}^{-1} (100 t)^{-1}$ whereas the inclusion of neutrino oscillations according to the MSW-LMA oscillation solution results in the prediction of $49 \pm 4 \text{ counts day}^{-1} (100 t)^{-1}$. The best fit of the ${}^7\text{Be}$ rate determined by Borexino is [34]:

$$47 \pm 7_{stat} \pm 12_{sys} \frac{\text{counts}}{\text{day} \cdot 100 t} \quad (2.3)$$

This result supports the MSW-LMA oscillation scenario. The main source of systematic uncertainty is the definition of the fiducial mass, which is currently estimated to 25%. However, work is in progress to reduce this uncertainty by an intensive calibration campaign in the near future.

Chapter 3

Data acquisition and structure

An event occurring in the *Inner Detector* (ID) and the *Outer Detector* (OD) produces light via scintillation and Cherenkov radiation, respectively. This light is collected by the photomultiplier tubes (PMT). For each detected photon, arrival time and deposited charge are recorded by means of the analogue and digital chain of the data acquisition (DAQ) system. For consistency checks, two independent offline data reconstruction codes were developed within the Borexino collaboration, i.e. the *Echidna* [15] and the *Mach4* [43] code. Both codes process the data and reconstruct all relevant physics parameters of an event. The analysis performed in this diploma thesis is based on the *Echidna* code.

This chapter presents the main features of DAQ, and describes the modification of Borexino electronics performed within this thesis. A pulser system for identification of malfunctioning DAQ channels of the OD has been constructed and implemented into the electronics read-out chain of the OD. The last section outlines the *Echidna* event reconstruction code and covers the variables used for analysis in Chapter 5.

3.1 Trigger system

3.1.1 Main Trigger System

The ID and OD are read out when the DAQ receives a trigger issued by at least one of the two detectors. The ID activates the trigger when 30 PMTs are hit within 60 ns , corresponding to an energy threshold of about 60 keV . The condition for the OD trigger is that at least 6 PMTs are firing within a time window of 150 ns . In case of a trigger, the time and charge information of each PMT hit in a given time gate are written to data base for both detectors. For the time period of data considered in this thesis (07/10/07 until 10/27/07), hits in the ID are recorded

within a time gate of $\sim 7.5 \mu s$, whereas for the OD the time gate is $\sim 8.5 \mu s$. The time resolution of these hits is of about $0.5 ns$, which is smaller than the intrinsic time jitter of the PMTs of $1.1 ns$. Details on time and charge determination in the analogue and digital chain of Borexino can be found in [15].

3.1.2 Analogue Neutron Trigger

The analogue neutron trigger is a tributary trigger system to the OD trigger. Its purpose is the detection of spallation neutrons produced by muons traversing the detector. The neutron trigger logic is depicted in Figure 3.1.

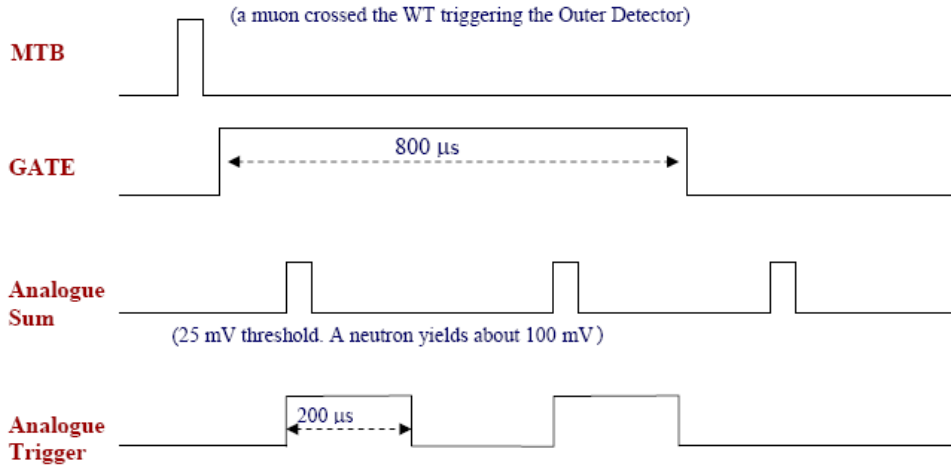


Figure 3.1: Timing sequence of the analogue neutron trigger after a muon crossed the *Water Tank* (WT) (sec. 2.3.2) triggering the OD [44].

The trigger board of the OD, the so called *Muon Trigger Board* (MTB), opens a time gate of $[25,800] \mu s$ for the analogue neutron trigger. A deadtime of $25 \mu s$ has been chosen to prevent fake events usually following muons, the so-called “muon afterpulses”. Muons produce a huge amount of light and therefore often ionize rest-gas inside the PMTs, which can produce noise signals for several *ms* after the muon. For more details on muon afterpulses see sec. 4.4.1.

The neutron trigger sets a threshold of $25 mV$ (~ 150 photoelectrons) to the analogue sum of the output of all ID PMTs. In this way, it suppresses most of the afterpulses, while neutron signals (with a typical height of $100 mV$) are recorded and specially flagged by DAQ.

However, detection of neutrons is complicated by the *Three Fast Trigger Coincidence* (TFTC) veto, which is activated when DAQ is triggered twice in less than $\sim 200 \mu s$. In this case, the veto prohibits any additional read-out of Borexino

within the next $\sim 2\text{ms}$. This drastically affects muons which produce multiple neutrons. Usually, only one neutron of such a muon-induced neutron shower can be detected by the neutron trigger. For more detail on neutron detection with respect to the analogue neutron trigger and TFTC veto, see Section 4.4.2.

3.2 Implementation of the Outer Detector pulser system

A physical event occurring in the detector is registered by the PMTs and transferred via an electronics chain to the data base mainframe *bmaster* [15]. Data acquisition and analysis are strongly dependent on the status of the DAQ. Broken signal channels affect the quality of event reconstruction, like position and energy. Thus, calibration and monitoring of the signal channels are necessary for each run to obtain reliable results. A signal channel with zero output in DAQ can be the result of malfunction of either PMT or electronics chain. PMT disfunction can not be fixed due to their position within the detector, in contrast to the DAQ electronics. The major portion of the electronics chain is assembled in the electronics room positioned next to the Borexino experiment, and thus is easily accessible. For detector maintenance it is indispensable to identify the source of disfunction in signal channels. On this account a pulser system for the OD has been constructed and assembled within DAQ electronics as part of this thesis. At first this section will present an overview of the OD DAQ electronics, and afterwards describe the newly installed pulser system.

3.2.1 Outer Detector electronics

The signal from the 208 PMTs of the OD is processed by an electronics chain located in two crates, the *High-Voltage-Decoupler* (HVD) rack and the *Signal-Processing* (SP) rack, shown in Figure 3.2. The first step of signal processing is performed in the HVD rack, i.e. the decoupling of the PMT signal from the high voltage powering the PMTs. Within the SP rack, the decoupled signal is converted from an analogue signal to a logic pulse and afterwards digitized. In addition, the signal of the OD PMTs is used to address the muon trigger board and the scalers, which are both located in the SP rack. The electronics chain is presented in the following with respect to both crates.

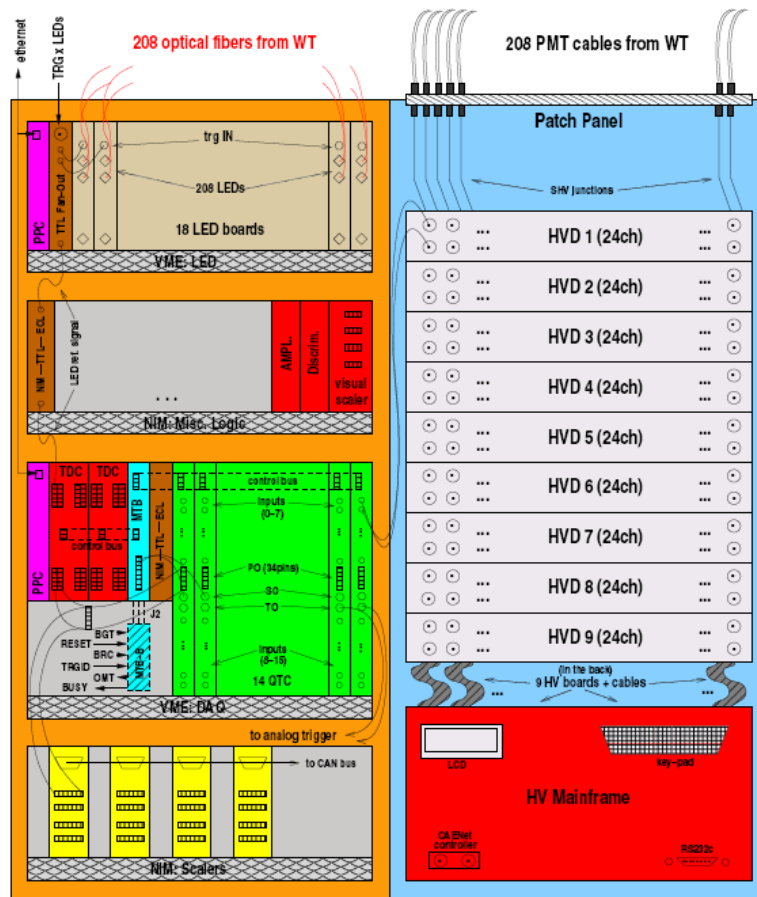


Figure 3.2: Schematics of the *High-Voltage-Decoupler* and *Signal-Processing* electronics racks of the *Outer Detector* [15].

Electronics chain within the HVD rack

The 208 PMTs of the OD are powered by AC high voltage via coaxial cables, which also transmit the PMT signal. These coaxial cables leave the detector through the organ pipes of the *Water Tank* (WT) described in chapter 2, and enter the nearby electronics room. To preserve temporal correlation all cables are of the same length of 55 m. In the electronics room, the cables arrive at top of the HVD rack and are connected to the **Patch Panel** (see Figure 3.2). The signal from the 208 PMTs is then forwarded by junction cables (SHV) to 9 **High Voltage Decoupler** (HVD) frames, each containing 2 boards à 12 channels. The HVDs decouple the PMT response from the AC high voltage, and transmit the decoupled pulse to the QTC-boards in the SP rack. The HVDs are powered by the **High Voltage Mainframe** (HV Mainframe), which is located at the bottom of the HVD rack. The new pulser system, which is described in section 3.2.2, has been installed into the HVD frames on the front end side.

Electronics chain within the SP rack

The decoupled pulse is fed to 14 **Charge-To-Time-Converter** (QTC) boards located in the SP rack, each containing 16 input and 3 output connectors. For each PMT the decoupled pulse is processed and three different output signals are produced:

- **Primary Output (PO)**: The PO produces a logic signal with the first edge providing the time of the input signal, and the length corresponding to the detected charge of the PMT pulse. The POs of the 16 channels are grouped to a 34-Pin connector at the front end side of the board. They are connected with two **Time-to-Digital-Converter** (TDC) boards which continuously digitize incoming pulses into their memory buffer, which has a time window depth of $\sim 8.5 \mu s$. Data is periodically overwritten until a trigger occurs. In this case, the physical event is recorded within the time window and the memory buffer is written to data base. The **Scalers** are also connected to the PO, which are located on the bottom of the SP rack in Figure 3.2. They provide realtime information on event rates and can be accessed via a web interface. They enable a quick check of the OD status.
- **Secondary Output (SO)**: The SO produces a one-per-board logic step function with its height corresponding to the number of PMTs firing in coincidence. Its length gives the coincidence time window. The SO is used for identifying muons by activating OD triggering via the **Muon Trigger Board** (MTB).



Figure 3.3: Front-end side of a *High Voltage Decoupler* (HVD) frame, upside down. A pulser signal can be injected into both boards of the HVD via the newly installed *Pulser System Connectors* (PSC) (marked in red).

- Tertiary Output (TO): This output delivers a one-per-board analogue pulse, which is the sum of all analogue input-pulses with a built-in fixed amplification factor of 2. Due to geometrical reasons some muons produce their Cherenkov light only in a small area. Therefore, only a few PMTs are illuminated by a huge amount of photons. The purpose of the TO is to identify these muons by activating the *Muon Trigger Board*.

As will be described in sec. 3.3.1, offline data processing requires electronics calibration of the detector within each run. LEDs located on the front of the *LED Boards* at the top of the SP rack (shown in Figure 3.2) emit calibration light pulses, which are transmitted via optical fibres to the OD PMTs. In the process of detector calibration, the laser reference signal for ID calibration and the LEDs are fired simultaneously, to calibrate both detectors at the same time.

3.2.2 Pulser system installation

A channel without any output can be easily identified by a look at the *Scalers* via the web interface. Zero rate of a channel can be the result of either a broken PMT or a malfunction in the electronics chain. By injection of a reference signal into the electronics chain its operational reliability can be checked. The identification of a fully functional electronics chain would automatically imply a disfunction of the corresponding PMT. Such a electronics monitoring system had only been present in the ID and has been installed to the OD as part of this thesis. The newly installed *Pulser System* injects a reference pulse simultaneously into each of the QTC-channels and probes the electronics status of the OD for every run.

The *Pulser System* has been installed into the 9 HVDs located in the HVD rack as well as into 2 spare HVDs. Each HVD frame contains 2 boards à 12 channels, with each board modified as a whole. The *Pulser System* installed to each board features

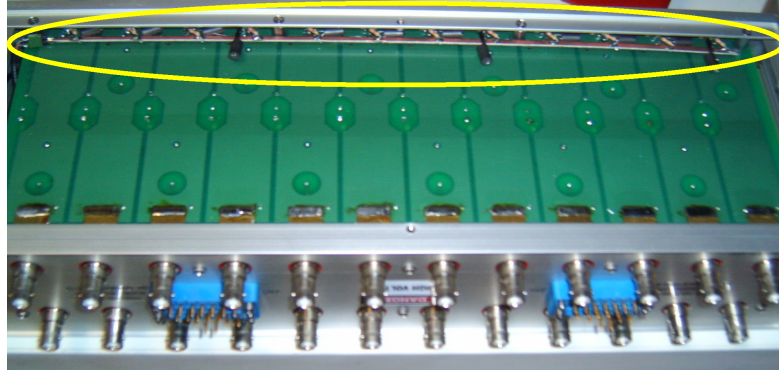


Figure 3.4: Back view of the open HVD frame, with one of the two boards visible. The new pulser system (marked in yellow) is connected with all 12 output channels of the HVD board, and can be addressed by the PSC, shown in Figure 3.3.

as the central component a copper bar of 42 cm length and 0.4 cm depth, as shown in Figure 3.4. The system is based on the injection of a reference signal via the copper bar into all 12 output channels of a HDV board. The coupling between the copper bar and the output channels can be achieved by an inductive or a capacitive coupling. Prototypes of both types were constructed and their quality of signal transmission and channel crosstalk studied. A pulse shape generator injected a test reference signal into the prototypes which was compared with the output of the HVD boards with an oscilloscope. Both prototypes performed excellent, with little difference in their signal properties. Due to the lower costs, the HVD boards were equipped with the inductive coupling. Finally, the copper bar has been terminated by a $50\ \Omega$ resistor on one end, and connected to an additionally installed connector of the HVD mainframe on the other end. Thus, each board of the HVDs can be externally addressed by the *Pulser System Connector* (PSC) of each HVD frame, as shown in Figure 3.3. Via the PSC the output channels of each HVD board are addressed simultaneously. To guarantee, that all 18 boards of the 9 HVD are triggered simultaneously, the pulser signal is spread via two FAN IN/OUT modules to all 18 PSC (shown in Figure 3.5). A reference pulse generated by the *Pulser System* triggers data acquisition and is recorded by the detector with a special trigger type (see description of event properties in sec. 3.3.2). By now, the *Pulser System* is an inherent part of detector calibration and maintenance work.

The first 1000 events of each normal data taking run consist of artificial calibration pulses, which also contain the pulser signals for the OD. These pulses are also injected into DAQ during data taking with a rate of 0.1 Hz to monitor detector performance over the duration of the whole run. On basis of this *Pulser System* an evaluation program for OD diagnostics has been written within the Borexino

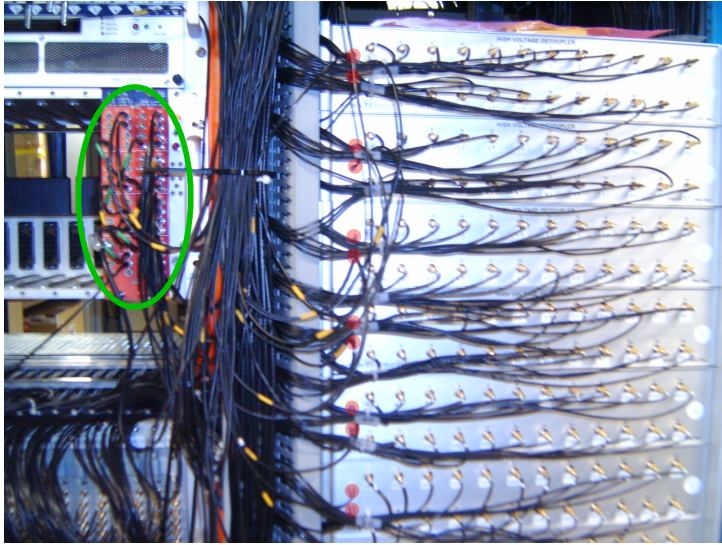


Figure 3.5: On the right side, the modified HVDs can be seen in the HVD rack, with the integrated PSC highlighted red. The PSC are connected to two FAN IN/OUT modules (marked in green), which are located in the SP rack on the left side.

collaboration and added to the *Echidna* frame work.

3.3 Echidna data structure

Echidna [15] is one of the two independent data reconstruction codes used within the Borexino collaboration. It is a very modular network-oriented code for offline data processing, based on C++/ROOT [45]. All analysis performed within the frame of this thesis has been performed with this code. At first, this section outlines the general reconstruction procedure performed by *Echidna*, followed by a description of all parameters used in the analysis. For a detailed description of the *Echidna* reconstruction steps, see [15].

3.3.1 Event processing

The raw events recorded by DAQ contain information on time and charge of each PMT hit. In the process of data reconstruction, first of all an electronics pre-calibration is performed with calibration events from laser, LED and pulser hits. These account for the first 1000 events of each normal run and are also injected into DAQ with a rate of 0.1 Hz . In addition, special calibration runs are performed

after each modification of electronics and at least every week. By means of the precalibration and channel calibration, the raw events undergo the first reconstruction step, i.e. decoding. A full list of decoding steps can be found in [15]. The decoded hits still contain a great amount of PMT dark noise. Thus, the next step in data processing is the identification of real physical events in contrast to mere dark noise background. The clustering module of *Echidna* searches for groups of time-correlated decoded hits. The ID clustering algorithm can identify up to three clusters within the $7.5 \mu s$ time gate. In general, only one cluster is found, but in the case of fast coincidences (like ^{212}Bi - ^{212}Po and ^{85}Kr - ^{85m}Rb) or accidental pile-up, more than one cluster may be detected. The efficiency of the clustering algorithm was checked by means of random triggers and found to be nearly 100% [34]. Events without a cluster are most likely no real physical events. Clusters form the basis of further event reconstruction like position of the interaction vertex, energy, pulse shape and many more.

The same procedure is also applied for the OD, with the difference that the OD clustering module is limited to the detection of one cluster. Considering that only muons trigger the OD, more than one cluster in a time gate of $\sim 8.5 \mu s$ is unlikely.

3.3.2 Software parameters of analysis

The *Echidna* data structure provides a large amount of information from single PMT hits up to numerous properties of reconstructed clusters. A full presentation of the whole *Echidna* data structure would go beyond the scope of this diploma thesis. Hence, the description of *Echidna* parameters focus on the relevant parameters used for data analysis performed in Chapter 5. All parameters concerning the ID are designated in the data structure as “laben”-parameters, referring to the *Laben S.p.A.* company which provided the digital boards for the digitalization of charge and time information of every PMT hit in the ID. Software parameters of the OD are designated as “muon”-parameters in the *Echidna* code.

Event properties

The *General Borexino Trigger* (GBT) condition is met if either the ID or the OD trigger are activated. In this case, the full detector is read out and data written to the data base. The activation of the GBT condition is designated as an *event*. Recorded *events* are not necessarily real physical events but can also be service trigger pulses or caused by electronics problems.

- Trigger type (*trigger.trgtype*):
The parameter *trigger.trgtype* identifies the type of a detected *event*. Calibra-

tion triggers (*trigger.trgtype* == 32), artificially random generated triggers (*trigger.trgtype* == 64) and laser (timing) and LED triggers (*trigger.trgtype* == 8) pose the Borexino service triggers and are injected into DAQ for detector maintenance and performance studies. Any event within Borexino which is not caused by these artificial triggers is recorded as trigger type 1 respectively 2. Trigger type 2 corresponds to an event which occurred only in the OD, e.g. a muon crossing the periphery of the Borexino WT. However, any event triggering the ID is recorded as trigger type 1, even if the OD triggered too. Neutrino events detected by Borexino are therefore designated as trigger type 1, as well as any radioactive decay within the ID or muons crossing the whole detector. To distinguish neutrino events from these background sources, additional software parameters are necessary.

- Number of reconstructed clusters by the ID clustering algorithm (*laben.n_clusters*):
As stated above, in general events are reconstructed with only one cluster, except for fast coincidences and accidental pile-up in the trigger time gate. Events without any cluster are most likely no actual physical event.
- Number of functional signal channels of the ID (*laben.n_live_pmts*):
This parameter provides the number of active signal channels during data taking. Due to malfunction of PMTs or electronics, the number of fully functional signal channels may vary between different runs. A reduced number of channels results in a reduced number of detected photons of an event. For calculation of the real energy of an event, one has to correct for the active number of signal channels. Usually, all events are normalized to 2000 active channels.
- GPS time information (*trigger.gpstime*[]):
Any event is recorded with its GPS time for coupling events to absolute time. This is necessary in case of a supernova explosion or analysis on events which are correlated in time. The precision of the GPS time is several μs .

Inner Detector Cluster properties

The following properties concern events which feature at least one cluster identified by the ID clustering algorithm. Only in exceptional cases an event contains more than one cluster, like very fast delayed or accidental coincidences.

- Number of hits (*laben.clusters[].nhits*):
The *nhits* parameter of a cluster is the number of hit PMTs associated to the cluster. In this thesis this parameter is normalized to 2000 PMTs using the *laben.n_live_pmts*, as stated above.

- Charge (*laben.clusters[].charge*):
An event is detected by its emitted photons, which are recorded by the PMTs. Each photon hitting a PMT creates one photoelectron. Photoelectrons are multiplied in the dynodes of the PMT and eventually the multiplied charge is collected. The multiplication of the initial photoelectrons is a statistical process, however the mean multiplication factor of a single photoelectron can be determined. By dividing the total measured charge at the PMT by this mean multiplication factor, one obtains the number of initial photoelectrons of the event. The *charge* parameter provided by *Echidna* is the number of photoelectrons of a hit, determined in this way.
The *charge* of a whole cluster is the sum of deposited *charge* of all hits within the cluster. In this thesis, *charge* will always refer to the total number of photoelectrons (pe) within a cluster. This parameter is normalized within this thesis to 2000 PMTs using the *laben.n_live_pmts*, as stated above.
- Charge of PMTs with light concentrators (*laben.clusters[].charge_conc*):
charge_conc is the sum of deposited *charge* (see above) of only those clustered hits, which were detected by one of the 1838 PMTs with light concentrator. This parameter is normalized within this thesis to 2000 PMTs using the *laben.n_live_pmts*, as stated above.
- Position reconstruction (*laben.clusters[].position_dbn.x y z*):
Four different reconstruction algorithms are present in the *Echidna* code. A crude *baricentrator* code computing the geometrical center of an event, has been used as starting point by other algorithms. The three sophisticated position reconstruction algorithms used in the *Echidna* data structure are the *Milan* [15], *Moscow* [15] and *Dubna* [15] codes. All three reconstruction codes are subjected to continuous development and improvement, and have been checked on reliability by means of simulations. All three codes have proven themselves and are consistent among each other. The position reconstruction code used in this diploma thesis is the *Dubna* code.
- Cluster mean time (*laben.clusters[].meantime*):
This variable provides the mean time of all hits of a cluster in relation to the cluster start time.
- Tail to total (*laben.clusters[].tailtot[i]*):
The *tailtot* variable is derived by a pulse shape analysis of the hit time distribution of the cluster. The pulse is first integrated over the whole distribution and then compared with an integration over a part of it. In this thesis the variable *tailtot[3]* is used which compares the tail above 100 ns with the whole distribution.

Outer Detector Cluster properties

The main task of the OD is the identification of muons by their Cherenkov light emission in the pure water of the WT. In addition, the OD has been subject to programming work on a muon track reconstruction algorithm. This code was not part of the *Echidna* code during the analysis performed within this thesis. However the code was implemented manually to the analysis programs created within this thesis and has been successfully applied in the analysis on neutrons and cosmogenic background in chapt. 5.

- Muon Identification (*muon.has_cluster*):
The OD clustering algorithm checks the OD PMTs for a group of time-correlated hits and identifies in this manner muons with an efficiency of at least 99.9% [11].
- Muon track reconstruction:
No official component of the *Echidna* code during the analysis performed within this thesis. The general procedure of the algorithm is outlined in sec. 4.4.1 [46].

Declared parameters of data analysis

Besides official parameters present in the continuously developing *Echidna* data structure, additional variables were defined on basis of these parameters for data analysis within this thesis. They are based on the characteristic light emission of muons, and are used in analysis to identify muons crossing the ID, which were not identified by the OD.

- Deutsch parameter:

$$Deutsch = 1 - \frac{charge_conc}{charge} \quad (3.1)$$

The *Deutsch parameter* provides a measure of eccentricity of an event within the ID. The 1838 PMTs with light concentrator cones are focused on the *Inner Vessel* (IV) and therefore don't register events far outside, in contrast to the 374 PMTs without concentrator cones. Comparing the detected charge of the PMTs with light concentrator (*charge_conc*) to the total detected charge (*charge*) one can identify events producing light outside the center, like muons crossing the ID at its boarder. For more details on this parameter in muon identification, see 5.2.2.

α , β and ν events are point-like light sources in the IV. Outside the IV, light emission of these events is strongly suppressed as result of quenchers in the buffer liquid (see sec. 2.3.1). The *Deutsch parameter* results in values below ~ 0.18 for these events. On the other hand, muons traversing the detector emit a huge amount of light due to scintillation and Cherenkov effect along their track. This eccentric amount of produced light is registered by the PMTs without cone. A detailed study of the efficiency of this parameter can be found in [11].

- “Strange” events flag:

As will be described in sec. 4.4.1, the *charge* value of muons can significantly differ from the charge expected via the value of *nhits* of the event. On the basis of the Poisson distribution, the expected charge ($charge_{exp}$) and number of hits (*nhits*) of an event are connected via the correlation:

$$charge_{exp} = -n_{live_pmts} \cdot \log\left(1 - \frac{nhits}{n_{live_pmts}}\right) \quad (3.2)$$

Events with a *charge* value that strongly differs from $charge_{exp}$ have a distorted charge information and are classified as “Strange” events.

Chapter 4

Solar neutrino fluxes and cosmogenic background

With the first real-time spectral measurement of ${}^7\text{Be}$ neutrinos [34], Borexino has proven its excellent capability to perform spectroscopy on sub-MeV solar neutrino fluxes. Further effort is currently performed in order to determine the remaining solar neutrino fluxes, i.e. from the pp/pep fusion processes, from the three neutrino emissions of the CNO cycle as well as the low energy part of the ${}^8\text{B}$ branch.

As presented in this chapter, the main background source for the more energetic fluxes from pep , CNO and ${}^8\text{B}$ is caused by muon-induced radionuclides, so called cosmogenic background. A muon beam experiment has been performed at CERN [47] in order to determine production rates of cosmogenic radionuclides. A short description and the results are outlined in this chapter. The experiment pointed out, that the main cosmogenic background in Borexino arises from two Carbon isotopes ${}^{11}\text{C}$ and ${}^{10}\text{C}$. The *Three-Fold Coincidence* (TFC) technique, a method developed to suppress these cosmogenic radionuclides, is described in detail. The technique is based on tagging cosmogenic background in coincidence with a muon and subsequent neutrons. The experimental signature of both particles within data acquisition is outlined in the end of the chapter.

4.1 The pp/pep , CNO and ${}^8\text{B}$ solar neutrino fluxes

4.1.1 Physics goals

pp/pep flux

The major contribution to the solar neutrino luminosity arises from the pp fusion process producing 91% of the total neutrino flux. A direct measurement of the pp flux would constrain the total neutrino luminosity to a great

extent. The comparison between the neutrino and photon luminosity yields a crucial check of the Sun's stability over a time scale of $10^5 - 10^6$ years. Moreover it could probe the validity of the *Standard Solar Model* (SSM) energy production schemes which are based on thermonuclear energy production and the Sun being in a quasi-steady state [15].

As mentioned in sec. 1.3.2, the pp and pep solar neutrino fluxes are directly related. Their relative ratio is only weakly model dependent and theoretically known to a good accuracy. Therefore, a measurement of the pep flux would determine the fundamental pp flux with high precision. Moreover the monoenergetic pep neutrinos with an energy of $1.44 MeV$ are located directly in the expected transition region between vacuum- and matter-dominated oscillations according to the MSW-LMA oscillation solution [14] (see sec. 1.2.2 and 1.3.3). The expected signal of the monoenergetic pep neutrinos in Borexino is a Compton-like electron-recoil spectrum extending to $1.22 MeV$ and can be used to test the predictions of this neutrino oscillation model.

***CNO* flux**

The fusion rates of the *CNO*-cycle in the Sun is highly temperature dependent and almost undetermined. The measurement of *CNO* neutrinos would provide information on the contribution of the *CNO*-cycle to solar energy production and the *CNO*-cycle itself. In the Sun, the *CNO* cycle contributes only with about 2%. However, it is the major energy production mechanism in heavy stars larger than a few solar masses.

The fraction of energy released in a star by the *CNO* cycle is also a measure of its age. Therefore the *CNO* cycle plays a key role in the age estimation of globular clusters, and is thus essential in setting a lower limit for the age of the universe [48].

8B flux

Spectral measurements of 8B neutrinos have been already performed by the Cherenkov detectors SNO [22] and Super-Kamiokande [21] (sec. 1.4.2). Both detectors are based on the detection of Cherenkov light emitted by electrons which were scattered by neutrinos. As a result of the low light yield and the high radioactive background of both detectors, $^8B-\nu$ have been measured only above an energy of $5.5 MeV$. A spectral measurement of $^8B-\nu$ below $5 MeV$ is of great interest as a spectral deformation is expected due to the MSW-LMA effect.

As described in the next section, cosmogenic background is the main background source for the high energetic solar neutrino fluxes, i.e. pep , *CNO* and 8B

dominant ν -flux	energy range	ν -rate (SSM)
${}^7Be-\nu$	250 – 800 keV	~ 50
pep - & $CNO-\nu$	0.8 – 1.4 MeV	~ 1.5
${}^8B-\nu$	2.8 – 5.5 MeV	~ 0.53

Table 4.1: Expected ν -rates within the three neutrino windows in counts per day and 100 t according to the SSM [47].

fluxes. With respect to this diploma thesis on cosmogenic background, only these three higher-energetic neutrino fluxes are addressed in the further course of this thesis.

4.1.2 Signal and background sources

The energy spectrum in Borexino is divided in three main energy regions according to the neutrino fluxes most prominent within these regions (see Table 4.1). As one can easily see, due to the low event rates the detection of pep/CNO and 8B neutrinos is challenging. Therefore, intense control of background contributions is necessary in order to accomplish a measurement of these fluxes. The background consists of internal radioactivity, external γ -ray background as well as radioactive elements produced by cosmic muons within the detector, so called cosmogenic background.

Due to the ultrahigh purification standards of Borexino, the internal radioactivity fulfills the requirements to detect the given neutrino fluxes. The radiopurity level is less than $< 2 \cdot 10^{-17} g/g$ in ${}^{238}U$ and $< 0.3 \cdot 10^{-17} g/g$ in ${}^{232}Th$ [34]. However, the natural isotopic abundance of radioactive ${}^{14}C$ in the scintillator can not be reduced by means of purification. With a 156 keV β decay, the high ${}^{14}C$ rate sets the energy threshold for neutrino detection to 200 keV , as can be seen in Figure 4.1.

The external γ -ray background originates from the construction materials of the detector and from the surrounding rock. In Borexino this problem was addressed by using radiopure buffer materials to screen the environmental radioactivity as well as construction materials of extremely low radioactivity. ${}^{208}Tl$, present in the glass of the photomultiplier tubes (PMT), emits a 2.6 MeV γ in its decay and enlarges the γ -induced background in the pep/CNO - and 8B -window. The higher-energetic neutrino fluxes are therefore subject to a larger γ background than ${}^7Be-\nu$. This can be solved by redefining the fiducial volume for the measurement of the higher energetic neutrino fluxes. Considering the 100 t fiducial mass used for ${}^7Be-\nu$ measurement, an external γ background of 1 event per day is expected

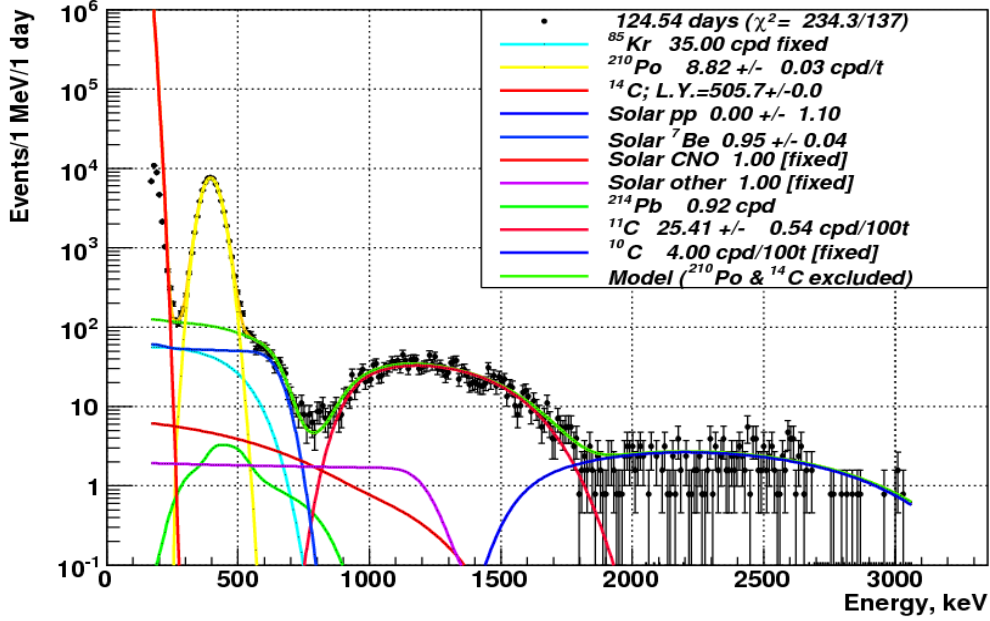


Figure 4.1: Fit of the energy spectrum of Borexino. The rates of solar pep -, CNO - and 8B - ν fluxes are fixed to the expectations according SSM and MSW-LMA oscillation solution [9]. Free solar fluxes in the fit are 7Be - and pp - ν . Radioactive background arises from ${}^{85}Kr$ [fixed], ${}^{210}Po$, ${}^{214}Po$ and ${}^{14}C$. The huge β -decay spectrum of ${}^{14}C$ is used to determine the light yield (L.Y.) in the low energy region of the spectrum. Cosmogenic background is mainly caused by ${}^{11}C$ and ${}^{10}C$. The spectral fit applies a single β^+ -decay spectrum to describe ${}^{10}C$ and the external γ -background from ${}^{208}Tl$, fixed to a combined total rate of $4 \text{ counts day}^{-1} (100 \text{ t})^{-1}$ [50].

within the pep/CNO window. Reducing the fiducial mass to 70 t , the increased self-shielding would lower the background by a factor of 10 while losing only 30% of the signal [33, 49].

However, the most prominent background source for pep , CNO and 8B neutrinos comes from cosmically induced radionuclides. High energetic muons produced in the atmosphere can traverse the shielding provided by the rock and induce reactions in which radioactive elements are produced within the Borexino detector.

Taking a look at Borexino data (Figure 4.1), one can see that the pep/CNO window is dominated by cosmogenic ${}^{11}C$. With a rate of $\sim 26 \text{ counts day}^{-1} (100 \text{ t})^{-1}$ [50], the ${}^{11}C$ exceeds the expected ν -signal rate of $\sim 1.5 \text{ counts day}^{-1} (100 \text{ t})^{-1}$ (Table 4.1) by an order of magnitude. Therefore, it is necessary to handle cosmogenic

background in order to perform a reliable measurement of the higher energetic neutrino fluxes.

4.2 Cosmogenic radionuclide background

In the *Laboratori Nazionali del Gran Sasso* (LNGS) at a depth of 3800 m.w.e. (meter water equivalent), the atmospheric muon flux is reduced by a factor of 10^6 relative to the surface. However, with a rate of 1.1 muons $m^{-2} h^{-1}$ corresponding to $\sim 10^4$ muon events per day in the detector, it is still significant. This residual muon flux induces electromagnetic and hadronic cascades, mainly consisting of γ -rays, electrons, neutrons, protons and π mesons. By interacting with the scintillator mass, the muon and its secondaries can produce radioactive nuclides within Borexino. Because of the very low signal rate of *pep*, *CNO* and 8B neutrinos, this cosmically-induced background is a serious problem.

4.2.1 Muon beam experiment at CERN

At the end of the 90s, a target experiment at CERN has been performed [47] in order to determine the production rate of cosmogenic radionuclides expected in the Borexino detector. A muon beam was focused on 240 cm of concrete in which the muon shower was built up, followed by 200 cm of water and a set of scintillator detectors. Therefore, the experimental setup simulated the main material properties of Borexino at the underground site of Gran Sasso. The muon beam was operated at two different energies (100 GeV and 190 GeV) to enable the extrapolation of the energy dependence of the measured cross sections to 320 GeV, the average muon energy at the LNGS site. The results of this experiment are shown in Table 4.3 with the three main neutrino windows considered separately.

These results show that cosmogenic background plays only a minor role in 7Be - ν detection, but it is crucial for *pep*- & *CNO*- ν detection and - though to a much smaller extent - also for 8B - ν detection. The two Carbon isotopes ${}^{11}C$ and ${}^{10}C$ make up almost entirely the cosmic induced background within the *pep*/*CNO* and the 8B window.

As a result of its very high rate compared to the expected ν -signal, special interest is directed towards the ${}^{11}C$ contribution. ${}^{11}C$ has been studied in the *Counting Test Facility* (CTF) [32, 33] and in simulations performed with FLUKA [51, 49, 33], a code to describe both hadronic and electromagnetic interactions up to 20 TeV. Both studies agree with the CERN experiment within 1σ .

Comparing the ${}^{11}C$ -rate of $\sim 15 \text{ counts day}^{-1} (100 t)^{-1}$ determined by the CERN

Isotope	^{12}B	^{11}Li	8He	9C	9Li	8B	6He	8Li
$T_{1/2}$	0.02 s	0.09 s	0.12 s	0.13 s	0.18 s	0.77 s	0.81 s	0.84 s
Isotope	^{11}Be	^{10}C	^{11}C	7Be	^{10}Be			
$T_{1/2}$	13.80 s	19.30 s	20.38 m	53.3 d	$1.5 \cdot 10^6 a$			

Table 4.2: Half-life times of all radioactive isotopes, which can be produced by muons and their secondaries in organic scintillator (^{12}C targets) [47].

Isotope	full range	250 - 800 keV $^7Be-\nu$	0.8 - 1.4 MeV $pep/CNO-\nu$	2.8 - 5.5 MeV $^8B-\nu$
$^8He + ^9Li$	0.034 ± 0.007	$< 6.8 \cdot 10^{-4}$	$< 1.0 \cdot 10^{-3}$	< 0.014
9C	0.077 ± 0.025	0	0	0.016 ± 0.005
8B	0.11 ± 0.02	0	$(3.3 \pm 0.6) \cdot 10^{-5}$	0.020 ± 0.004
6He	0.26 ± 0.03	0.040 ± 0.004	0.07 ± 0.01	0.011 ± 0.001
8Li	0.070 ± 0.017	$(2.5 \pm 0.6) \cdot 10^{-4}$	$(8.0 \pm 2.0) \cdot 10^{-4}$	0.020 ± 0.005
^{11}Be	< 0.34	$< 4.3 \cdot 10^{-4}$	$< 1.0 \cdot 10^{-4}$	< 0.01
^{10}C	1.95 ± 0.21	0	0	0.56 ± 0.06
^{11}C	14.55 ± 1.49	0	7.36 ± 0.75	0
7Be	0.34 ± 0.04	0.34 ± 0.04	0	0
Total sum	~ 17.4	~ 0.38	~ 7.4	~ 0.65
ν -rate (SSM)		~ 50	~ 1.5	~ 0.53

Table 4.3: Expected muon-induced background and solar neutrino rates within the different energy ranges defined by the neutrino windows (see Table 4.1). The rates are stated in counts per day and 100 tons [47]. Half-life time of cosmogenic radionuclides are listed in Table 4.2.

experiment [47] with current spectral fits in Borexino of $\sim 26 \text{ counts day}^{-1} (100 t)^{-1}$ shown in Figure 4.1, a discrepancy has to be noted. The quality of the spectral fit of the ^{11}C -spectrum over two orders of magnitude leaves no hint of unknown background sources in Borexino. Therefore, it stands to reason that this difference originates from the larger dimension of the Borexino detector (nearly 300 tons of scintillator liquid) in which electromagnetic and hadronic cascades can develop to a larger degree. The CERN experiment, as well as the FLUKA simulation or the direct measurement in the CTF were performed on the basis of a much smaller exposed target mass (CERN: $< 11 \text{ kg}$; CTF & FLUKA simulation: $4 t$).

4.3 The Three-fold Coincidence technique

The very short-lived radioactive nuclides shown in table 4.2 have a half-life time of less than 1 second, and can be easily tagged with their parent muon. By discarding the first 2 seconds after each muon, this background can be suppressed by a factor of 10 for the $pep/CNO-\nu$ window and by a factor of 3 for the $^8\text{B}-\nu$ window, losing only $\sim 10\%$ of active data taking time. Thus, the only relevant radioactive nuclides left within these two ν -windows are ^{10}C and ^{11}C , which decay with mean lifetimes of 27.84 s and 29.40 m , respectively. Due to a muon rate of ~ 5000 per day within the *Inner Detector* (ID), these events cannot be discarded by applying a deadtime cut after each muon without blinding out the whole detector. In order to suppress these background sources an event-by-event tagging has to be applied.

4.3.1 Tagging of ^{11}C and ^{10}C

First proposed in the 90s by Martin Deutsch [52], the *Three-Fold Coincidence* (TFC) technique is based on the assumption that, no matter how the muon induced shower develops, obtaining Carbon isotopes out of a ^{12}C atom requires to knock off at least one neutron. According to this, the net reactions for ^{10}C and ^{11}C are:



The free neutrons travel a range of a few dozen cm until it is fully thermalized in the scintillator. Eventually after $\sim 250 \mu\text{s}$ the neutrons are captured on Hydrogen, emitting a characteristic 2.2 MeV γ -ray [15, 33, 32].



Neutrons can also be captured on ^{12}C emitting γ -rays with a combined energy of 4.9 MeV . However, the cross section for this reaction is two orders of magnitude lower than the neutron capture on Hydrogen. The coincidence of a muon

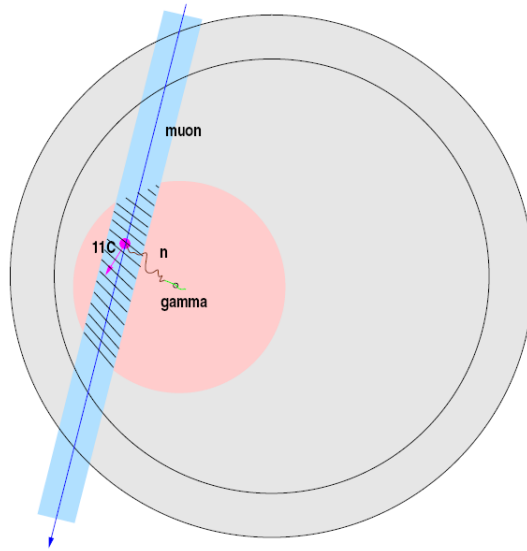


Figure 4.2: Schematics of first and second level suppression of cosmogenic background by means of the TFC technique [15].

followed by a neutron capture γ flags the production of cosmogenic radionuclides, in particular the production of Carbon isotopes.

4.3.2 Background suppression

First level suppression

After identification of such a $\mu - n$ -coincidence, a first level suppression of the produced radionuclides can be achieved by blinding out a spherical volume of radius r around the reconstructed position of the γ for a given time window t , as depicted in Figure 4.2. The time window t should be equal to a few times the mean lifetime of the respective radionuclide. The radius r should be considered with respect to the mean distance between the reconstructed $\gamma_{2.2\text{ MeV}}$ position and the radionuclide. This mean distance is composed of:

- The mean free path of neutrons produced along with radionuclides until thermalization ($\sim 40\text{ cm}$) [49].
- The mean free path of the neutron capture γ of about $20\text{-}30\text{ cm}$ [15], which is reconstructed by the position reconstruction algorithm approximately in the middle of the track.

- Convective currents on the time scale of t , which can displace the radionuclide. Due to a temperature gradient in the whole detector of about 4 K , there are no convective currents even on the time scale of several days in Borexino .

Second level suppression

In addition to the γ also the parent muon can be used to tag possible cosmogenic radioactive nuclides. Considering that cosmogenic radionuclides are only produced within a given radius around a muon track, one can define a cylinder whose axis is taken along the track. Only the intersection of this cylindrical volume with the sphere defined around the reconstructed γ is blinded out (see Figure 4.2). Thus, the fraction of data loss can be reduced significantly.

4.4 Signatures of muons and neutron capture gammas within DAQ

As stated in the previous chapter, the tagging of muon induced ^{11}C and ^{10}C is based on the muon and the γ which is emitted in the neutron capture process. This section provides a description of the identification and special features of these particles within data acquisition.

4.4.1 Muons

After passing the Gran Sasso rock shielding, muons enter the LNGS site with a rate of $1.1\text{ m}^{-2}\text{ h}^{-1}$ and mean energy of $\langle E_\mu \rangle = 320\text{ GeV}$, corresponding to an exposure of 5000 muons per day to the ID of Borexino. 99.9% of these muons are identified by the Outer Detector (OD) clustering algorithm (see sec. 3.3.2). However, muons crossing the ID show very distinctive features which can be used for identification, further increasing the already remarkable efficiency of muon detection.

For minimal-ionizing particles like muons, the characteristic energy deposition is about 2 MeV/cm in the scintillator ($\rho = 0.89\text{ kg/l}$). Thus, a muon passing through the *Inner Vessel* (IV) produces a huge amount of scintillation light and saturates immediately all 2212 PMTs. These events are usually identified by their very high energy (*charge* variable at several tens of thousands photoelectrons; *nhits* at saturation of all fully functional PMTs; parameter description in sec. 3.3.2). However, the huge signal from a muon can cause problems in the data acquisition process, i.e.:

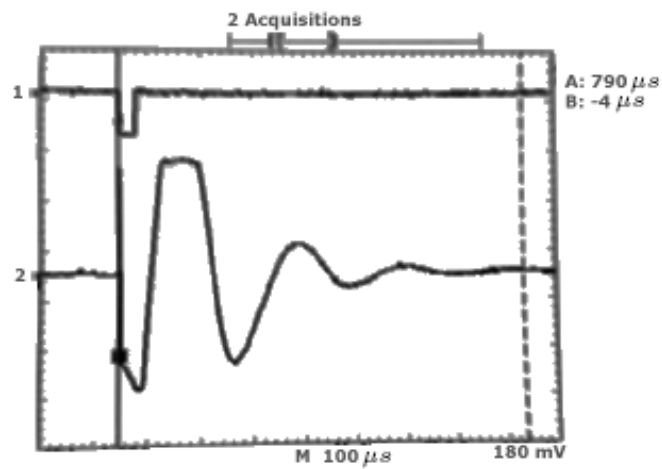


Figure 4.3: The oscilloscope is triggered on the logic signal of the *Muon Trigger Board* (MTB) (see sec. 3.2.1), which flags muon detection in the OD. Channel 1 shows the MTB signal, whereas channel 2 monitors the integrator output behavior of a single channel after a detected muon pulse. It takes several hundreds of μs to stabilize the integrator output. The *charge* information of these muon events is distorted and not reliable. These fluctuations can even influence the *charge* determination of muon-induced neutron events [44].

- Distortion of the charge variable:

As shown in Figure 4.3, after a muon crosses the scintillator, a huge pulse is generated in the *Front-End* (FE) boards, which is followed by a large overshoot. The channel's integrator output, used to determine the *charge* of an event, oscillates around the baseline for a time of up to several $100\ \mu\text{s}$. Thus, the integrated signal produces very distorted values of the charge variable of the muon event. On basis of the long oscillation time, this affects also neutron capture gammas which occur $\sim 250\ \mu\text{s}$ after muons producing ^{11}C and ^{10}C . However the variable *nhits* of these γ -events is still reliable. For a description of the software parameter used in this analysis see sec. 3.3.2.

- Afterpulses following a muon:

Scintillation light generated by a muon produces a large amount of photoelectrons within the PMT. In the process of this massive photoelectron multiplication along the dynodes, residual gas atoms within the PMT can be ionized. Because of their high mass, the charged atoms move only slowly within the electric field of the dynodes. According to the position where the atom was ionized, several different path lengths are possible and therefore several different drift times. After a prompt signal from the photoelectrons, delayed signals from ionized gas atoms occur in the PMT producing fake events in the DAQ, so-called muon afterpulses.

To handle these afterpulses the *Borexino Trigger Board* (BTB) code has been modified. After the detection of a muon by the OD *Muon Trigger Board* (MTB), the threshold for events in the ID is greatly increased for a few ms. Due to the higher threshold afterpulses are not recorded anymore by the system. However, this does not count for the neutron analogue trigger described in sec. 3.1.2. This trigger suppresses these afterpulses by applying a $25\ \mu\text{s}$ lower time limit following the muon itself (see also sec. 4.4.2).

Another type of muon events are muons traversing only the buffer liquid. Because of the quencher added to the buffer liquid the scintillation light is dampened by a factor of ~ 20 . These muons are recorded with a much smaller energy than muons crossing the IV itself. Simulations [53] within the Borexino collaboration indicate that even these muons still produce a high amount of light, and thereby are distinguishable to neutrino signals. However, muons crossing the ID near its border, i.e. behind the PMTs, have a quite high chance of being recorded by the DAQ with a visible energy comparable to a neutrino signal.

Identification of muons

In order to identify these muons in addition to the OD, several properties of a muon signal within the ID can be used. For the analysis described in Chapter 5, the following muon identification cuts have been performed (for description of the variables used, see sec. 3.3.2):

- *Outer Detector clustering:*
The OD clustering algorithm identifies 99.9% of all muons [11].
- *Cluster mean time:*
Muon signals (as well as α signals) show a very broad time distribution compared to β/γ like events (e.g. neutrinos from the Sun). Therefore by applying a cut on the mean time, muons (and α events) can be tagged.
- *Deutsch parameter:*
As described in Section 3.3.2, the *Deutsch parameter* identifies light contributions external to the *Fiducial Volume* (FV), especially muon tracks.
- *“Strange” events:*
As already noted above, the determined charge of muons can greatly differ from the expected charge (*charge*) on the basis of detected number of hits (*nhits*). Therefore, the ratio of reconstructed charge to measured charge serves especially to identify muons.

Muon track reconstruction

Based on the OD, a reconstruction algorithm for muon tracks passing Borexino [46] has been developed. The code used in this thesis is one of the first versions (date: November 2007). The muon track reconstruction algorithm identifies clusters of PMT hits in the OD according to their time and position. The algorithm selects the first cluster on the *Stainless Steel Sphere* (SSS) as entry point. The exit point is chosen to be the largest cluster either on the bottom of the SSS or on the floor. If no cluster is found, the algorithm searches for this cluster on the whole sphere. If there is only one cluster present on the sphere, the algorithm tries to split this into two smaller ones. By identifying the entry and exit point, the muon track is defined.

This muon track reconstruction is used for the analysis of neutrons and ^{11}C described in Chapter 5 by applying the TFC technique. In addition a validity check of the muon track reconstruction itself has been performed and is stated in Section 5.4.8.

4.4.2 Neutron capture gammas

Several problems in the first stage of Borexino data taking hindered the detection of gammas emitted in the process of neutron capture (see eq. (4.3)). Most of the problems have been solved by now, however work on the neutron detection ability of Borexino is still in progress. A summary on current improvements of the Borexino's neutron detection capability is outlined in Chapter 7. The following section covers the status of neutron detection in the time period of 07/10/07 until 10/27/07. Data taken during this time period is the basis of the analysis presented in Chapter 5.

Identification of neutron capture gammas

Gammas produced in the neutron capture process on Hydrogen (or Carbon isotopes) of the scintillator molecules are identified by the neutron analogue trigger depicted in Section 3.1.2. Events within a time window of $[25,800] \mu s$ after the muon and an energy larger than $\sim 300 keV$ activate this neutron trigger. The $25 \mu s$ lower time limit prevents the major portion of muon afterpulses to be recorded in the neutron time window. Nevertheless, about 10% of all neutron events have a non negligible amount of afterpulse hits in this time gate. These neutrons have badly reconstructed spatial positions, though they can be identified by their large mean time caused by the broad time distribution of afterpulse hits. A mean time cut of more than $100 ns$ identifies these badly reconstructed neutrons quite good (no efficiency study performed yet).

In general, the *charge* value of all neutron candidates is spoiled, regardless whether afterpulses occurred or not (as described in sec. 4.4.1). The *nhits* variable gives reliable values for neutron events which are not affected by the afterpulses.

Three Fast Trigger Coincidence Veto

The *Three Fast Trigger Coincidence* (TFTC) veto is activated when 2 triggers are fired less than $\sim 200 \mu s$ apart. When this condition is met, the veto prohibits any additional trigger within the next $\sim 2 ms$.

This has a dramatic consequence for muon-induced showers, which can produce several neutrons at once (up to more than hundred neutrons). The higher the neutron multiplicity of an event, the higher the probability of a neutron capture process within $200 \mu s$ ($\tau_n \sim 250 \mu s$) after the muon. Consequently, the activation of the TFTC veto prohibits the detection of any other neutrons. Hence it follows, that with a neutron time window of $800 \mu s$ after a muon, the neutron trigger can detect 3 neutrons at best.

Since most of the neutrons are not detected, this states a serious problem in applying the TFC technique (as stated in sec. 4.3) in order to discard the cosmogenic radionuclide ^{10}C and ^{11}C .

However, for the determination of the rates of these two radionuclides, it is not necessary to detect all shower induced neutrons. The analysis concerning ^{11}C identification is described in the next chapter.

Chapter 5

Analysis and results

As outlined in the previous chapter, the tagging of muon-induced ^{11}C and ^{10}C background is the most critical issue for detection of the high energy part of the solar neutrino spectrum, i.e. the *pep*-, *CNO*- and ^8B - ν energy region. The *Three-Fold Coincidence* (TFC) technique described in Section 4.3 is a powerful method to reject these cosmogenic radionuclides. Therefore its efficiency is of great interest. On this account, a detailed study on the feasibility of the TFC technique in Borexino has been performed within this diploma thesis. On basis of the TFC, correlations between muon, neutron capture γ and cosmogenic ^{11}C were studied. The analysis is based on data taken by Borexino between 07/10/07 and 10/27/07 and spans an active measuring time of 54 days. With the given data set, analysis on ^{10}C is not feasible due to its low production rate of $\sim 2 \text{ counts day}^{-1} (100 \text{ t})^{-1}$ (see Table 4.3 in sec. 4.2). However, an outlook on the main features of a possible ^{10}C analysis based on more statistics is given in Chapter 7.

First of all the preparation of data and event selection, are described in the first two sections of this chapter. The next three sections present the results of analysis concerning the participating particles of TFC technique: neutron, muon and cosmogenic radionuclide ^{11}C .

The section about neutrons outlines the general problem of multi-neutron showers in Borexino and their identification in data analysis. Furthermore, properties of neutrons are analyzed and presented, i.e. measured energy distribution, decay time, as well as the spatial distribution with respect to the parent muon.

The next section covers the analysis performed on the cosmogenic radionuclide ^{11}C . First, the production channels of ^{11}C within muon-induced showers are presented and intrinsic inefficiencies of the TFC technique due to so-called “invisible” channels is pointed out. As a result of analysis artifacts, the time distribution of signal and background is convoluted with additional contributions. A model to describe the convoluted distribution was developed within this thesis and is dis-

cussed in detail.

Afterwards, ^{11}C is analyzed with respect to its knock-off neutrons and to its parent muon. Spatial correlations and time distributions of these pairs provide a wide range of information on details of the TFC. Correlations in space allocate the mean free path of neutrons as well as the mean distance between muon and ^{11}C . On the other hand, by means of the time distribution, the ^{11}C decay time is fitted and its rate determined. Eventually, the comparison between the rate obtained by neutron- ^{11}C and muon- ^{11}C correlations provides an excellent test of consistency and the reliability of TFC technique. Finally, the TFC technique is applied to discard ^{11}C from data, and the variation of the spectrum examined.

5.1 Data set preparation

The analysis presented in this chapter is performed on data taken by Borexino between 07/10/07 and 10/27/07. From this data some runs had to be removed due to various problems in data acquisition (DAQ). The selected data was filtered removing the following types of events:

- Calibration events

The first 1000 events of a run consist of laser and pulser events for detector calibration. After this initial calibration, these events are still injected with a rate of 0.1 Hz into the system in order to observe the detector response stability. These events, as well as complete calibration runs are discarded from the data set.

- ^{214}Bi and ^{214}Po decays

When air is introduced in ultrapure scintillator, a contamination by ^{222}Rn is inevitable. The Radon contamination results in several radioactive daughter elements according to the ^{238}U -chain.

In July 2007, during a temporary refilling procedure due to temperature changes within the detector, ^{222}Rn entered the *Inner Vessel* (IV) of Borexino. The α -decay of Radon (5.49 MeV) is quenched to an energy well below the *pep/CNO* energy window of $0.8\text{-}1.4\text{ MeV}$. However, its radioactive daughter elements produce background within this window. The most important contribution arises from ^{214}Bi , which deposits up to 1.51 MeV energy in the detector by its β -decay.

Fortunately, ^{214}Bi can be tagged by its fast coincidence with its daughter element ^{214}Po :





Both decays can be discarded by identification of a coincidence of two events less than $708 \mu\text{s}$ ($3 \cdot \tau({}^{214}\text{Po})$) apart and of appropriate energies. The *charge* value of ${}^{214}\text{Po}$ candidates has to be within $[150,500] \text{ pe}$, while the *charge* range for ${}^{214}\text{Bi}$ candidates is $[100,2000] \text{ pe}$. The 100 pe *charge* threshold prevents accidental coincidences with the intrinsic scintillator radioactivity from ${}^{14}\text{C}$.

After removing these types of events the resulting data set spans an active measuring time with fully functional neutron trigger of 54.04 days.

5.2 Event selection

The declaration of muon, neutron and radionuclide (${}^{11}\text{C}$, ${}^{10}\text{C}$) events is based on several identification criteria listed in this section. The analysis performed in this thesis is based on the offline data processing code *Echidna* [15], which has been developed by the Borexino collaboration. *Echidna* and all variables used for the event selection are described in Section 3.3.2.

5.2.1 General criterion

The variable *laben.n_clusters* provides the number of clusters which an event contains. Events without cluster do not have any physical meaning and are neglected therefore in the course of the analysis.

5.2.2 Criteria for muon identification

As described in Section , muons can be identified not only by the OD clustering algorithm but also by the ID on the basis of their characteristic light emission and influence on electronics. The parameters used for muon identification are described in Section 3.3.2. An event is identified as a muon, if one of the following criteria is fulfilled:

- *OD clustering*: *muon.has_cluster* == 1 identifies more than 99.9% of all muons crossing the detector [11].
- *Cluster mean time*: A cluster mean time of more than 100 ns identifies muons as well as α events.

- *Deutsch parameter*: The Deutsch parameter is a measure of eccentricity of light production in the ID. Muons traversing the detector emit a huge amount of light along their track due to scintillation and Cherenkov effect. The eccentric amount of produced light is revealed by this parameter. In this thesis, muons are identified by *Deutsch parameter* being larger than a value of 0.18. A detailed efficiency study of this parameter can be found in [11].
- “*Strange*” events: Especially muons which cross the scintillator in the IV produce a huge amount of light. The detector electronics require several 100 μs to recover from the huge light pulse. Until the electronics have stabilized, a distorted *charge* value is measured (described in sec. 4.4.1). A large deviation of the this parameter with respect to a an expected *charge* value according to the detected number of hit PMTs (*nhits* parameter) identifies these muon events. The ratio of expected *charge* to detected *charge* is set to be below 0.6 photoelectrons (pe) respectively above 1.4 *pe* in order to count an event as a muon candidate.

The efficiency of the OD clustering itself is already impressive. Along with the additional cuts of the ID, the overall efficiency is well beyond 99.99% [11]. This corresponds to less than one unidentified muon event in 2 days within the ID (muon rate: 5000 muons per day within the ID). In terms of this analysis, the efficiency of muon identification is in accordance with 100%.

5.2.3 Criterion for neutron / neutron capture γ identification

Neutrons produced by muon-induced showers are detected by the analogue neutron trigger by means of the characteristic γ of 2.2 *MeV*. It is emitted in the process of neutron capture on Hydrogen or stable Carbon isotopes, as described in sec. 4.3. These events are flagged in *Echidna* data with trigger type 128, which poses the identification criterion for the data analysis performed in this chapter.

As events detected by the neutron trigger identify neutron production, these events are classified as “neutrons” in the further course of this analysis, instead of the technically more correct term of “neutron capture γ ”. Differences between these two are pointed out in situations where it becomes necessary.

5.2.4 Criteria for radionuclide candidate identification

According to the TFC described in sec. 4.3, events qualify as radionuclide candidates by their energy deposition in the detector as well as the time difference to

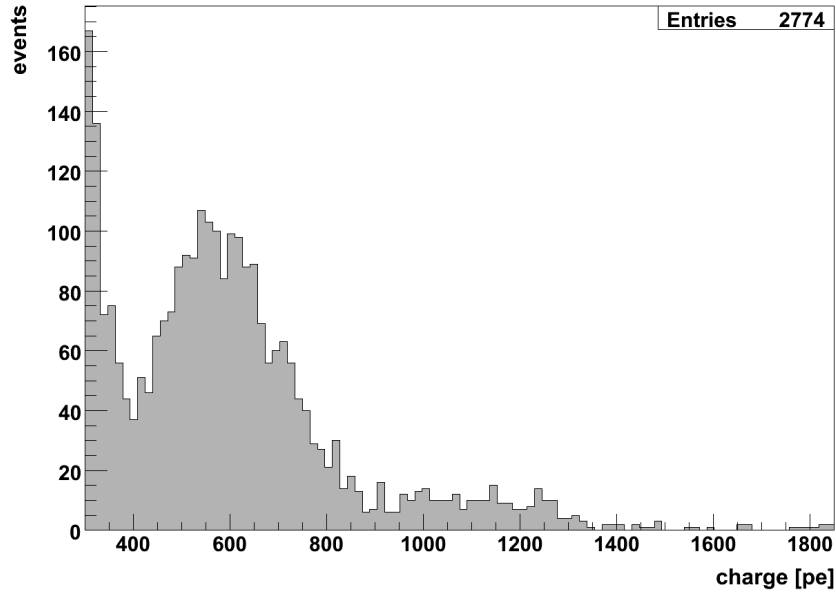


Figure 5.1: Charge spectrum of events with *trigger type* equal 1 in the *Fiducial Volume* ($R < 3.276 m$, corresponding to 100 t). The spectrum is filtered from neutron, muon and calibration events. Also ^{214}Bi - ^{214}Po coincidences are removed from data. Below a *charge* of 400 pe, the rest of the huge ^{214}Po peak as well as the 7Be - ν shoulder are present. In the *charge* range of 400 to 900 pe the prominent decay of ^{11}C is clearly visible. Between 900 and 1300 pe the contribution of external γ s from ^{208}Tl arises, covering ^{10}C in that region. Beyond 1300 8B - ν and ^{10}C decays appear.

the last muon-induced neutron event. With respect to data analysis, radionuclide candidates have to fulfill the following criteria:

- The *trigger type* of the event has to be equal 1. This means, the event has occurred only in the ID and is no artificial service trigger of Borexino. For more details on triggers, see sec. 3.3.2.
- The event is not identified as a muon (according to the muon criteria described above).
- If not otherwise stated the possible radionuclide has to be within the *Fiducial Volume* (FV) defined by the radial software cut of $R < 3.276 m$ corresponding to 100 t of fiducial mass.

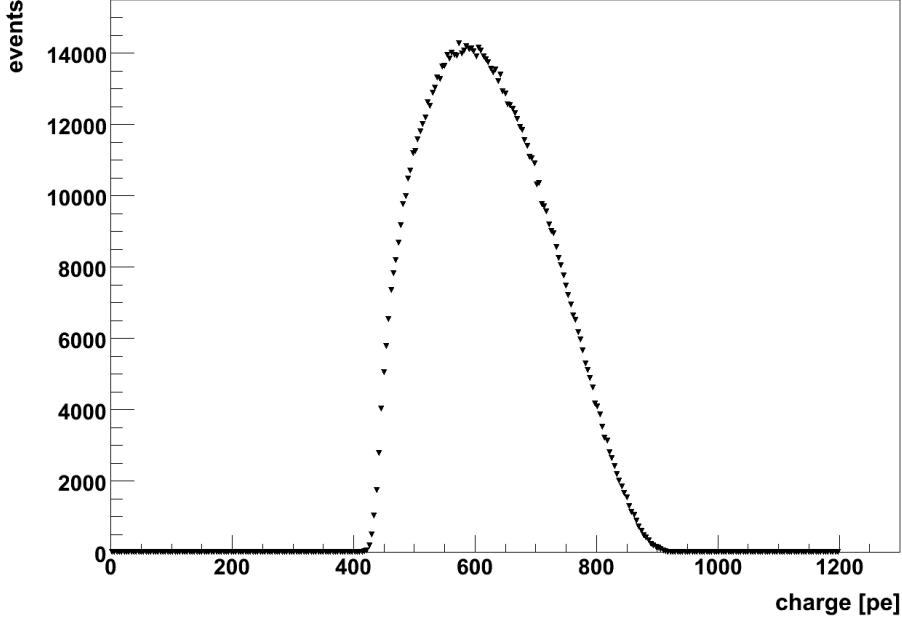


Figure 5.2: *Charge* spectrum of ^{11}C determined by spectral fits [50].

- The *charge* parameter has to be within limits according to the expected energy deposited by the radionuclide.
- The event occurs after a neutron within a time window of several mean lifetimes of the respective radionuclide.

The values of the two crucial identification criteria of a radionuclide candidate, i.e. *charge* and time difference to a previous neutron, are described for both Carbon isotopes in the following:

^{11}C decays with a mean lifetime of 29.40 m and a 0.96 MeV β^+ end-point according to the reaction:



The annihilation of the positron within the detector shifts the deposited energy of the decay by an additional energy of 1.022 MeV to an energy range of 1.022 to 1.982 MeV. As stated in sec. 3.3.2, for higher energies the correlation between deposited energy in the detector and the *charge* variable of *Echidna* deviates from linear behavior. Taking a look at the *charge* spectrum of the data for the FV (Figure 5.1), one can see the spectrum

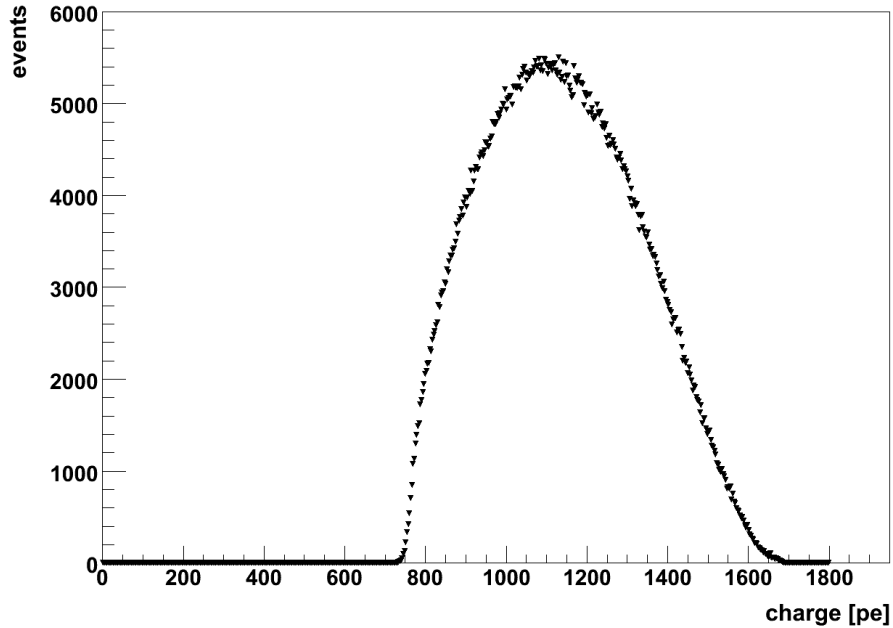


Figure 5.3: *Charge* spectrum of ^{10}C determined by spectral fits. The background of ^{208}Tl has been fitted together with ^{10}C [50].

of ^{11}C in the range of about 400 to 900 *pe*. The ^{11}C *charge* spectrum has been also extracted by means of spectral fits within the Borexino collaboration, and is shown in Figure 5.2. According to these results, the *charge* window of ^{11}C candidates has been set to 400-950 *pe*. For determination of ^{11}C mean lifetime and rate, possible ^{11}C events also have to be within a time window of 4 hours to the last muon-induced neutron event, which corresponds to about 8 times the mean lifetime of ^{11}C .

^{10}C is subject to β^+ decay with a decay time of 27.84 *s*:



The decay of ^{10}C leads to an excited state of ^{10}B and therefore to an additional emission of γ -radiation. In 98.53% (main decay channel) this radiation contributes 0.72 *MeV* to the energy deposition within the detector, whereas in 1.47% (suppressed decay channel) the radiation accounts for 1.02 *MeV*. Combined with the energy deposited in the positron annihilation, the total energy of the main decay channel spans from 1.74 *MeV* to 3.642 *MeV*. The suppressed decay channel results in a total energy deposition between

2.04 MeV and 3.942 MeV. In Figure 5.1 above a *charge* of 900 *pe* the contributions of ^{10}C and external background by ^{208}Tl get dominant. ^{208}Tl is present in the glass of ID PMTs and emits a 2.6 MeV γ -ray in the process of radioactive decay. This γ -radiation can lose energy due to scatter processes and attenuation before it reaches the IV of Borexino. Thus, the monoenergetic Thallium gamma emission is not visible as a clear peak in Figure 5.1 but as a broad distribution. Figure 5.3 shows the *charge* spectrum obtained by fitting the combined spectral contribution of ^{10}C and external background with a single β^+ -decay spectrum.

The major decay channel of ^{10}C and external background dominate the spectral fit, whereas the suppressed decay channel contributes insignificantly. Neglecting the contribution of the suppressed channel above the upper limit of the main decay channel (i.e. $E > 3.642 \text{ MeV}$), possible ^{10}C candidates are chosen within a *charge* range between 700 *pe* and 1750 *pe*. In addition, possible ^{10}C events have to be within 4 *min* ($\sim 8 \cdot \tau(^{10}\text{C})$) to a previous neutron-event. With an expected rate of about $2 \text{ counts day}^{-1} (100 \text{ t})^{-1}$ (Table 4.3), there should only be ~ 100 ^{10}C events in the data set. Due to the intersecting energy regions of [1.74,1.982] MeV between both Carbon isotopes, an additional *charge* cut is necessary to discard ^{11}C in the ^{10}C analysis, further reducing the already low number of events. Thus, an analysis on correlations by means of the TFC technique is not feasible with the given data set. Chapter 6 outlines the main features of a possible ^{10}C analysis based on more statistics.

5.3 Neutron analysis

Via interaction with the surrounding rock or the detector material itself, muons can produce electromagnetic and hadronic showers in which neutrons and radionuclides are produced. In order to reject these cosmogenic radionuclides from data, the application of the TFC technique depends on the detection of the muon-induced neutrons.

The status of neutron detection outlined in this section reflects the situation of the electronics system during the time period 07/10/07 to 10/27/07. The data, which is analyzed in this thesis, was taken in this time period. As will be pointed out in this section, the main DAQ system of Borexino was limited in its neutron detection capabilities for the given time period. Due to electronics problems, usually only one neutron of a muon-induced multiple-neutron shower was recorded by DAQ. It has to be remarked that great progress in neutron detection has been achieved recently and this problem is solved by now. For more details on recent improvements on neutron detection in Borexino, see the outlook on the cosmogenic radionuclide

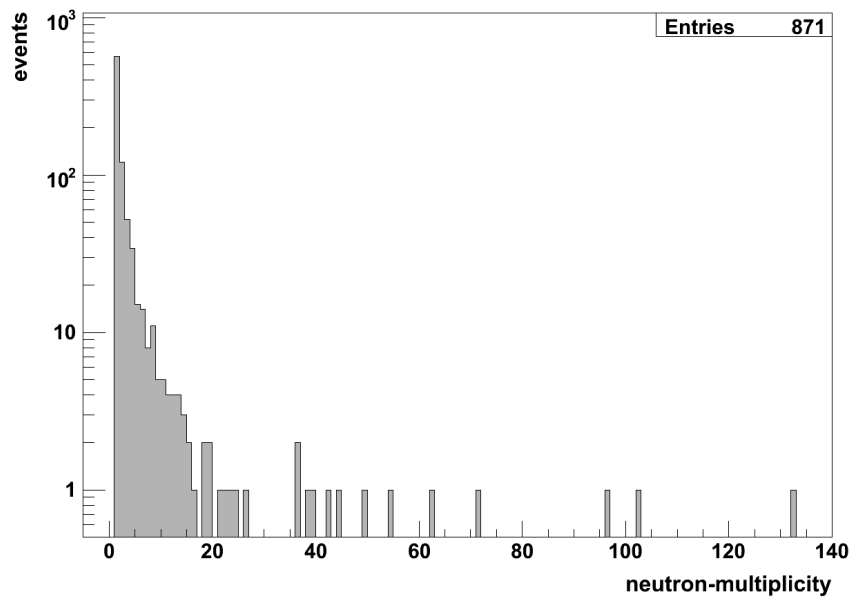


Figure 5.4: Distribution of neutron multiplicities in muon-induced showers of at least one neutron [55].

analysis in Section 7.2.

5.3.1 Neutron multiplicity

The neutron multiplicity of muon-induced showers is usually equal to one, however multi-neutron showers up to one hundred neutrons are possible. As stated in sec. 4.4.2, due to the *Three Fast Trigger Coincidence* (TFTC) veto of the main Borexino data acquisition (DAQ) system, only up to three neutrons of these showers can be detected at best. On this account, work is performed to improve the neutron detection capability of Borexino. In parallel to this analysis, multiplicities of neutron events have been studied independently by two analysis groups [54, 55].

Neutron showers within auxiliary DAQ

With the main DAQ system being subject to the TFTC veto, an auxiliary DAQ system has been connected to the detector. When the OD is triggered by a muon, a PC collects the analogue cumulative output of all PMTs of the ID. The collected data covers the time window of $10\ \mu\text{s}$ before to $490\ \mu\text{s}$ after the muon trigger.

To qualify as a neutron candidate, a detected peak has to be more than $25\ \mu\text{s}$ after the muon and produce a signal of at least $47\ \text{mV}$ corresponding to ~ 300 photoelectrons. The time threshold of $25\ \mu\text{s}$ is set to avoid the major portion of afterpulses created by the muon (for more detail on muon afterpulses see sec. 4.4.1). The result of this study on neutron multiplicity with the auxiliary DAQ is presented in Figure 5.4. About 60% of all neutron showers contain only 1 neutron, the majority of all produced neutrons is generated in neutron-showers with more than 20 neutrons.

Except the first $25\ \mu\text{s}$, the auxiliary system can detect all neutrons within a neutron shower. However, it does neither provide spatial reconstruction nor communicate with the main DAQ. Therefore, the information of the auxiliary system is not present in the *Echidna* data structure and can not be used in the application of the TFC technique. Nevertheless, this study sheds light on the reliability of the main DAQ system with respect to the TFC veto.

Neutron showers within main DAQ

The analogue neutron trigger of the main DAQ system (see sec. 4.4.2 and 3.1.2) identifies events as neutron candidates when they are within a time window of $[25, 800]\ \mu\text{s}$ after a muon event and have an energy greater than $300\ \text{keV}$. The *Three-Fast-Trigger-Coincidence* (TFTC) veto is activated, when two triggers occur less than $\sim 200\ \mu\text{s}$ apart. Within the next $\sim 2\ \text{ms}$, any additional trigger is prohibited by the TFTC veto. Therefore single-neutron showers are detected correctly by the main DAQ system, which accounts for $\sim 60\%$ of all neutron showers. All higher multiplicity neutron showers are subject to TFTC veto, with usually only one of these shower neutrons being recorded by the main DAQ system. Thus, muons followed by more than one neutron are quite rare in *Echidna* data. Nevertheless, multi-neutron showers are recorded by the main system, however with a limited maximum number of three neutrons. As a result of the time window of the analogue neutron trigger (as mentioned above), detected neutrons corresponding to the same muon can be about $775\ \mu\text{s}$ apart at most. In the data analysis performed within this thesis, showers are identified as neutron events when they are less than $2\ \text{ms}$ apart.

Shower neutrons are generated by the muon itself or by its shower particles, and are therefore produced approximately at the same time. The neutrons travel a few dozens of centimeters until they thermalize. Eventually, they are captured with a mean time of $\sim 250\ \mu\text{s}$ on Hydrogen or Carbon, emitting a characteristic γ ($E_\gamma = 2.2\ \text{MeV}$ for capture on Hydrogen). In order to determine the spatial distribution of neutrons within a shower, one can take a look at the distances between neutrons of a shower.

Figure 5.5 shows the distance distribution between consecutive shower neutrons.

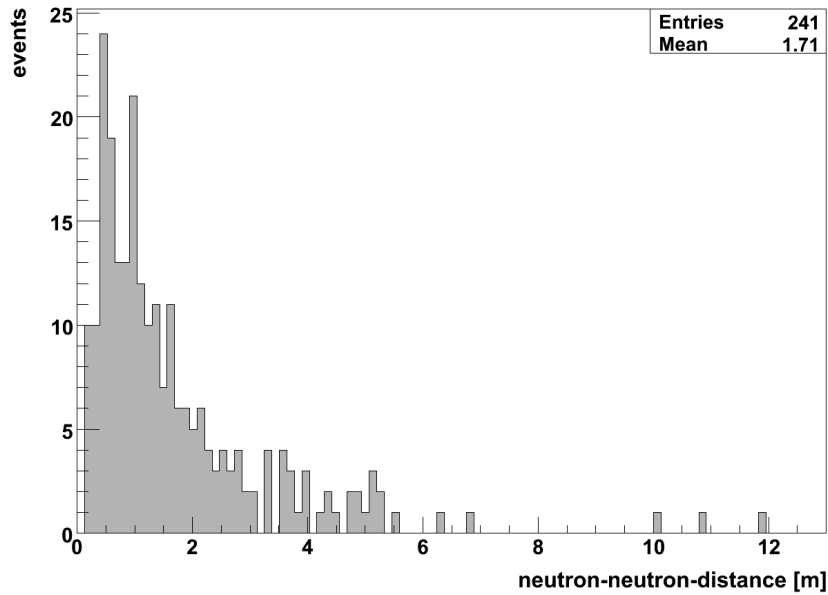


Figure 5.5: Distribution of distance of consecutive neutrons within a shower.

As one can easily see, shower neutrons are not located in the same area of the detector, but well distributed over several meters.

5.3.2 Nomenclature

According to the neutron multiplicity of muon-induced showers, different terms are used throughout this analysis. The terms used are presented in the following:

- neutron event: An event is recorded by the analogue neutron trigger as described in Section 4.4.2.
- single-neutron shower: This type of event is characterized by the detection of only one neutron event in a muon-induced shower
- multiple-neutron shower: The detection of several neutron events (i.e. more than one) accompanying a muon. Neutron showers are identified in *Echidna* as a culmination of neutron events less than 2 ms apart.
- neutron shower: The sum of single-neutron showers and multiple-neutron-showers. Thus it represents the detection of at least one neutron and therefore identifies neutron production in general.

Although the main DAQ system of Borexino is not able to detect all the neutrons for the analyzed time period, several properties of neutrons within the detector can be studied.

5.3.3 Neutron rate

In the analyzed data set, neutron showers occur at a rate of 56 showers per day. Each shower is the result of a muon-induced knock-off reaction of neutrons from a nucleus and therefore flags the production of cosmogenic radionuclides. Because the main DAQ system of Borexino usually detects only one neutron of a shower, the rate of neutron events in the ID is almost equal the rate of neutron showers. The rate of neutron events determined in the analyzed data (54 days of data taking) is 63 events per day in the ID.

5.3.4 Badly reconstructed neutrons

Badly reconstructed neutrons are the result of muon afterpulses, which reach into the neutron trigger window (sec. 4.4.1). The position and energy reconstruction of neutrons, which are affected by afterpulses, is significantly distorted. These badly reconstructed neutrons are identified in this thesis by their *cluster mean time* (parameter described in sec. 3.3.2) being larger than 100 ns . Figures 5.6 and 5.7 demonstrate the influence of muon afterpulses on the *nhits* parameter of the neutron candidates. The significant impact of muon afterpulses on the positional reconstruction of these neutrons is illustrated in the distance distribution between ^{11}C and neutrons in sec. 5.4.5.

About 16% of all neutron events feature a cluster mean time of more than 100 ns .

5.3.5 Neutron energy

As described in the Sections 4.4.1, 4.4.2, the *charge* information of all neutron events is spoiled due to the stabilization time of several $100\ \mu\text{s}$ required by the DAQ electronics. Nevertheless, the energy of neutron events can be determined by the *nhits* variable, i.e. the number of hit PMTs. This parameter is not affected by this problem. However, it can be distorted by muon afterpulses (also described in sec. 4.4.1). Taking a look at Figure 5.6, one can see the *nhits* spectrum of neutron candidates without influence of muon afterpulses (*clustermeantime* $< 100\text{ ns}$). A clear peak of the neutron capture gamma is visible at about 700 nhits corresponding to the 2.2 MeV γ from neutron capture on Hydrogen. Figure 5.7 illustrates the effect of afterpulses on the *nhits* variable. Regardless of the occurrence of muon

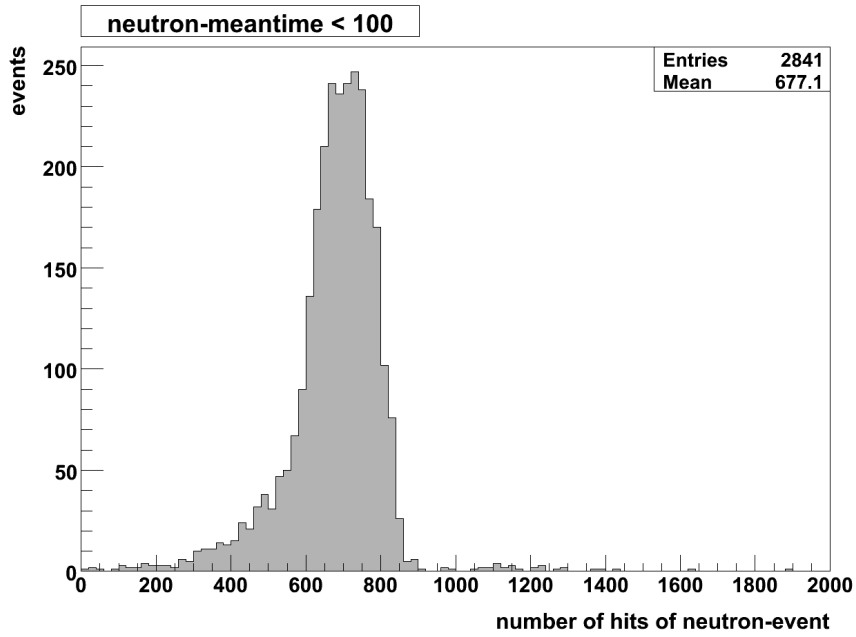


Figure 5.6: Number of hit PMT ($nhits$) of neutron candidates. The *cluster mean time* cut of 100 ns for the neutron cluster rejects badly reconstructed neutron events. A definition of the $nhits$ parameter can be found in sec. 3.3.2.

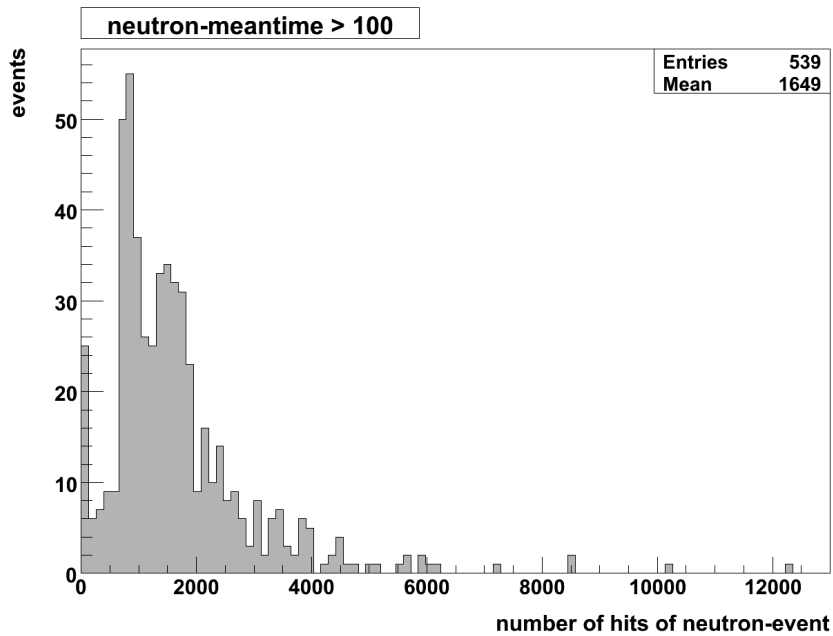


Figure 5.7: Number of hit PMT ($nhits$) of badly reconstructed neutron candidates (*cluster mean time* $> 100\text{ ns}$). As one can see, the $nhits$ parameter is distorted. A definition of the $nhits$ parameter can be found in sec. 3.3.2.

afterpulses, the *charge* parameter of all neutron events is spoiled (not shown in the plots).

5.3.6 Spatial neutron-muon correlations

First of all, the spatial correlation of events identified by the neutron trigger to the parent muon is based on the intrinsic mean free path of muon-induced neutrons in the scintillator. This expected exponential behavior is broadened by three contributions:

- Mean free path of the neutron capture γ :
The event recorded by the neutron trigger originates in fact from the γ created in the process of neutron capture. It has a mean free path of 20-30 *cm* and is reconstructed approximately in the middle of its path [15]. The emission of the γ is isotropic and therefore allows no conclusion on the exact position of the captured neutron.
- Spatial resolution of reconstructed γ :
The position reconstruction algorithm itself features an intrinsic uncertainty. The resolution of reconstructed events is ~ 10 -20 *cm* depending the deposited energy [34].
- Resolution of muon track reconstruction:
The resolution of the muon track has not been determined so far.

All these uncertainties contribute to an overall broadening of the spatial distribution. Due to this, the determination of the real mean free path of neutrons is impeded. However, for an application of the TFC technique it is sufficient to determine the effective range between detected neutron captures and the reconstructed muon track.

In Figure 5.8, the distance between the reconstructed neutron events and the track of their parent muon is plotted. On basis of the cylindrical symmetry (defined by the muon track) combined with exponential decrease due to neutron capture, the following cylindric radial distribution is expected:

$$dN(\rho) = 2\pi\rho d\rho \cdot \left(\frac{A}{\lambda_{cyl}} e^{-\frac{\rho}{\lambda_{cyl}}} + a \right) \quad (5.5)$$

ρ is the lateral distance to the muon track and λ_{cyl} the effective lateral mean free path of neutron events with respect to the muon track. A is the number of neutron captures in the data set. Due to badly reconstructed neutrons and muons, the spatial correlation between some $n - \mu$ is distorted. The parameter a accounts

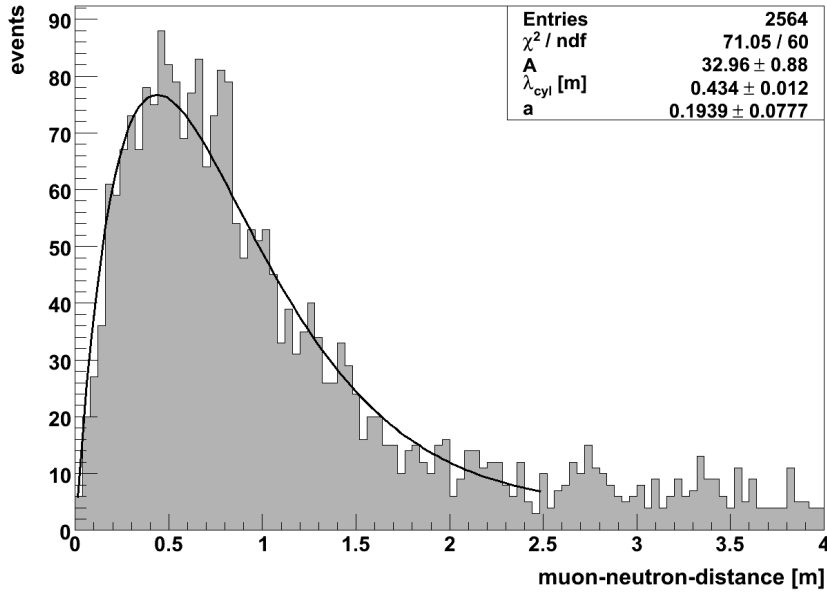


Figure 5.8: Lateral distance of neutron events to reconstructed muon track. The cylindrical symmetry around the muon track causes the step linear increase of the event numbers at small distances. The distribution is fitted by eq. (5.5). The fitted effective mean free path is a result of the real mean free path of neutrons and of uncertainties due to neutron capture γ mean free path, as well as position and muon track reconstruction.

for these pairs of lost correlation, and also uncorrelated random coincidences within the neutron trigger window. Function (5.5) is fitted to the distribution as shown in Figure 5.8. The fit function (5.5) considers only an exponential lateral behavior of the neutrons and uncorrelated background. Thus, it neglects the additional broadening mentioned above. However, for analysis on correlations of muon and neutron events in the data, an effective lateral mean free path is sufficient. The fit describes well the lateral distribution of the fitted area and results in an effective cylindrical mean free path of $\lambda_{\text{cyl}} = 0.434 \pm 0.012 \text{ m}$.

The analysis on the neutron capture time in the next section will point out, that accidental coincidences in the neutron time gate are negligible. This means that the background contribution in Figure 5.8 arises due to $n - \mu$ pairs with disturbed spatial correlation. This is the case, when either neutron or muon track are badly reconstructed. Analysis on ^{11}C -neutron (Sec. 5.4.6) and ^{11}C -muon (Sec. 5.4.8) addresses this fact.

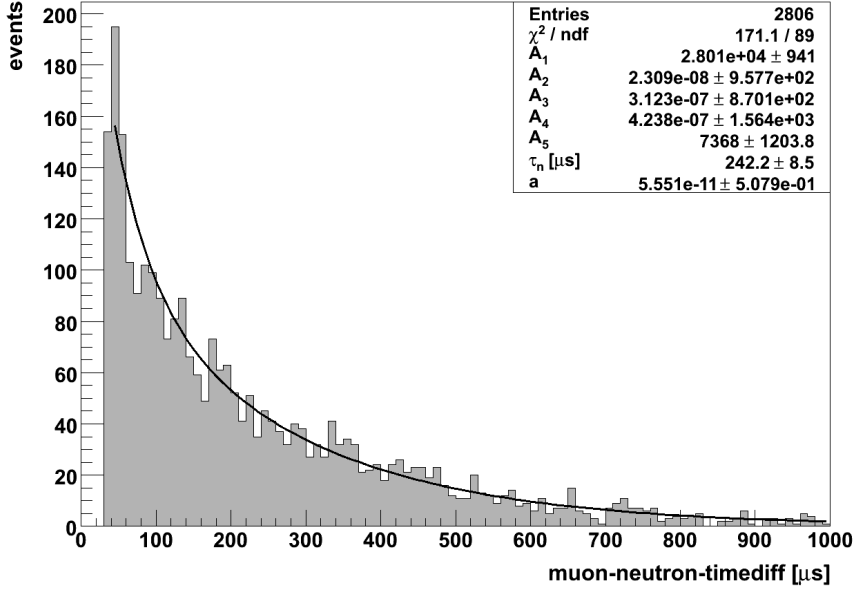


Figure 5.9: Time distribution of neutron events relative to their parent muon fitted with multiple exponentials. The $25 \mu\text{s}$ time threshold of the neutron trigger avoids the misidentification of muon afterpulses as neutron candidates. For more detail on this topic, see Sections 4.4.1 and 4.4.2.

5.3.7 Neutron capture mean time

The study of correlations between muons and their induced neutrons also yields information about the neutron capture mean time τ_n . Neutrons are produced at the moment the muon passes the detector and their capture is detected by the analogue neutron trigger. Figure 5.9 displays the time distribution of these coincidences. Also shown is a multiple exponential fit of the time distribution, based on the consideration, that due to the TFTC veto usually only the first neutron of a multiple-neutron shower is detected (sec. 5.3.1). Therefore, the probability that at least one neutron of a shower with neutron-multiplicity M is captured in a time window of $[0, t]$ after a muon event is:

$$P_M(t) = 1 - \prod_1^M e^{-\frac{t}{\tau}} = 1 - e^{-M\frac{t}{\tau}} \quad (5.6)$$

Thus, the differential probability of at least one neutron capture within a time interval dt is:

$$dP_M(t) = \frac{M}{\tau} e^{-M \frac{t}{\tau}} dt \quad (5.7)$$

Taking into account the probability that a neutron shower of multiplicity M is generated with a certain probability $W(M)$, one can describe the time spectrum in general:

$$dP(t) = \sum_M W(M) dP_M(t) \stackrel{(5.7)}{=} \sum_M W(M) \frac{M}{\tau} e^{-M \frac{t}{\tau}} dt \quad (5.8)$$

For a data set with a number of A neutron showers and a background contribution of a , the time profile is described by:

$$dN(t) = A dP(t) + a dt \stackrel{(5.8)}{=} \sum_M A_M \frac{M}{\tau} e^{-M \frac{t}{\tau}} dt + a dt \quad (5.9)$$

$$A_M := A \cdot W(M) \quad (5.10)$$

The Function (5.9) is fitted to the time profile in Figure 5.9 with exponentials up to a neutron multiplicity M of 5. The contribution of the one-neutron exponential to the distribution is high, whereas the contribution of multi-neutron exponentials is quite low, except for the 5-neutron exponential. Due to its steep inclination, this exponential is weighted the most by the fitting algorithm as it describes the deviation to the 1-neutron exponential in the low time region. This increase is not a result of 5-neutron showers, but also of the sum of all multiple-neutron showers with $M > 5$ which have been neglected by the fit function. However, this fit demonstrates that the contribution of multiple-neutron showers to the later part of neutron capture time distribution is negligible. Also the minor amount of background in the time distribution proves that all events detected by the neutron trigger can be considered as neutron capture processes.

Fitting only the late part of the time distribution, and thereby rejecting the contribution of multiple neutron showers, the mean neutron capture time τ_n can be determined with much less systematic uncertainties. In Figure 5.10 the time profile is fitted by a single exponential in the time region greater than $250 \mu s$. Not shown in the plot, the contribution of a 2-neutron exponential as well as a constant background distribution have been considered and shown to be as negligible (order of 10^{-7} respectively 10^{-8}). The fit results in a neutron capture mean time of $232 \pm 10 \mu s$. This result is in reasonable agreement with former experimental determinations of τ_n in scintillator material, performed within the CTF ($\tau_n = 214 \pm 11 \mu s$ [33], respectively $\tau_n = 257 \pm 27 \mu s$ [32]) as well as in FLUKA simulations [51, 32] ($\tau_n = 254 \pm 1 \mu s$).

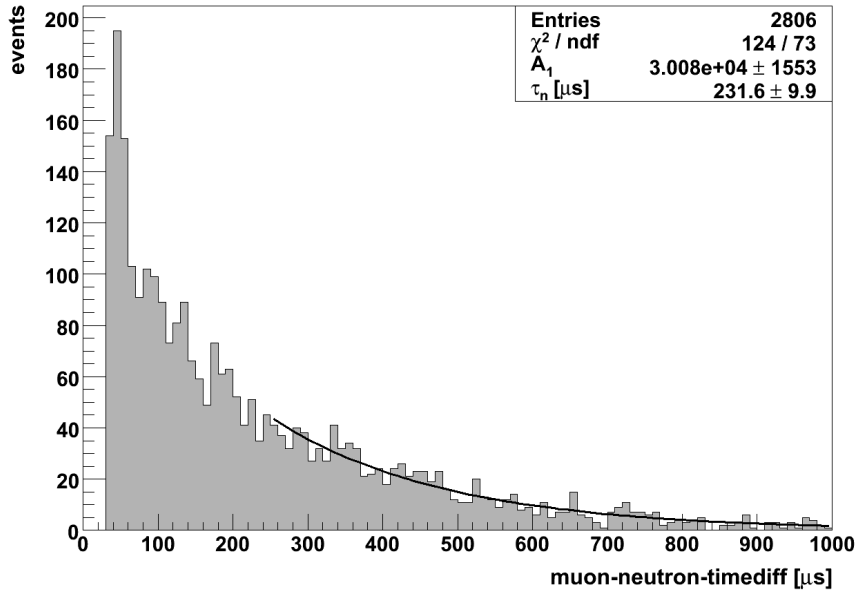


Figure 5.10: Time distribution of neutron events relative to their parent muon fitted with a single exponential.

5.4 ^{11}C analysis

As described in section 4.3, the short-lived cosmogenic radionuclides with a mean live time less than about one second can be easily rejected from data by a general veto for $\sim 2\text{ s}$ of the detector after each muon. However, ^{11}C and ^{10}C have mean lifetimes of 29.40 m and 27.84 s and can not be discarded this easily. A general veto of 1 h would be necessary to discard both radionuclides. With a rate of ~ 5000 muons per day in the ID, the detector would be permanently vetoed.

The goal of TFC technique is the tagging of these cosmogenic radionuclides. Especially ^{11}C is of interests, which is the main obstacle in detection of $p\bar{p}$ - and $\text{CNO-}\nu$. To determine the reliability of the TFC technique within Borexino, its tagging strategy can also be used to search actively for ^{11}C in the data. Consequently, a ^{11}C rate can be determined and compared with rates determined by spectral fits of ^{11}C . This section presents the results of the study on ^{11}C as well as the applicability of the TFC with respect to ^{11}C -neutron and ^{11}C -muon correlations.

	reaction	weight
with n	$^{12}\text{C}(\gamma, n)^{11}\text{C}$	59.4%
	$^{12}\text{C}(n, 2n)^{11}\text{C}$	13.4%
	$^{12}\text{C}(p, p+n)^{11}\text{C}$	9.2%
	$^{12}\text{C}(\pi^-, \pi^- + n)^{11}\text{C}$	6.8%
	$^{12}\text{C}(\mu, \mu + n)^{11}\text{C}$	4.0%
	$^{12}\text{C}(\pi^+, \pi^+ + n)^{11}\text{C}$	1.8%
	$^{12}\text{C}(e, e + n)^{11}\text{C}$	0.7%
invisible	$^{12}\text{C}(p, d)^{11}\text{C}$	1.0%
	$^{12}\text{C}(\pi^+, \pi^0 + p)^{11}\text{C}$	3.5%

Table 5.1: ^{11}C production channels in muon-induced particle showers as computed by FLUKA simulations [49, 33].

5.4.1 ^{11}C production channels

The muon beam experiment performed at CERN on cosmogenic radionuclides [47] (described in sec. 4.2.1) demonstrated that, in Borexino, ^{11}C background would exceed the signal from pep and CNO neutrinos (according to the SSM) by an order of magnitude. Therefore, simulations on ^{11}C production in muon-induced showers were performed by the Borexino collaboration in order to determine the reliability of the TFC technique that was originally suggested by M. Deutsch [52]. The simulation used the particle transport code FLUKA [51] to calculate the production rates of the prominent particles induced by muons within the CTF setup, i.e. neutrons, protons, γ -rays, electrons, π mesons as well as ^{11}C induced by these secondaries or the muon itself. The resulting weights of each production channel are presented in table 5.1.

The study demonstrated that muon-induced showers are dominated by γ rays and electrons. Due to a giant dipole resonance of ^{12}C at 25 MeV, the cross section for γ rays becomes dominant. In consequence, the main production channel for ^{11}C production is the (γ, n) exchange reaction which accounts for 59.4% of the total production rate. Spallation by electrons is much less effective, as their cross section is lower by a factor of the fine structure constant α . Other channels with at least 1 neutron in the final state account for additional 35.1% of the total production rate.

There are 2 production channels without a final neutron, i.e. the $^{12}\text{C}(p, d)^{11}\text{C}$ and $^{12}\text{C}(\pi^+, \pi^0 + p)^{11}\text{C}$ reactions. Due to the absence of neutrons, both reactions cannot be tagged by the TFC technique and are therefore referred as “invisible” channels. These invisible channels cause an intrinsic inefficiency of ^{11}C tagging via the TFC. However, they only account for 4.5% of the total ^{11}C production rate.

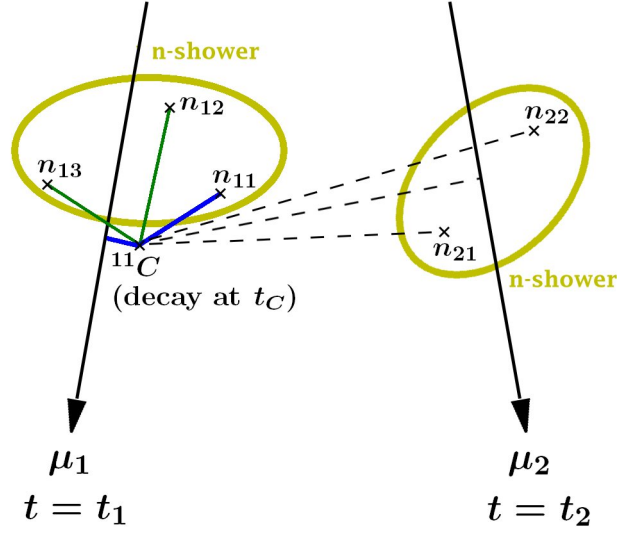


Figure 5.11: Schematics of muon, neutron and ^{11}C correlations. The ^{11}C is produced at time t_1 and is correlated in time and space (blue line) with its knock-off neutron (n_{11}) and its parent muon (μ_1). Because all neutrons induced by μ_1 are detected approximately at the same, the ^{11}C event is also correlated to all shower neutrons in time (illustrated by the green line). The muon μ_2 and its induced neutrons occur at time t_2 and are completely uncorrelated to the ^{11}C event (dashed lines).

5.4.2 Correlations in the data analysis

Muons and their secondaries can produce ^{11}C by removing one neutron from a ^{12}C nucleus. Any produced ^{11}C nucleus corresponds to one neutron and one muon. For analysis on time correlations between ^{11}C (selection criteria stated in sec. 5.2.4) and neutron events, usually a time gate of 4 hours after each neutron event is opened ($\tau_{^{11}\text{C}} = 29.40\text{ m}$). Neutron-inducing muons occur in the ID at a rate of ~ 60 per day (stated in sec 5.3.3). This corresponds to one such muon every $\sim 24\text{ min}$ in average. Thus, a ^{11}C decay can not be unambiguously allocated to its parent muon and its knock-off neutron. Nevertheless, an analysis on correlations in time and space between ^{11}C and neutrons/muons is possible. This shall be illustrated in the following.

Correlated and uncorrelated event-pairs

Because ^{11}C can not be definitely allocated to its knock-off neutron, one has to consider every pair of neutrons and ^{11}C decays, which is less than a few ^{11}C decay

times apart. In this analysis the time gate is usually chosen to 4 hours.

Due to overlap of these time gates, ^{11}C candidates can be counted several times by different neutron events. However, only correlated pairs of neutron and ^{11}C will contribute to the characteristic exponential distribution in the time profile. This is based on the fact, that the capture of the knock-off neutron ($\tau \sim 250\mu\text{s}$) is approximately coincident with the ^{11}C production, compared to the ^{11}C mean lifetime of 29.40 m . Thus, the profile of the time difference between the detection of the knock-off neutron and the decay of its corresponding ^{11}C follows an exponential profile, which is typical for radioactive decays. All neutrons, which are not correlated with the specific ^{11}C result in an uncorrelated flat background.

Figure 5.11 illustrates the correlation between ^{11}C , neutrons and muons. A muon μ_1 crosses the detector at time t_1 and produces ^{11}C by rejecting a neutron (n_{11}). Also, additional neutrons of the muon-induced shower are present (n_{12} and n_{13}). The whole neutron shower of μ_1 is marked by a yellow circle in the Figure.

All shower neutrons are produced at the same time by μ_1 and decay independently with a neutron mean capture time of $\sim 250\mu\text{s}$. However, on a time scale of the ^{11}C mean lifetime ($\tau_{^{11}\text{C}} = 29.40\text{ m}$), all neutrons of the same shower are captured at the same time. Thus, the ^{11}C produced by μ_1 is correlated with all shower neutrons of this muon in time (green line). However, the ^{11}C is only correlated to its knock-off neutron n_{11} both in time and space (illustrated by the blue line). The ^{11}C is also correlated in time and space with the muon μ_1 .

Also shown is another muon μ_2 which crosses the detector at time t_2 . Time t_2 shall be less than 4 h before the ^{11}C decay at time t_C (in this example, μ_2 produces neutrons without any ^{11}C). Because the ^{11}C decay is within the 4 h time gate to the neutrons of μ_2 (n_{21} and n_{22}), the time correlation to these two neutrons is also recorded in the data analysis. By reason that the ^{11}C is completely uncorrelated with the neutrons of μ_2 (shown as the dashed line), these neutron- ^{11}C pairs result as uncorrelated background in temporal and spatial distributions between ^{11}C and neutron events. Also the ^{11}C is completely uncorrelated with μ_2 .

Temporal correlations and shower-correction:

An exponential decay of ^{11}C is expected in the relative time distribution between muon-induced neutron events and ^{11}C candidates. This exponential comprises information on ^{11}C mean lifetime as well as on the number of ^{11}C decays. According to this number, a rate of ^{11}C production can be determined.

As stated above, ^{11}C produced in a multiple-neutron shower is correlated in time with all neutrons of the same shower. The single ^{11}C decay would be counted multiple times as a correlated event. One can correct this fact, by only considering one neutron of the whole shower for analysis on temporal correlations. The so-called “shower-correction” applied in this thesis considers only the last neutron

event in time of a detected multiple-neutron shower.

Because there is only one muon per ^{11}C production, the shower correction is not necessary for analysis on muon- ^{11}C correlations (performed in sec 5.4.8).

Spatial correlations:

As shown in Figure 5.11 and described above, ^{11}C is only directly correlated in space with its knock-off neutron and parent muon. Thus, for analysis on spatial correlations all neutron- ^{11}C pairs can be considered.

5.4.3 Influence of DAQ deadtime

The time gate after a neutron for ^{11}C search is chosen to 4 h . Compared to the average run duration in the analyzed data set of about 6 h , the interruption of open time gates due to deadtime between two runs is very likely. The goal of the Borexino collaboration is to minimize the deadtime between runs, however especially in this early stage of data taking, hardware inspections as well as rejections of runs due to electronic problems can produce long deadtime between runs. Deadtimes during an open time gate distort the time profile.

For a determination of ^{11}C properties by means of the time profile, it is critical to avoid these distortions. For this reason, time gates for ^{11}C search are stopped at the end of a run. However, this procedure introduces its own artificial effect to the time profile, i.e. a linear decrease in time distribution of signal as well as the background. But in contrast to distortions caused by deadtime, the linear decrease due to finite run duration can be modeled and well fitted to the data, as described in the next section.

5.4.4 Model of the time profile

The effect of limited run duration on the distribution of time between neutron events and ^{11}C candidates is outlined in this section. First of all the model is based on a run of duration t_{run} , containing neutron and ^{11}C events with rates $R_n(t)$ respectively $R_{^{11}\text{C}}(t)$. After each neutron event an independent time gate of length t_{gate} is opened and time differences t_{diff} to following ^{11}C events are recorded. Therefore, a ^{11}C event can be recorded by several neutrons. An active time gate is prematurely closed when the run ends. The differential number of recorded $n - ^{11}\text{C}$ pairs, consisting of neutrons in the time interval $[t, t + dt]$ and ^{11}C events within $[t + t_{diff}, t + t_{diff} + dt_{diff}]$, is

$$dN(t, t_{diff}) = R_n(t) dt \cdot R_{^{11}\text{C}}(t + t_{diff}) dt_{diff} \quad (5.11)$$

$$t \in [0, t_{run}] \quad t_{diff} \in [0, t_{gate}] \cap [0, t_{run}] \quad (5.12)$$

The intersection condition of t_{diff} expresses the fact that the maximum time difference between a neutron and a ^{11}C event is limited both by the time gate length t_{gate} as well as the run duration t_{run} . E.g., when the run duration is shorter than the chosen time gate, t_{diff} can be maximal t_{run} . Runs with $t_{run} < t_{gate}$ will be referred to as “short runs”, whereas “long runs” correspond to $t_{run} \geq t_{gate}$.

Model of neutron and ^{11}C rates

As the neutrons are (as their parent muons) distributed randomly in time, the neutron rate is constant:

$$R_n(t) = R_n \quad (5.13)$$

The ^{11}C rate in the time gates is determined by two contributions: a correlated and an uncorrelated $n - ^{11}\text{C}$ distribution.

$$R_{^{11}\text{C}}(t + t_{diff}) = R_{^{11}\text{C};corr}(t + t_{diff}) + R_{^{11}\text{C};uncorr}(t + t_{diff}) \quad (5.14)$$

Precondition of the time model:

As mentioned in sec. 5.4.2, ^{11}C is correlated in time with all neutrons of the shower, in which it was produced. Each temporal correlation contributes to an exponential decay in the time profile governed by the ^{11}C decay time. Thus, ^{11}C contributes for every detected shower neutron to the time profile. To determine a rate on basis of the time profile, it is essential, that ^{11}C decays are not counted as correlated events multiple times. The model to describe the time profile of t_{diff} is based on the precondition, that a ^{11}C event is only correlated in time with a single neutron. In the actual data analysis performed in this thesis, this condition is achieved by the application of the shower-correction, which is also described in sec. 5.4.2.

With this precondition, each produced ^{11}C is only correlated in time with a single neutron and contributes to the correlated time distribution only once. The uncorrelated pairs of neutron and ^{11}C just increase the flat background of the time profile. Therefore, the correlated and uncorrelated distributions of $R_{^{11}\text{C}}(t + t_{diff})$ in eq. (5.14) can be described as follows:

Correlated contribution:

$$R_{^{11}\text{C};\text{corr}}(t + t_{\text{diff}}) = \frac{K}{\tau} e^{-\frac{t_{\text{diff}}}{\tau}} \quad (5.15)$$

K is the mean number of correlated ^{11}C recorded in the time gates.

Uncorrelated contribution:

$$R_{^{11}\text{C};\text{uncorr}}(t + t_{\text{diff}}) = R_{^{11}\text{C};\text{uncorr}} \quad (5.16)$$

As mentioned above, the rate of uncorrelated $n - ^{11}\text{C}$ pairs is time independent.

The combination of the correlated and uncorrelated contribution can be written as

$$\begin{aligned} R_{^{11}\text{C}}(t + t_{\text{diff}}) &= R_{^{11}\text{C};\text{corr}}(t + t_{\text{diff}}) + R_{^{11}\text{C};\text{uncorr}}(t + t_{\text{diff}}) \stackrel{(5.14)(5.15)(5.16)}{=} \\ &= \frac{K}{\tau} e^{-\frac{t_{\text{diff}}}{\tau}} + R_{^{11}\text{C};\text{uncorr}} := \widehat{R}_{^{11}\text{C}}(t_{\text{diff}}) \end{aligned} \quad (5.17)$$

$\widehat{R}_{^{11}\text{C}}(t_{\text{diff}})$ is independent of time t and describes the common time profile of a radioactive decay, consisting of an exponential decay with uncorrelated flat background. Considering the end of run, the total distribution of recorded events behaves as

$$\widehat{R}_{^{11}\text{C}}(t_{\text{diff}}) = \begin{cases} \widehat{R}_{^{11}\text{C}}(t_{\text{diff}}) & \text{if } t \leq t_{\text{run}} - t_{\text{diff}} \\ 0 & \text{else} \end{cases} \quad (5.18)$$

Integration of equation (5.11) in time t with an integration range according to (5.12) and the definition of rates according to Formulas (5.13) and (5.17) gives

$$\begin{aligned} dN(t_{\text{diff}}) &= R_n \widehat{R}_{^{11}\text{C}}(t_{\text{diff}}) \cdot (t_{\text{run}} - t_{\text{diff}}) dt_{\text{diff}} \\ t_{\text{diff}} &\in [0; t_{\text{gate}}] \cap [0; t_{\text{run}}] \end{aligned} \quad (5.19)$$

This equation can be rewritten as:

$$\begin{aligned} dN(t_{\text{diff}}) &\stackrel{(5.17)}{=} \left(\frac{A_s}{\tau} e^{-\frac{t_{\text{diff}}}{\tau}} + a_s \right) \left(1 - \frac{1}{t_{\text{run}}} t_{\text{diff}} \right) \\ t_{\text{diff}} &\in [0; t_{\text{gate}}] \cap [0; t_{\text{run}}] \end{aligned} \quad (5.20)$$

$$A_s := R_n \cdot K \cdot t_{\text{run}}$$

Total number of correlated ^{11}C events in the single run.

$$a_s := R_n \cdot R_{^{11}\text{C};\text{uncorr}} \cdot t_{\text{run}}$$

Total rate of uncorrelated background in the single run.

As one can see in Formula (5.20), the usual distribution of a radioactive decay with flat background is now convoluted with an artificial linear decrease due to the limited run duration, i.e. $(1 - \frac{1}{t_{run}}t_{diff})$. This effect shall be illustrated in more detail. Schematic plots of the The following time profiles are based on a time gate of 4 h, which is also used in the actual ^{11}C analysis in this chapter.

Figure 5.12 shows a typical artificial deformation of the time profile of a long run ($t_{gate} < t_{run}$). In Figure 5.13 the deformed time profiles for runs of different duration t_{run} are shown. The black lined time profiles are the distributions described by eq. (5.19). The purple lined time profiles consider only the uncorrelated background distributions $dN_{uncorr}(t_{diff})$. On basis of Formulas (5.17) and (5.19), the distribution of uncorrelated background is

$$\begin{aligned} dN_{uncorr}(t_{diff}) &= R_n \widehat{R}^{11\text{C};uncorr} \cdot (t_{run} - t_{diff}) dt_{diff} \\ t_{diff} &\in [0; t_{gate}] \cap [0; t_{run}] \end{aligned} \quad (5.21)$$

As one can see, in the shortest run ($t_{run} = 2h$) the neutron and ^{11}C time difference is limited by the run duration. No time difference for more than 2 h is can be detected in this short run. Therefore, the linear decrease is broken by the run end at 2 h.

Multiple runs

Equation (5.19) and (5.20) describe the time profile of a single run. However, the data set prepared for analysis consists of up to about 140 runs. Every run of this ensemble contributes with its own time profile according to the stated equations. Therefore, the total time profile in t_{diff} is the sum of all these individual time profiles. With respect to the model, two factors have to be considered:

Short and long runs:

As mentioned before, one has to distinguish runs on the basis whether their duration is longer ($t_{gate} \leq t_{run}$: long runs) or shorter ($t_{gate} > t_{run}$: short runs) than the chosen time gate of analysis. Figure 5.13 shows the different behavior of long and short runs. It illustrates the time profile of the sum of correlated and uncorrelated distributions (according to eq. (5.19), as well as the time considering only the uncorrelated distribution (according to eq. (5.21).

For better illustration, the concept of summed time profiles shall be explained for uncorrelated background, shown in the Figure as purple time profiles. The following considerations can be applied completely analog on correlated contributions. It is obvious, that the background profiles of long runs can be summed up in a

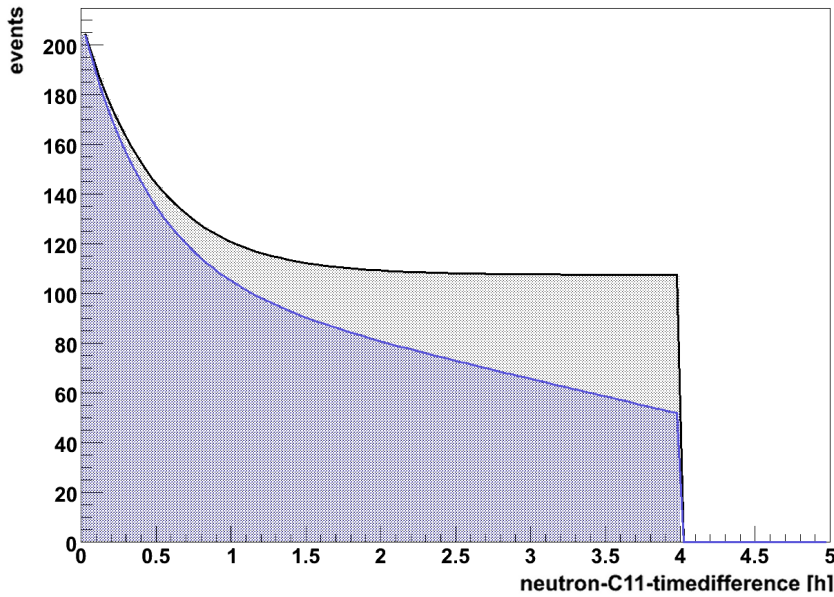


Figure 5.12: Model of ^{11}C time profile before (black) and after artificial deformation (blue) according to Formulas (5.20), respectively (5.19).

linear way. Thus, the *Summed Background Time Profiles* (SBTF) of long runs can be described by a single linear function. As shown in Figure 5.13, the background profile of a short run is interrupted by the run end. Because the event number can not be negative, linear behavior is broken. Therefore, the sum of short runs can not be described by a single linear function.

This fact is illustrated in Figure 5.14. As expected, the SBTF of long runs results in a total linear function. In contrast, the SBTF of short runs can be misinterpreted as a decay effect.

This consideration is completely analog for the correlated distributions. On basis of this study, only long runs are used for analysis on time profiles, unless otherwise stated.

Stability of rates:

With the restriction onto long runs, the total time profile of sum of N runs can be written according to 5.19 as:

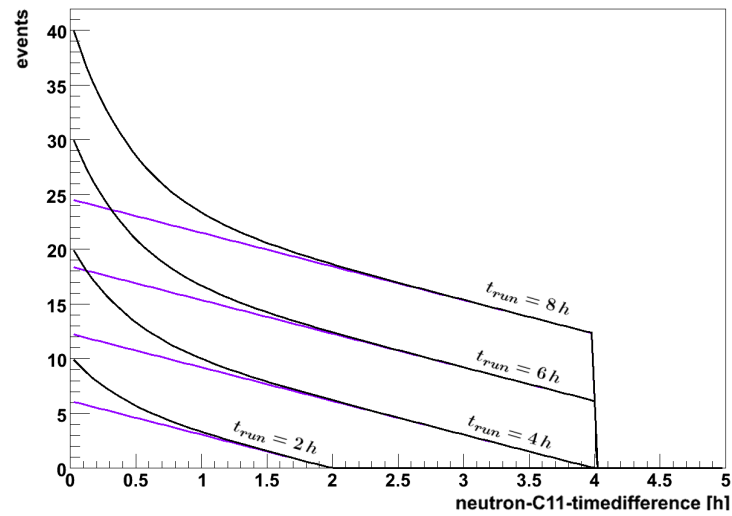


Figure 5.13: Deformed time profiles for different run durations. The black time profiles are the sum of correlated and uncorrelated distributions artificially deformed by the finite run duration (according to eq. (5.19)). The purple time profiles represent only the deformed uncorrelated distributions (according to eq. (5.21)).

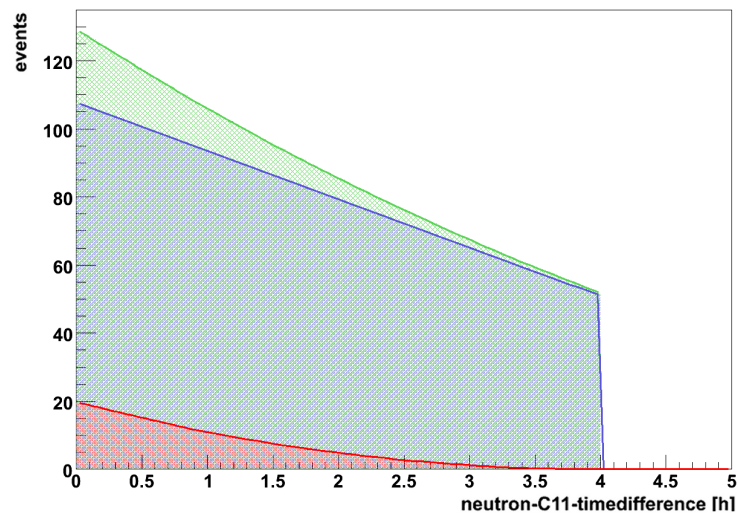


Figure 5.14: Summed time profiles of the deformed uncorrelated background distributions for short runs (shaded red), long runs (blue shaded) and all runs (shaded green).

$$dN_{total}(t_{diff}) = \sum_i^N R_{n;i} \widehat{R}_{11C;i}(t_{diff}) \cdot (t_{run;i} - t_{diff}) dt_{diff} \quad t_{diff} \in [0; t_{gate}] \quad (5.22)$$

Parameter i refers to different runs in the ensemble. The run duration $t_{run;i}$ is naturally dependant on the specific runs. One would expect the rates $R_{n;i}$ and $\widehat{R}_{11C;i}(t_{diff})$ to be equal for all analyzed runs. However, electronics and software problems can cause fluctuations in the detected rates. To accommodate for this, $R_{n;i}$ and $\widehat{R}_{11C;i}(t_{diff})$ are treated as run dependent variables in this analysis. Therefore, using eq. (5.17), the Formula (5.22) can be expressed as

$$\begin{aligned} dN_{total}(t_{diff}) &= \frac{A}{\tau} e^{-\frac{t_{diff}}{\tau}} \left(1 - \frac{B}{A} t_{diff}\right) + a \left(1 - \frac{b}{a} t_{diff}\right) \\ &= \frac{A}{\tau} e^{-\frac{t_{diff}}{\tau}} (1 - C \cdot t_{diff}) + a(1 - c \cdot t_{diff}) \end{aligned} \quad (5.23)$$

$A := \sum R_{n;i} K_i t_{run;i} \stackrel{(5.24)}{=} \sum R_{11C;i} t_{run;i}$	Total number of correlated ^{11}C events.
$B := \sum R_{n;i} K_i \stackrel{(5.24)}{=} \sum R_{11C;i}$	Sum of run-specific correlated ^{11}C event rates.
$a := R_{11C;uncorr} \sum R_{n;i} t_{run;i}$	Total rate of uncorrelated background.
$b := R_{11C;uncorr} \sum R_{n;i}$	Sum of run-specific uncorrelated ^{11}C event rates.
$C := \frac{B}{A}$	Decrease factor of correlated ^{11}C events
$c := \frac{b}{a}$	Decrease factor of uncorrelated background events
τ	mean lifetime of ^{11}C .

In the definition of the parameters A and B , the following equation has been used:

$$R_{11C;i} = R_{n;i} \cdot K_i \quad (5.24)$$

A fluctuation of the neutron rate $R_{n;i}$ automatically results in a fluctuation of the mean number of correlated ^{11}C detected per neutron time gate, which is denoted as K_i (see eq. 5.15). The product of both results in the total rate of detected ^{11}C of the whole run i , denoted as $R_{11C;i}$ (eq. 5.24).

Uncorrelated background within a neutron time gate ($R_{^{11}\text{C};uncorr}$) is according to its nature independent from the detected neutron rate, and therefore independent of specific runs.

As one can see in Formula (5.23), at first glance the correlated and uncorrelated distribution seem to have different artificial decrease factors C and c , respectively. In fact, this is not the case and illustrated in the following:

Parameter A can be expressed by a mean value of the product of $R_{n;i}$ and $t_{run;i}$.

$$A = N \cdot \langle R_{^{11}\text{C};i} t_{run;i} \rangle \quad (5.25)$$

N is the number of analyzed runs, while i represents different runs of this ensemble. Because the run-specific ^{11}C rate ($R_{^{11}\text{C};i}$) and the duration of a given run ($t_{run;i}$) are uncorrelated values, one can express A by the mean values of each single factor:

$$A = N \cdot \langle R_{^{11}\text{C};i} \rangle \langle t_{run;i} \rangle \quad (5.26)$$

According to this, parameter B can be expressed in the same way:

$$B = N \cdot \langle R_{^{11}\text{C};i} \rangle \quad (5.27)$$

Repeating this procedure also for a and b , one can show that

$$C = c = (\langle t_{run;i} \rangle)^{-1} \quad (5.28)$$

On the basis of this result, Formula (5.23) simplifies to

$$dN_{total}(t_{diff}) = \left(\frac{A}{\tau} e^{-\frac{t_{diff}}{\tau}} + a \right) (1 - C \cdot t_{diff}) \quad (5.29)$$

The restriction on long runs (i.e. runs of a duration more than the time gate of 4 h), the total time profile of these runs can be expressed by a single function. The summed time profile of long runs is identical in shape to the time profile of a single run (compare to eq. (5.20). Thus, Figure 5.12 also illustrates the summed time profile of long runs for the deformed and non-deformed case.

Formula (5.29) is used for all time profile fits in the analysis on ^{11}C . Parameter A is the total amount of ^{11}C in the analyzed time profile, while a is caused by uncorrelated background. Parameter C is treated as a free parameter in all fits.

This model is only based on the fact, that ^{11}C is correlated with one single previous neutron in data of a run of finite duration of at least 4 h (long runs).

This model can also be applied on analysis of correlations between muons and ^{11}C . In this case, ^{11}C is only correlated with its parent muon, and thus fulfills the requirement of this model.

5.4.5 ^{11}C -neutron correlations

After a neutron event is identified by the analogue neutron trigger, events within a 4 h time gate qualify as ^{11}C candidates by a *charge* value of 400 to 950 *pe*, according to sec. 5.2.4. The analysis on correlations between the detected neutron events and these ^{11}C candidates is presented in the following.

Spatial ^{11}C -neutron correlations

The distribution of the distance between neutrons and ^{11}C events is expected to follow an exponential decrease convoluted with a volumetrical increase according to the spherical symmetry around the reconstructed neutron position.

$$dN(r) = 4\pi r^2 dr \cdot \left(\frac{A}{\lambda} e^{-\frac{r}{\lambda}} + a \right) \quad (5.30)$$

The definition of variables follows the same style as already used in sec. 5.3.6 for the determination of the effective lateral neutron mean free path to the parent muon track:

r is the distance between reconstructed positions of neutron and ^{11}C events. λ is the effective mean free path of neutron events. A is the actual number of ^{11}C decays, while a accounts for uncorrelated random coincidences within the time gate for ^{11}C search.

Four different plots are shown, illustrating the effect of the two major influences on the distance distribution: the n - ^{11}C time difference, as well as the influence of muon afterpulses on the quality of neutron position reconstruction.

- $n - ^{11}\text{C}$ time difference:
 Figures 5.15 and 5.16 demonstrate that ^{11}C is in fact produced in company with muon-induced neutrons. For a time difference of less than 1.5 h ($\tau(^{11}\text{C}) = 29.40\text{ m}$) a clear peak due to the exponential correlation in Formula (5.30) is visible. On the other hand, for a time difference of more than 1.5 h , no correlation is visible and the distribution is following an uncorrelated r^2 -behavior. As a result of geometrical effects, the distribution bends down at $\sim 3\text{ m}$. Neutrons are not restricted in their position, however ^{11}C candidates are limited to the FV with a radius of 3.276 m . In order to avoid this geometrical distortion, the fit in Figures 5.15 and 5.17 are performed to an upper limit of 2.5 m .
- Badly reconstructed neutrons:
 As described in sec. 4.4.2, muon afterpulses can reach into the neutron trigger gate and distort energy and position determination. A criterion to identify these neutrons is their cluster mean time (described in sec. 5.3.4).

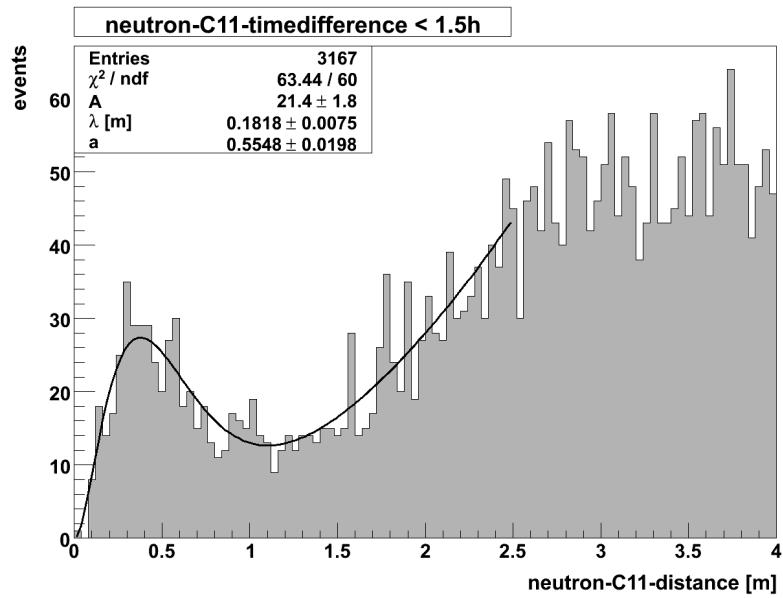


Figure 5.15: Radial distance of neutrons and ^{11}C candidates for a time difference less than $1.5h$. The distribution is fitted according to Formula (5.30).

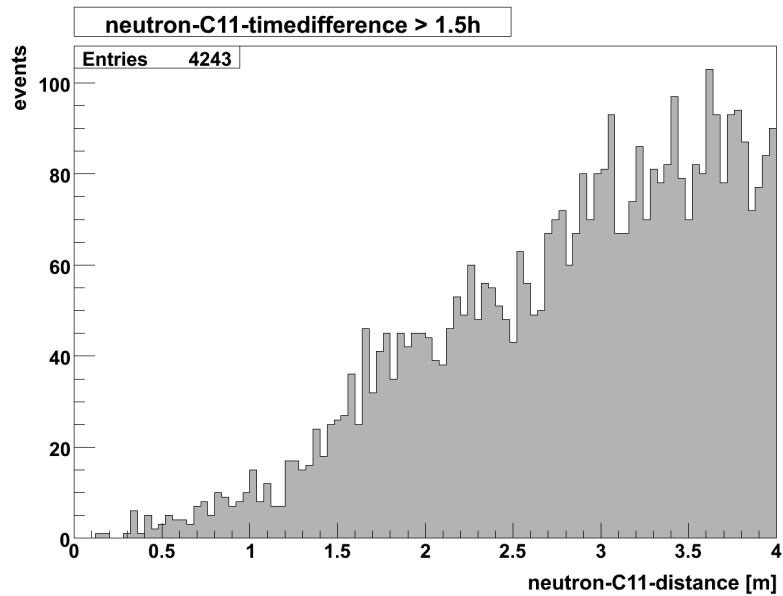


Figure 5.16: Radial distance of neutrons and ^{11}C candidates for a time difference greater than $1.5h$.

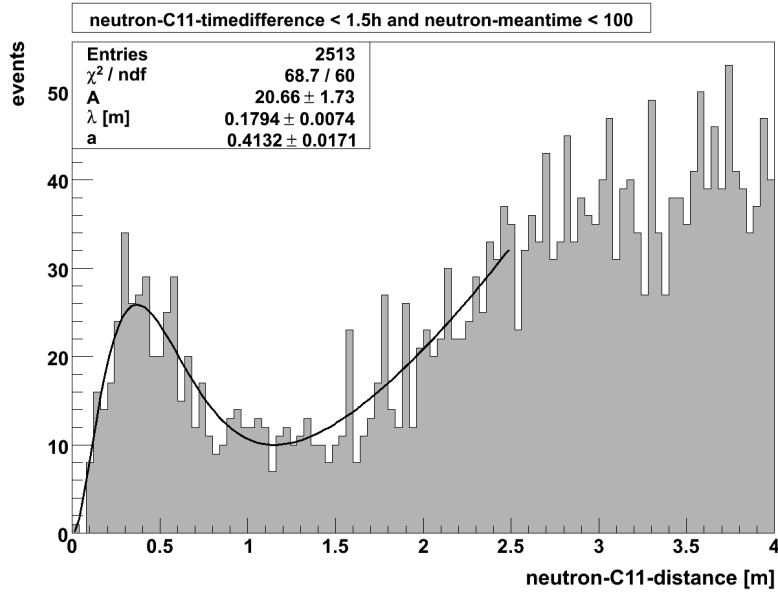


Figure 5.17: Radial distance of neutrons and ^{11}C candidates for a time difference less than $1.5h$ and a neutron-cluster mean time less than 100 ns . The distribution is fitted according to Formula (5.30).

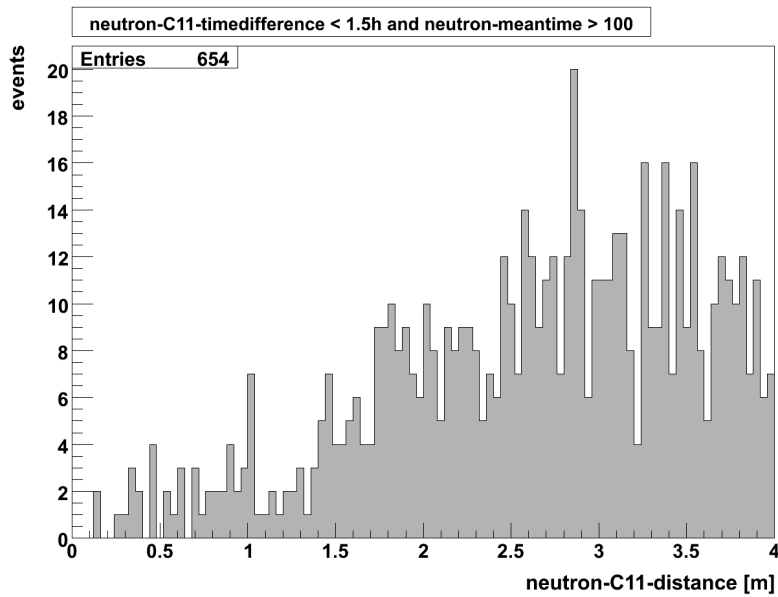


Figure 5.18: Radial distance of neutrons and ^{11}C candidates for a time difference less than $1.5h$ and a neutron-cluster mean time greater than 100 ns (badly reconstructed neutrons).

The influence of a mean time cut of 100 ns is shown in Figures 5.17 and 5.18. Both plots show the distance distribution for a time difference less than 1.5 h . However, they differ in the mean time cut applied. As one can see, neutrons with a cluster mean time $< 100\text{ ns}$ feature the clear peak of spatial correlation, in contrast to neutrons with long mean time. Any spatial correlation is lost as a result of bad neutron position reconstruction. Comparing the fits of Figures 5.15 and 5.17, the influence of badly reconstructed neutrons to the fitted effective mean free path is minimal.

The fits performed with eq. (5.30) neglect a gaussian contribution due to the muon track and neutron positional reconstruction resolution. However, for a study on correlations in the data, it is sufficient to consider effective values. The effective mean free path of neutrons in Borexino is determined to $17.94 \pm 0.74\text{ cm}$. Apart from the distance between neutrons and ^{11}C events, the alignment in space is also of interest. The majority of muons are entering the detector from above, also do the muons which produce neutrons in nuclear reactions.

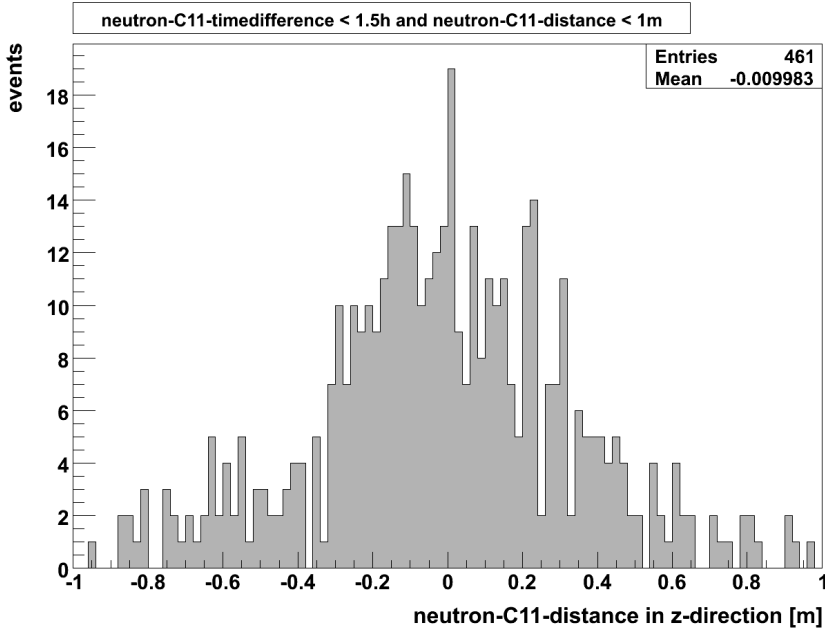


Figure 5.19: Distance of neutrons and ^{11}C candidates in z-direction for time difference less than 1.5 h and neutron- ^{11}C distance less than 1 m . Negative numbers correspond to neutrons which are below the detected ^{11}C candidate.

Figure 5.19 shows the distribution of the distance between neutron and ^{11}C projected on the z-axis. Cuts in time ($< 1.5\text{ h}$) and space ($< 1\text{ m}$) are chosen to

yield a high number of real neutron- ^{11}C pairs. The peak at zero is a consequence of the radial exponential described in Formula (5.30). This distribution features a mean value of -0.9 cm , which is within statistical fluctuations compatible with zero. There are as many neutrons above as below the ^{11}C events. The directional information of the parent muon is therefore not transferred to the induced neutrons in the process of ^{11}C production. They are ejected isotropically from the parent ^{12}C nucleus.

^{11}C mean lifetime

With the detection of a muon-induced neutron, the potential production of ^{11}C is flagged. By recording the time difference between these neutron events to following ^{11}C candidates, one expects a time profile according to Formula (5.29) (sec. 5.4.4) due to the effect of finite runtime. As a prerequisite of this formula, only runs with at least 4 h runtime were chosen for the analysis on the ^{11}C mean lifetime. The resulting data set spans a total runtime of 45.40 d with active neutron trigger. In addition, Formula (5.29) requires, that any ^{11}C is only correlated with maximal one neutron. This prerequisite is met by application of the shower-correction (sec. 5.4.2).

It has to be noted, that the time difference between neutrons and produced ^{11}C is not exactly equal to the life time of the ^{11}C , which is created in the moment the muon is passing the detector. However the mean lifetime of neutrons is $231.6\text{ }\mu\text{s}$ (determined in 5.3.7), and therefore negligible on the time scale for all radionuclides listed in Table 4.3.

Figure 5.20 shows the fit of the temporal distribution. Due to the overlapping energy region of ^{11}C and ^{10}C for $[1.74, 1.02]\text{ MeV}$, ^{10}C decays are present in the short time region of the time distribution ($\tau(^{10}\text{C}) = 27.84\text{ s}$). A time threshold of 2 m is chosen for the fit to avoid these ^{10}C decays.

The good agreement of the fitted ^{11}C mean lifetime of $29.79 \pm 3.82\text{ m}$ with the literature value of 29.40 m proves, that the TFC technique is a powerful tool for tagging radionuclides, especially ^{11}C .

5.4.6 Determination of ^{11}C rate with respect to neutron- ^{11}C distance

By fixing the ^{11}C mean life time to the literature value of 29.40 m (in analysis macros: 0.50 h), Formula (5.29) can be used to determine parameter A , which is the overall number of correlated ^{11}C events in the analyzed data. The analysis is performed again with application of the shower-correction (described in sec. 5.4.2)

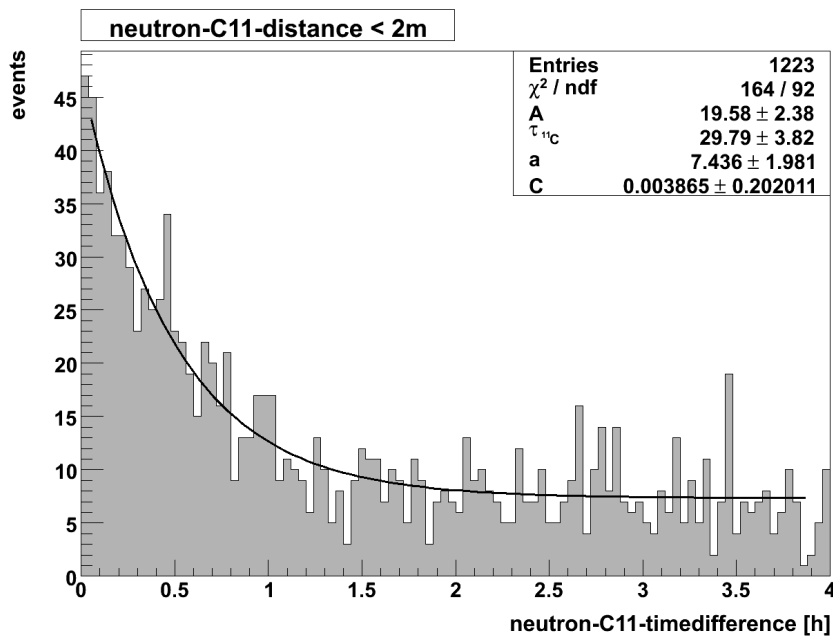


Figure 5.20: Temporal distribution between neutron events and ^{11}C candidates which a spatial distance of less than 2 m , fitted according to formula 5.23. Analyzed runs were chosen by their runtime being greater than 4 h .

and restriction on long runs (runtime $> 4 h$), in order to meet the prerequisites of the modeled time profile in eq. (5.29). As described in sec. 4.3, the final objective of the TFC technique is to reject ^{11}C without losing too much data. With respect to the effective mean free path of the neutron of $17.94 cm$ (determined in the previous section) and the ^{11}C mean lifetime of $29.40 m$, reasonable cuts are:

- Distance between neutron and ^{11}C candidate less than $1 m$
- Time difference between neutron and ^{11}C candidate less than $1 h$

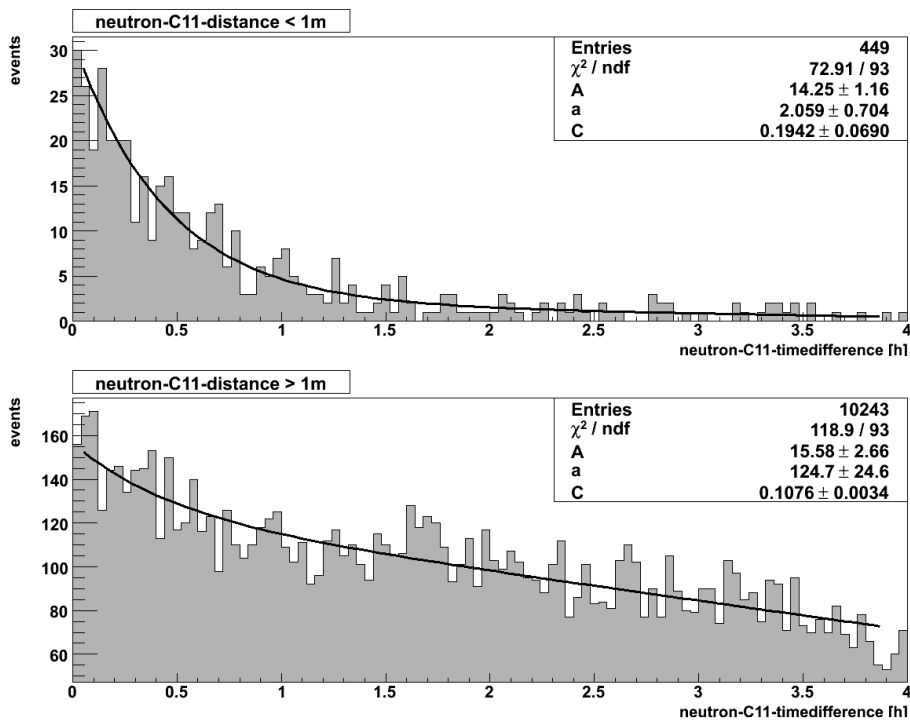


Figure 5.21: Temporal distribution between neutron events and ^{11}C candidates for distance between neutron and ^{11}C candidate of less than $1 m$ (upper plot) as well as more than $1 m$ (lower plot). Both distributions are fitted according to formula (5.29). Analyzed runs were chosen if their runtime was greater than $4 h$.

With a fitted effective neutron mean free path of $17.94 cm$, it is obvious that nearly all correlated ^{11}C events are expected to be within a $1 m$ radius to the neutron. However, there are two reasons which cause a distortion of distance between correlated neutron and ^{11}C events.

1. Badly reconstructed neutrons (described in sec. 5.3.4) :

As shown in Figure 5.18, muon afterpulses tamper the position reconstruction of neutrons. Correlated neutrons of the ^{11}C event are not positioned within a radius of 1 m , but are rather randomly distributed over the whole volume. Due to volumetrical increase (r^2 -behavior), almost all of these neutrons are reconstructed with a distance to the ^{11}C of larger than 1 m .

2. Misidentification of neutrons within a shower:

As described for the shower correction in sec. 5.4.2, all ^{11}C produced within a neutron shower is temporally correlated to all neutrons of the shower. However, each ^{11}C event is correlated in space only with its corresponding knock-off neutron. The Borexino DAQ system usually detects only one neutron of a muon-induced neutron shower due to the *Three-Fast-Trigger-Coincidence* (TFTC) veto. This effect is described in detail in sec. 4.4.2. For high multiplicity events, it is very likely that shower-neutron is detected, which is not the knock-neutron. Figure 5.5 illustrates the spatial distance distribution of consecutive neutrons within a shower. One can see that the shower is distributed over several meters. Therefore, ^{11}C created in high multiplicity neutron showers is expected to be correlated in time with the detected neutron, however correlation in space is most likely lost (see also sec. 5.4.2).

The DAQ sometimes detects more than 1 neutron of a shower, but due to the application of the shower correction, only one of these detected shower neutrons is used for analysis on time profiles.

As a result of these two effects, time correlated neutron- ^{11}C pairs occur also for distances larger than 1 m . Figure 5.21 shows the time profile for the two radial regions of less 1 m and more than 1 m distance between neutrons and ^{11}C candidates. Due to the two effects stated above, ^{11}C decays are present in both distance regions.

In order to transfer the fitted parameter A in a number of events, one has to account for the time binning of the fitted plots. A variation of data binning results in a variation of entries within the bins and thus affects the fit parameter A . To get the number of correlated events, one has to divide by the length of a single time bin. With the full time gate of 4 h separated in 100 bins, a single time bin has a length of $\frac{4\text{h}}{100} = 0.04\text{ h}$.

Table 5.2 shows the results of the analysis. The rate is calculated by the determined number of events divided by the total runtime of long runs of 45.40 d . 52% of all determined ^{11}C is detected at a distance larger than 1 m due to the effects of badly reconstructed neutrons as well as misidentified neutrons. The total rate of correlated ^{11}C events identified by the TFC technique is $16.43 \pm$

neutron- ^{11}C distance	A	number of events	rate
$< 1\text{m}$	14.25 ± 1.16	356 ± 29	7.85 ± 0.64
$> 1\text{m}$	15.58 ± 2.66	390 ± 67	8.58 ± 1.44
Total sum			16.43 ± 1.58
Corrected total sum			17.20 ± 1.65

Table 5.2: Table of correlated ^{11}C events and determination of ^{11}C rate ($\frac{\text{counts}}{\text{day}100\text{tons}}$). Effects considered in the corrected total sum are invisible production channels (4.5%).

Critical radius	rate	rate	total rate
	(< crit. radius)	(> crit. radius)	
1m	8.2 ± 0.7	9.0 ± 1.5	17.2 ± 1.7
2m	11.2 ± 1.0	6.3 ± 2.4	17.5 ± 2.6
3m	13.8 ± 1.5	3.5 ± 2.7	17.3 ± 3.0
4m	16.8 ± 1.9	0.4 ± 1.8	17.3 ± 2.6

Table 5.3: Table of correlated ^{11}C events and determination of ^{11}C rate ($\text{counts } d^{-1} (100 t)^{-1}$). The rates are determined by Formula (5.23) and the shower-correction (sec. 5.4.2) for different radial ranges.

$1.58 \text{ counts } day^{-1} (100 t)^{-1}$. One also has to consider that 4.5% of all muon-induced ^{11}C is produced via invisible channels, as described in sec. 5.4.1. Considering these invisible channels, one gets an overall rate of ^{11}C of $17.20 \pm 1.65 \text{ counts } day^{-1} (100 t)^{-1}$. However this is in disagreement with ^{11}C rates of $26 \text{ counts } day^{-1} (100 t)^{-1}$ determined by spectral fits [50] (see Figure 4.1).

Test of fit stability

The model developed in sec. 5.4.4 as well as the fitting procedure were tested, in order to determine fitting instabilities. The same fit procedure as in the previous section was performed, varying the critical distance, i.e. the distance which divides the distance distribution in two regions. The results of all test fits are shown in table 5.3. The overall numbers of correlated ^{11}C rate are consistent in all tests. The analysis on ^{11}C rates based on the correlations to muons delivers consistent results (sec. 5.4.8).

The disagreement of ^{11}C rates determined by spectral fits and TFC technique is the matter of discussion in sec. 5.4.11.

5.4.7 Spatial ^{11}C -muon correlations

As stated in sec. 4.3 about the TFC technique, muons alone are not feasible to tag the cosmogenic Carbon isotopes due to their high rate (5000 per day in the ID) and the long mean lifetimes of these radionuclide. For analysis on ^{11}C -muon correlations, the neutron trigger is still inevitable. The occurrence of a neutron flags radionuclide production. Thus, only muons are considered for analysis, which are accompanied by at least one neutrons. These muons can be used for an analysis on correlations to the generated radionuclides. Information about the mean distance between muon and radionuclides can decrease significantly the deadtime target mass loss. This second level suppression is also described in sec. 4.3.

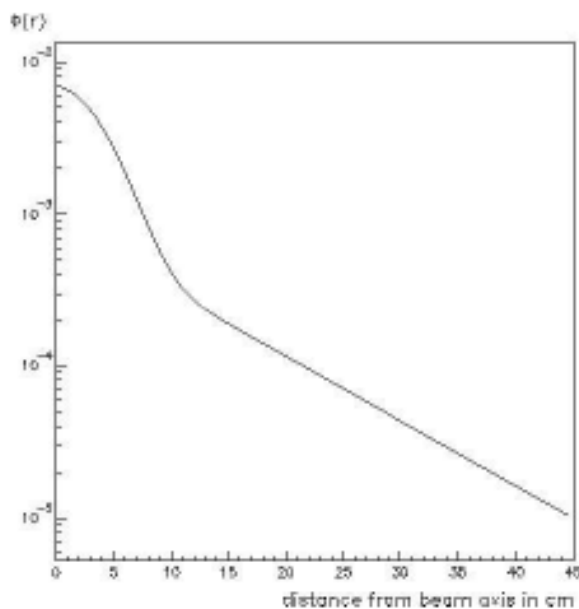


Figure 5.22: Lateral activation profile $\Phi(\rho)$ of ^{11}C with respect to the muon beam, as determined by Hagner et al. at the CERN experiment [47].

An experiment was performed at CERN by Hagner et al. [47] in order to determine the production rates of cosmogenic radionuclides in liquid-scintillator detectors as Borexino. The experimental setup and results of this experiment are presented in sec. 4.2.1. The experiment studied also the lateral distance between the muon beam and the ^{11}C produced within the scintillator. Figure 5.22 shows the result of this study. $\Phi(\rho)$ is the lateral activation profile of ^{11}C according to the following formula:

$$dN(\rho) = 2\pi\rho d\rho \cdot (B\Phi(\rho) + a) \quad (5.31)$$

The normalized distribution function $\Phi(\rho)$ fulfills the condition:

$$\int_0^\infty \Phi(\rho)2\pi\rho d\rho = 1 \quad (5.32)$$

B is the total number of produced ^{11}C and a represents background in the data. The lateral distribution function $\Phi(\rho)$ is determined by Hagner et al. [47] as:

$$\Phi(\rho) = \frac{1}{166} \cdot e^{-0.0403r^2} + \frac{1}{1223} \cdot e^{-0.098r} \quad (5.33)$$

The uncertainty of this function is stated as $\sim 3\%$ for ρ smaller than $\sim 10\text{cm}$ and is increasing to larger lateral distances, e.g. $\sim 18\%$ for $\rho \sim 10\text{cm}$. For a detailed description of uncertainties see dissertation by Hagner [47]. The contribution in (5.33) is dominated by the gaussian. Neglecting the exponential contribution in (5.33), the lateral distribution of ^{11}C can be written as:

$$dN(\rho) = 2\pi\rho d\rho \cdot (Ae^{-\frac{\rho^2}{2\sigma^2}} + a) \quad (5.34)$$

σ is the effective standard deviation of the modeled gaussian lateral profile, while A is the product of B and the gaussian normalization factor. The gaussian in (5.34) is composed by the gaussian activation profile of ^{11}C , as well as the gaussian resolutions of muon track and ^{11}C position reconstruction. For analysis on correlations between reconstructed muon tracks and ^{11}C , it is sufficient to determine the effective spatial distribution.

Figures 5.23 and 5.24 show the lateral distance between reconstructed muon track and ^{11}C candidates as observed in Borexino. The plots differ by the time difference between the muon-induced neutron ^{11}C candidates (less than 1.5h respectively more than 1.5h). As one can see in Figure 5.24, for a time difference larger than 1.5h no sign of correlated events is visible and the distribution is following the linear ρ -behavior of uncorrelated background according to Formula 5.34. With a mean lifetime of 29.40m , almost all ^{11}C has decayed after 1.5h . Due to the elongation of muon tracks, geometrical effects due to the finite size of the IV play an even greater role compared to the neutron- ^{11}C distance distribution (sec. 5.4.5). The muon- ^{11}C distribution gets significantly distorted at $\sim 2\text{m}$.

Figure 5.23 shows the lateral distribution for a time difference less than 1.5h , where a culmination of events in the low lateral distance region is visible. The distribution is fitted according to Formula (5.34) up to a distance of 1.5m . The fit results in a effective standard deviation of the muon- ^{11}C lateral profile of $\sigma = 31 \pm 2\text{cm}$.

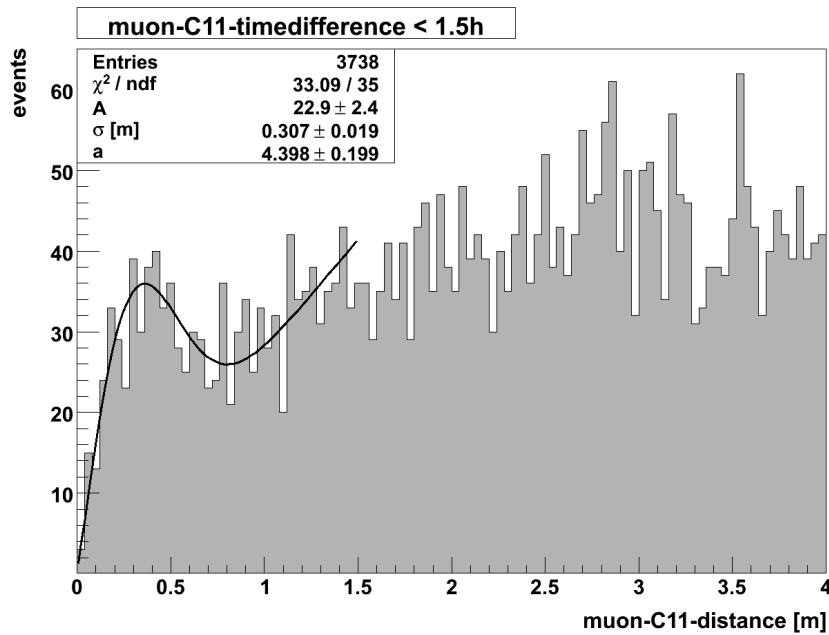


Figure 5.23: Distance between reconstructed muon track and ^{11}C candidates for a time difference less than 1.5h. The distribution is fitted according to formula 5.34

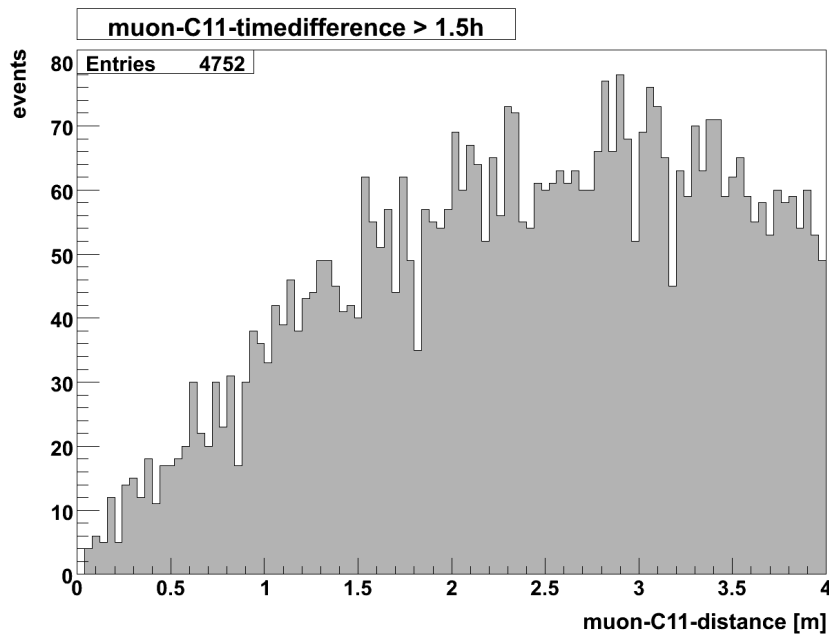


Figure 5.24: Distance between reconstructed muon track and ^{11}C candidates for a time difference more than 1.5h.

5.4.8 Determination of ^{11}C rate with respect to muon- ^{11}C distance

The determination of rates is performed in an analogous manner to sec. 5.4.6. The differences in analysis are:

- No shower correction:
The multiplicity of neutron events has no influence on the muon. Muons used for this analysis just have to be accompanied by at least one neutron in the data, therefore shower correction (sec. 5.4.2) is needless. This is one prerequisite for the modeled time profile of eq. (5.29). No problems due to badly reconstructed neutrons or neutron misidentification arise.
- Total runtime:
For the determination of ^{11}C with respect to the spatial distance to the neutrons, the total runtime was defined by runs with active analogue neutron trigger and at least 4 h runtime. The neutron trigger is activated by the OD and therefore even active when the muon crate is disabled. However, when the muon crate is offline, no information on hits is written to data base and thus no track reconstruction is possible. For the analysis with respect to muon tracks, only the part of a run with active muon crate is taken. The muon sensitive duration of a run has to be of at least 4 h to be analyzed, resulting in data set with total runtime of 45.26 d. This is the second prerequisite for the modeled time profile in eq. (5.29).
- Muon track reconstruction efficiency:
The reconstruction algorithm outlined in sec. 4.4.1 is sometimes not able to reconstruct the muon track. This is the case, when the algorithm does not find 2 clusters or can not split a detected single cluster. In the data set 2.26% of all muon events could not be reconstructed by the algorithm. As ^{11}C production is independent from the success of muon track reconstruction, one has to apply this correction factor to the ^{11}C rates determined by the TFC technique with muon tracks.

Taking a look at Figure 5.23 one can see that for rate determination of ^{11}C a spatial cut of 1 m for lateral distance between muon and ^{11}C candidates is reasonable. According to this cut, time profiles for distance regions of less respectively more than 1 m are plotted in Figure 5.25. They are fitted according to the modeled time profile function (5.29).

The number of correlated ^{11}C events is determined again with the fitted value of A and considering the length of a time bin (0.04 h). The rate is calculated by

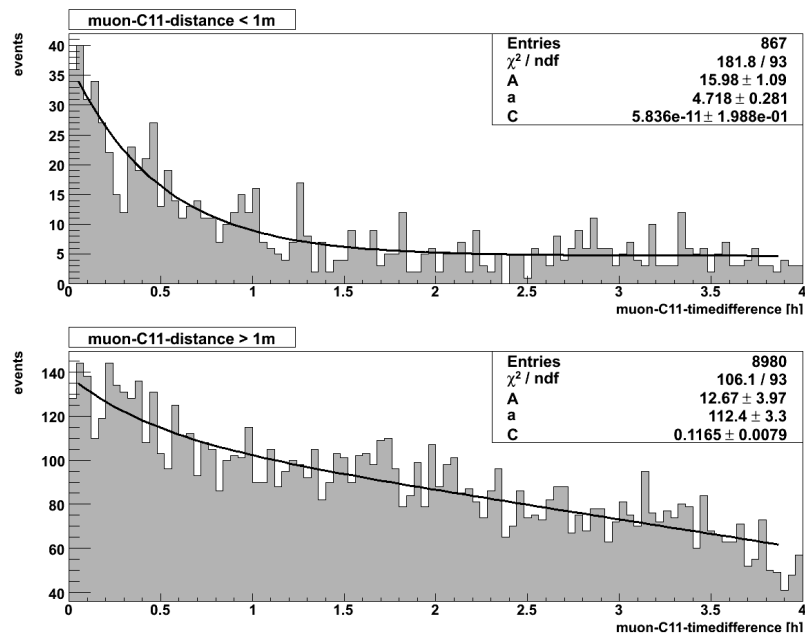


Figure 5.25: Temporal distribution between muon-neutron coincidences and ^{11}C candidates for lateral distance between muon and ^{11}C candidate with critical lateral distance 1 m . Both distributions are fitted according to Formula (5.29).

muon- ^{11}C distance	A	number of events	rate
$< 1m$	15.98 ± 1.09	400 ± 27	8.83 ± 0.60
$> 1m$	12.67 ± 3.97	317 ± 99	7.00 ± 2.19
Total sum			15.83 ± 2.27
Corrected total sum			16.96 ± 2.43

Table 5.4: Table of correlated ^{11}C events and determination of ^{11}C rate ($\text{counts } d^{-1} (100t)^{-1}$). Effects considered in corrected total sum are invisible production channels (4.5%) and muons with failed reconstruction (2.26%).

the event number divided by the analyzed total runtime of $45.26 d$. Furthermore, the runtime is corrected for invisible production channels (4.5%) (see sec. 5.4.1) and failed muon reconstruction (2.26%). Table 5.4 shows the results of these calculations. On basis of the effective standard deviation $\sigma = 31 \pm 2 cm$ of spatial muon- ^{11}C correlations (measured in the section before), one expects nearly all ^{11}C decays within a lateral distance of $1 m$ to the muon track.

However, the high number of events for a lateral distance larger than $1 m$ indicates, that a large number of muons is badly reconstructed. The spatial correlation for these muons events is distorted, and only temporal correlation to ^{11}C decays remains.

This accounts for 44% of all detected ^{11}C . Thus, the analysis on ^{11}C rates yields information on the reliability of the muon track reconstruction. However, it has to be pointed out, that the used muon track reconstruction algorithm [46] is one of the very first version of this code. Great progress in the muon track reconstruction is expected in the near future. An outlook on this topic is given in 7.

The determined ^{11}C rate of $16.96 \pm 2.43 \text{ counts } day^{-1} (100t)^{-1}$ is in excellent agreement with the rate determined by neutron- ^{11}C spatial cuts ($17.20 \pm 1.65 \text{ counts } day^{-1} (100t)^{-1}$) in sec. 5.4.6.

5.4.9 Untaggable ^{11}C due to deadtime

Besides the invisible channels in ^{11}C production, there is also another source of untaggable ^{11}C decays. Due to maintenance work or due to the rejection of runs caused by DAQ problems, the deadtime between two validated runs can be of the order of hours. During this time, ^{11}C is produced and can decay during the active run. This “deadtime- ^{11}C ” can not be tagged by the TFC technique because the corresponding neutron event has not been detected.

Figure 5.26 shows a schematic of this situation. A run is stopped and deadtime spans the interval $[0, t_{dead}]$. After this deadtime, a new run is started covering the

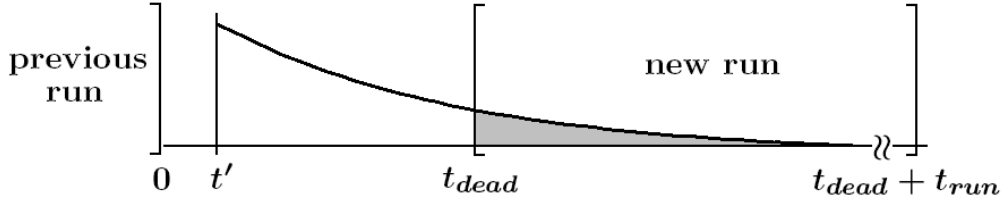


Figure 5.26: Schematics of ^{11}C production during deadtime between runs. ^{11}C is produced in the deadtime at time t' . The gray area illustrates ^{11}C decay during the next active run.

time interval $[t_{dead}, t_{dead} + t_{run}]$. The probability of a ^{11}C nuclide, which is produced during the deadtime at time t , to decay within the active run is:

$$\begin{aligned}
 P(t) &= \frac{1}{\tau} \int_{t_{dead}}^{t_{dead} + t_{run}} e^{-\frac{t'-t}{\tau}} dt' \quad t_{run} \gg \tau \quad \frac{1}{\tau} \int_{t_{dead}}^{\infty} e^{-\frac{t'-t}{\tau}} dt' \\
 &= e^{-\frac{t_{dead}-t}{\tau}}
 \end{aligned} \tag{5.35}$$

The mean duration of runs in Borexino is $\sim 6\text{ h}$ and therefore satisfies the approximation in Formula (5.35) (mean lifetime of ^{11}C is 29.40 m). To get the total number of expected decays in the run, one integrates over the whole deadtime:

$$\begin{aligned}
 N(t_{dead}) &= \int_0^{t_{dead}} P(t) R dt = R \int_0^{t_{dead}} e^{-\frac{t_{dead}-t}{\tau}} dt = \\
 &= R\tau \cdot (1 - e^{-\frac{t_{dead}}{\tau}})
 \end{aligned} \tag{5.36}$$

R is the production rate of ^{11}C . According to spectral fits, the ^{11}C rate is $\sim 26\text{ counts day}^{-1} (100\text{ t})^{-1}$ (Figure 4.1). Applying Formula 5.36 with this rate on the data set, one gets an total number of expected deadtime ^{11}C decays of 72 events. With a runtime of 60.6 days, this corresponds to a mean rate of untaggable ^{11}C of $1.2\text{ counts day}^{-1} (100\text{ t})^{-1}$. 35% of the ^{11}C energy spectrum covers the *pep/CNO* energy window 4.3. This results in a rate of $0.42\text{ counts day}^{-1} (100\text{ t})^{-1}$ within this window. Compared to the expected neutrino rate in the *pep/CNO* window of $\sim 1.5\text{ counts day}^{-1} (100\text{ t})^{-1}$ (Table 4.3), this is not a negligible background contribution.

In combination with the intrinsic inefficiency of the TFC technique of 4.5% due to invisible channels (sec. 5.4.1) corresponding to $0.4\text{ counts day}^{-1} (100\text{ t})^{-1}$ in the *pep/CNO* window (based on the spectral determined ^{11}C rate of $26\text{ counts day}^{-1} (100\text{ t})^{-1}$), the total amount of untaggable ^{11}C rate ($1.6\text{ counts day}^{-1} (100\text{ t})^{-1}$) competes with the ν -signal.

5.4.10 Reduction of cosmogenic ^{11}C background

The main purpose of the TFC technique is to discard cosmogenic ^{11}C from the data in order to measure the low rates of pep - and CNO - ν . As described in sec. 4.3, the ^{11}C suppression can be performed on a first and also a second level. As a reminder, first level suppression discards all events within a given time gate t in a sphere r around the detected neutrons. In second level suppression only the intersection of the sphere with a cylinder defined by the muon track is blinded out, in order to reduce loss of exposure.

Based on the effective mean free distance between neutron and ^{11}C events of 17.94 cm (determined in sec. 5.4.5), a 1 m cut around the neutron is reasonable. However correlations on ^{11}C rates via neutrons show, that 52% of determined ^{11}C is detected at a distance larger than 1 m due to badly reconstructed neutrons as well as misidentified neutrons (see sec. 5.4.6). On the other hand, ^{11}C rates determined by muons indicate, that muons are badly reconstructed for 44% of all detected ^{11}C events (sec. 5.4.8). These effects disrupt spatial correlation between the three particles neutron, ^{11}C and muon and thereby render the second level suppression inapplicable.

Therefore, reduction of ^{11}C is achieved in this thesis by applying only the first level suppression. As already mentioned, a spatial cut of ^{11}C -neutron distance less than 1 m , as well as a temporal cut of 1 h (i.e. $\sim 2 \cdot \tau(^{11}\text{C})$) are applied. All events with a *charge* value greater than 400 pe fulfilling these cuts are discarded. Figure 5.27 shows the *charge* spectrum before (red) and after removal of these events (blue). No restriction on duration of a run is made, resulting in a data set with a total runtime of 54.04 d . According to the results obtained in sec. 5.4.6 (Table 5.2), for a distance less than 1 m one expects a ^{11}C rate $R_{r<1\text{m}}$ of $8.22 \pm 0.61\text{ counts day}^{-1} (100\text{ t})^{-1}$ (effect due to invisible channels (4.5%) included). Considering also the time cut of 1 h one expects the following number of removed ^{11}C :

$$N_{remov} = R_{r<1\text{m}} \cdot t_{run;total} \cdot (1 - e^{-\frac{1\text{h}}{\tau}}) = 361.96 \pm 28.56\text{cpd} \quad (5.37)$$

One can compare this expectation with real event subtraction. The charge spectrum contains 1974 events in the ^{11}C region ($[400,950]\text{ pe}$) before TFC is used. After the removal of events by TFC technique 1599 events are still present, corresponding to a reduction of 375 events. It has to be remarked, that this number of subtracted events also contains other radionuclides. However due to their low rate, the only mentionable radionuclide is ^{10}C which spectrum intersects with ^{11}C in the energy region $[1.74,198]\text{ MeV}$ (sec. 5.2.4). Nevertheless this component is negligible in comparison to the statistical error of expected event reduction ($R(^{10}\text{C}) \sim 2\text{ counts day}^{-1} (100\text{ t})^{-1}$) (Table 4.3). Therefore, the expectation is in good agreement with the results obtained by event rejection. Nevertheless even

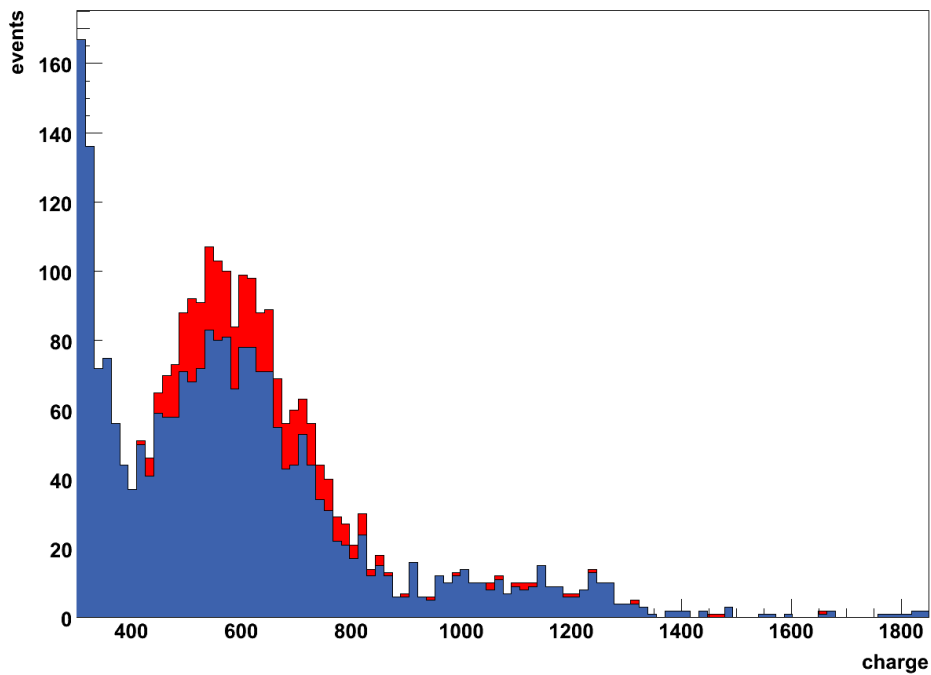


Figure 5.27: Charge spectrum of the Fiducial Volume filtered from neutron and muon events (red). Blue plot shows the charge spectrum after additional removal of all events with a charge value greater than 400 pe within 1 m and 1 h after a neutron event.

after application of TFC a lot of ^{11}C is still left. The low ^{11}C rejection efficiency of the TFC technique for the given detector configuration of analysis is the result of badly reconstructed neutrons as well as misidentification of shower neutrons. Both sources disrupt the neutron- ^{11}C distance and therefore restrict the cut based on spatial correlations (described in sec. 5.4.6).

5.4.11 Discussion on efficiency of analysis

The expected ^{11}C rate determined by application of the TFC technique is $17.20 \pm 1.65 \text{ counts } d^{-1} (100 t)^{-1}$ for ^{11}C -neutron spatial cuts (sec. 5.4.6) respectively $16.96 \pm 2.43 \text{ counts } d^{-1} (100 t)^{-1}$ for ^{11}C -muon spatial cuts (sec. 5.4.8). However the determination of ^{11}C rate by means of spectral fits results in a value of $26 \text{ counts } d^{-1} (100 t)^{-1}$ (Figure 4.1).

Therefore, the distortions of correlations in data analysis shall be summarized:

1. Badly reconstructed neutrons

Muons crossing the Inner Vessel (IV) produce a huge amount of light which often excites the photomultiplier tubes (PMT). These excited PMTs can produce fake signals (so called afterpulses), which can reach into the time window of the analogue neutron trigger and disturb the *charge* and position reconstruction of a neutron event. Spatial correlation between ^{11}C and neutron is lost, and therefore ^{11}C can not be tagged by its distance to the neutron event. These badly reconstructed neutrons are identified within analysis by a mean time cut of the neutron cluster being larger than 100 ns . About 16% of of all detected neutron events belong to this category. This topic is covered in sec. 5.3.4.

2. Detection inefficiency in high neutron-multiplicity events

Due to the *Three Fast Trigger Coincidence* (TFTC) veto usually only one neutron of a muon-induced shower was detected by DAQ of Borexino. This neutron is usually not the one corresponding to ^{11}C production in the shower, and therefore spatial correlation is almost lost. See sec. 5.4.6 for more information.

3. Badly reconstructed muon tracks

The distribution of distances between reconstructed muon tracks and ^{11}C candidates shows a strong spatial correlation. With a fitted effective standard deviation of σ of $31 \pm 2 \text{ cm}$ (sec. 5.4.7), almost all correlated ^{11}C decays are expected to be within 1 m to the parent muon track. However, determination of ^{11}C rates with respect to the lateral distance show, that 44% of all detected correlated ^{11}C events have a distance to muon track larger than 1 m (sec.

5.4.8). This indicates, that many muons are not reconstructed correctly. The spatial correlation between these muons and their induced ^{11}C is disturbed.

4. Time threshold in neutron detection

The first $25\ \mu\text{s}$ of the analogue neutron trigger are blinded out, in order to avoid the main portion of the muon afterpulses. Any neutron decaying during this time is lost for DAQ. With a measured mean neutron capture time of $231.6 \pm 9.9\ \mu\text{s}$ (determined in sec. 5.3.7) this accounts for about 10% of all produced neutrons. The analogue neutron trigger is covered in Section 3.1.2 and 4.4.2.

Effects 1-3 disturb the spatial correlation between the three particles neutron, muon and ^{11}C and therefore reduce the efficiency of a first and second level suppression of ^{11}C (4.3). However, the total rate determined by temporal correlations is independent of these effects (rates determined in sec. 5.4.6, 5.4.8). In the analysis performed in this chapter, a total rate of ^{11}C of about $17\ \text{counts day}^{-1}\ (100\ t)^{-1}$ has been determined, in contrast to ^{11}C rates of $26\ \text{counts day}^{-1}\ (100\ t)^{-1}$ determined by spectral fits. An unknown inefficiency in the identification of muon-induced neutron production is the most likely source of this effect.

This does not refer to the fact that the neutron trigger cannot detect all neutrons in a shower. For correlation in time its enough to detect one neutron of a shower, as explained in sec. 5.4.2. However if no neutron of a shower at all is detected, the produced ^{11}C does not contribute to a correlated distribution in the time profile. As a reminder, an incident with at least one neutron event is referred in this thesis as a neutron shower.

The neutron trigger has a known inefficiency of about 10%, as stated above. However this does not make up an inefficiency in correlated neutron- ^{11}C pairs of 35%. Up to the present, the source of additional inefficiency is unknown. Therefore, additional studies on the TFC correlations are important. The next chapter covers a prospective ^{10}C , which would provide a cross-check on the reliability of the TFC. However, it has to be noted, that great improvements in neutron detection have been recently achieved, and are also expected for muon track reconstruction, described in sec. 7.2. Also for the modified hardware and software condition of Borexino, a study on ^{11}C and also potentially on ^{10}C will provide information on the improved quality of Borexino's capability to reject cosmogenic background.

Chapter 6

Prospective ^{10}C analysis

The analysis performed in Chapter 5 determined a ^{11}C rate of about $17 \text{ counts day}^{-1} (100 t)^{-1}$, based on temporal correlations using the TFC technique (rates determined in sec. 5.4.6, 5.4.8). Spectral fits of the energy spectrum result in a ^{11}C rate of $26 \text{ counts day}^{-1} (100 t)^{-1}$ (Figure 4.1). As stated in Section 5.4.11, one inefficiency arises due to the $25 \mu\text{s}$ time threshold of the analogue neutron trigger, though this contribution cannot account for the total inefficiency in ^{11}C of about 35%. Thus, an additional analysis on ^{10}C by means of the TFC technique (sec. 4.3) is important to perform a consistency check. According to the CERN experiment [47], the rate of cosmogenic ^{10}C is expected to be about $2 \text{ counts day}^{-1} (100 t)^{-1}$ within Borexino (see Table 4.3). Therefore a reasonable analysis on correlations between neutrons, muons and ^{10}C requires a data set with an active measuring time of at least 100 days. This section outlines the major considerations for an analysis on ^{10}C based on the TFC technique with sufficient amount of data.

As outlined in sec. 5.2.4, reasonable selection criteria for ^{10}C candidates are a *charge* value between 700 to 1750 photoelectrons (*pe*). This *charge* cut neglects the energy deposition above 1750 *pe* by the suppressed decay channel of ^{10}C , which occurs in 1.47% of ^{10}C decays (see sec. 5.2.4). With a mean life time of 27.84 s, a time gate after a neutrons of 4 m is suitable. A time threshold of 4 s avoids contributions of the short lived cosmogenic radionuclides, e.g. ^8Li , ^9Li , ^6He (Table 4.3).

6.1 ^{10}C production channels

No official analysis on the contributions of different channels in the process of muon-induced ^{10}C production has been performed yet for Borexino. However, for application of the TFC technique (sec. 4.3) only the contribution of invisible channels is important, i.e. channels with no free neutron in the final state. ^{10}C

produced in these channels cannot be tagged by means of the TFC technique. To produce ^{10}C in the scintillator, ^{12}C has to lose 2 neutrons by interaction with the muon or its secondaries. The only invisible channels are:

- $^{12}\text{C}(p; t)^{10}\text{C}$
- $^{12}\text{C}(\pi^+; \pi^0 + d)^{10}\text{C}$

Both production channels are based on three particle processes with bond final states, and therefore are extremely unlikely. They are strongly suppressed in comparison to production channels without bond states, which result in at least one free neutron. On the basis of this, the contribution of invisible channels in ^{10}C production can be assumed as negligible.

6.2 Influence of DAQ deadtime

Due to the short mean life time of ^{10}C of 27.84 s, several problems (sec. 5.4.11) of ^{11}C analysis are not present. Effects due to finite run duration are not present (sec. 5.4.3), and thus the model of time profile used in ^{11}C analysis is not required (see sec. 5.4.4). However, shower correction is still necessary to avoid multi-counting of ^{10}C decays due to multiple-neutron showers (sec. 5.4.2).

6.3 ^{10}C signal and background

The main background sources for an analysis on ^{10}C are cosmogenic ^{11}C and external γ -radiation due to ^{208}Tl present in the PMT glass. The main difference of these two background sources with respect to analysis is the temporal correlation to previous neutron events. Whereas the external γ -background from Thallium is completely uncorrelated and therefore expected as a flat contribution in the time profile, the ^{11}C decays are correlated with previous neutrons. The expected time profile is:

$$dN(t_{diff}) = \frac{A_{11\text{C}}}{\tau_{11\text{C}}} e^{-\frac{t_{diff}}{\tau_{11\text{C}}}} + \frac{A_{10\text{C}}}{\tau_{10\text{C}}} e^{-\frac{t_{diff}}{\tau_{10\text{C}}}} + a \quad (6.1)$$

The parameter A_C represents the number of correlated events of ^{10}C respectively ^{11}C , with τ the decay time of either Carbon isotope. a is the result of uncorrelated background, from whom the external γ -background is part of. Both background contributions are described in detail in the following:

- External γ -background:

The uncorrelated γ -background does not influence the determination of correlated ^{10}C rate. However, it is quite dominant in the ^{10}C energy range and may reduce the significance of the time profile fit (see sec. 5.2.4 and Figures 5.1, 5.3). The contribution of the external γ -rays is strongly limited to the outer parts of the FV. The FV is defined by a target mass of 100 t and has been determined to a radius of 3.276 m . The external background can be reduced to a great extent by application of radial cuts, though accompanied by a quite high loss of target mass.

- Cosmogenic ^{11}C background:

Both ^{10}C and ^{11}C are correlated with muon-induced neutron events. Due to their overlapping time and energy spectra, ^{11}C is expected as the major background for a ^{10}C analysis. ^{11}C radionuclides decay with a mean life time of 29.40 m and therefore significantly contributes within the ^{10}C time window of 4 m . ^{11}C cannot be discarded from the ^{10}C analysis by means of a temporal cut. However, applying a cut in the energy, one can reject ^{11}C . The decay energies of both Carbon isotopes intersect in the region of $[1.74, 1.982]\text{ MeV}$, corresponding to a *charge* region of $[700, 950]\text{ pe}$. By discarding this energy region, ^{11}C is excluded and the time profile stated in Equation 6.1 is reduced to a single exponential due to ^{10}C with a flat background contribution. This *charge* cut limits the selection of ^{10}C candidates to a *charge* range of 950 to 1750, introducing an inefficiency in the rate determination.

Eventually analysis on ^{10}C has to account for inefficiencies introduced by the possible restrictions in charge selection of candidates, i.e. a low energy cut avoiding ^{11}C decays as well as the negligence of ^{10}C decays due to the suppressed decay channel above a *charge* value of 1750 pe .

Chapter 7

Summary, Outlook and Conclusion

7.1 Summary

Borexino has been commissioned on 16th of May 2007 and has published first results on real time detection of ${}^7\text{Be}$ neutrinos in 16th of August 2007. The measured ${}^7\text{Be}-\nu$ rate of $47 \pm 7_{stat} \pm 12_{sys} \text{ counts day}^{-1} (100 t)^{-1}$ is in agreement with expectations of the MSW-LMA oscillation solution.

With the detection of the ${}^7\text{Be}$ neutrinos, great effort has been performed to achieve a direct measurement of the remaining solar fluxes from pp/pep , CNO and ${}^8\text{B}$ neutrino emissions. Cosmogenic background from ${}^{11}\text{C}$ and ${}^{10}\text{C}$ is the main background source for the high energetic solar neutrino fluxes. The expected ${}^{10}\text{C}$ production rate of $\sim 0.6 \text{ counts day}^{-1} (100 t)^{-1}$ in the ${}^8\text{B}-\nu$ window is comparable with the neutrino signal within this window. However, especially the ${}^{11}\text{C}$ rate of $\sim 26 \text{ counts day}^{-1} (100 t)^{-1}$ (determined by spectral fits) exceeds the signal from pep and CNO neutrinos ($\sim 1.5 \text{ counts day}^{-1} (100 t)^{-1}$) by an order of magnitude. For a measurement of these neutrino fluxes, it is critical to reject cosmogenic background.

The *Three-fold Coincidence* (TFC) technique is a powerful tool to achieve this goal. It is based on correlations in space and time between the three particles muon, neutron and the particular cosmogenic radionuclide (${}^{11}\text{C}$ or ${}^{10}\text{C}$).

The main part of this thesis has been dedicated to the analysis of these correlations and the efficiency of the TFC technique in Borexino. As the most prominent cosmogenic background, ${}^{11}\text{C}$ suites excellent for these studies.

As participating particle of the TFC, correct muon reconstruction but moreover correct muon identification are indispensable. Thus, a calibrated and fully func-

tional detector is essential. In the frame of this work, a pulser system to monitor the electronics status of the Outer Detector (OD) has been constructed and implemented into the electronics read-out chain. The newly installed pulser system injects a reference signal into the OD electronics and thereby checks its operational reliability for each run. By now, this pulser system is an inherent part of calibration and maintenance work of the Borexino detector.

In addition an analysis has been performed on correlations between the three particles participating in the TFC, i.e. neutron, muon and ^{11}C . On basis of Borexino's offline data processing software *Echidna*, a data set of 54 d has been prepared for analysis. Calibration events are excluded, as well as radioactive background from ^{214}Bi on basis of the fast coincidences with its daughter nuclide ^{214}Po . Furthermore, a set of identification criteria for the particles neutrons, muons and the cosmogenic radionuclides establish the basis of analysis on correlations.

The analysis is performed on data taken by Borexino in the time period of 07/10/07 until 10/27/07. Due to electronics problems, Borexino's main data acquisition (DAQ) system was limited in its efficiency in neutron detection of multiple neutron showers. As a result of the so-called *Three Fast Trigger Coincidence* (TFTC) veto, usually only one neutron of a muon-induced shower was detected. The influence of this effect on the muon-neutron time profile is discussed and a fitting model is presented. The mean neutron capture time in the liquid-scintillator detector Borexino has been determined as $232 \pm 10 \mu\text{s}$.

The study on correlations between muons and neutrons also provides insight to the distance between reconstructed neutrons and muons tracks. On the basis of these correlations, an effective lateral mean free path of the reconstructed neutrons with respect to reconstructed muon tracks of $43 \pm 1 \text{ cm}$ has been determined.

The central part of this thesis is the analysis of correlations in time and space between ^{11}C and neutrons/muons. The analysis on spatial correlations between ^{11}C and neutrons results in a effective neutron mean free path between reconstructed neutron and ^{11}C position of $18 \pm 1 \text{ cm}$. In addition, the influence of badly reconstructed neutrons for the TFC technique is discussed and demonstrated. These neutrons loose their spatial correlation to ^{11}C and therefore decrease the efficiency of the TFC technique.

Furthermore, the effect of finite run durations on temporal correlations is discussed in detail. A model of the time profile is developed and successful applied in determination of the mean life time of ^{11}C . A measured mean lifetime of $29.79 \pm 3.82 \text{ m}$ is in excellent agreement with the expected value of 29.40 m .

The model of time profile is applied for rate determination of ^{11}C by means of

previous neutron/muon events. The total ^{11}C rate determined by application of the TFC technique is $17.20 \pm 1.65 \text{ counts day}^{-1} (100 t)^{-1}$ for ^{11}C -neutron spatial cuts, respectively $16.96 \pm 2.43 \text{ counts day}^{-1} (100 t)^{-1}$ for ^{11}C -muon spatial cuts. Both analysis are in excellent agreement, and prove the reliability of the developed model of time profiles.

Eventually, the TFC technique is applied to reject ^{11}C from the data. A sphere of 1 m radius around each detected neutron is blinded out for 1 h. According to the analyzed correlations, a rejection of a ^{11}C rate of $6.78 \pm 0.55 \text{ counts day}^{-1} (100 t)^{-1}$ is expected. The number of discarded events is in good agreement with this. After application of the TFC technique, ^{11}C is still present with a rate of $\sim 19 \text{ counts day}^{-1} (100 t)^{-1}$. This is caused by loss of spatial correlation due to badly reconstructed neutron events, and misidentification of neutrons in a neutron-shower.

As mentioned above, the total production rate of ^{11}C determined in this thesis on basis of the TFC is $\sim 17 \text{ counts day}^{-1} (100 t)^{-1}$. These values differ from the rate obtained by spectral fits ($\sim 26 \text{ counts day}^{-1} (100 t)^{-1}$). This result implies a total inefficiency of the TFC of 35% within the frame of Borexino's hardware and software configuration of the analyzed time period. The most likely source of this discrepancy is an inefficiency in neutron detection.

An additional test of this technique on basis of the cosmogenic ^{10}C is important for consistency checks. Due to the low rate of ^{10}C , analysis on this radionuclide is not feasible with the data set used in this thesis. However, the procedure and main features of potential analysis on ^{10}C on basis of sufficient statistics is outlined in this thesis.

Besides the efficiency of the TFC, the impact of deadtime between active runs has been analyzed, too. ^{11}C produced during this deadtime can not be tagged by the TFC technique, however it can decay during an active run. Considering also invisible channels of ^{11}C production, the total amount of untaggable ^{11}C for the given data set is determined $1.6 \text{ counts day}^{-1} (100 t)^{-1}$ which is in the order of magnitude of the expected *pep/CNO- ν* signal of $\sim 1.5 \text{ counts day}^{-1} (100 t)^{-1}$. This result was presented during a meeting within the Borexino collaboration and the importance of short deadtimes between runs has been acknowledged.

However, the status of neutron detection, muon track reconstruction, untaggable ^{11}C described in this thesis only represents the first steps of ongoing work on Borexino's capability of discarding cosmogenic radionuclides. Great improvements in neutron detection have been recently achieved by the collaboration and also muon track reconstruction is constantly improved.

7.2 Outlook

Effort is currently performed by the Borexino collaboration to increase the efficiency of the TFC technique. The detector is continuously modified and tuned for maximum performance and great improvements in neutron detection have been recently achieved. Also, muon track reconstruction is subject of steady development and expected to improve significantly.

7.2.1 Neutron detection

Since 11/27/07 the analogue neutron trigger of Borexino has been modified to solve the problem of the detection inefficiency in high neutron-multiplicity events. The *Three-Fast-Trigger-Coincidence* (TFTC) is activated, when 2 triggers occur less than $\sim 200 \mu s$ apart. When this is the case, the veto prohibits any additional trigger within the next $\sim 2 ms$. This prevented the detection of all neutrons of a multiple-neutron shower.

The new configuration of the analogue neutron trigger activates a single trigger with a time gate of $1.6 ms$. During this time, all events are written in the same data acquisition gate. Eventually, an algorithm identifies the neutron candidates according their energy in the offline data processing of the run. Because all neutrons are detected by a single trigger, this method bypasses the TFTC veto and allows the detection of all neutrons.

A great improvement in the rejection of ^{11}C and ^{10}C based on the TFC technique is expected. An additional analysis on ^{11}C (respectively ^{10}C) with the new setup of the neutron trigger will probe the efficiency of the Borexino detector, to measure *pep*- and *CNO*-neutrinos.

7.2.2 Muon track reconstruction

The analysis on muons in this thesis is based on one of the first versions of the *Muon Track Reconstruction* (MTR) algorithm of the *Outer Detector* (OD) (date of the version: 11/05/07). The analysis performed in this thesis on correlations between ^{11}C and muons demonstrated, that this early version of the OD MTR is capable to correctly reconstruct about 44% muons.

On basis of simulations, the OD MTR has been continuously improved and is an integrated module of the *Echidna* software framework by now. Furthermore, the use of a muon sampler has been recently proposed within the Borexino collaboration. The deployment of an external muon sampler with high spatial reconstruction capabilities on top of the Borexino detector would allow a direct comparison to the reconstructed muon tracks.

On basis of the enhancement of the OD MTR algorithm, an improvement in the reconstruction reliability is expected. Furthermore, an additional MTR algorithm for the *Inner Detector* (ID) is currently under development. Similar to its OD counterpart, the algorithm for the ID identifies the entry and exit point of the muon on the inner surface of the *Stainless Steel Sphere* (SSS). Due to the higher area coverage of PMTs and increased light yield in the ID, a good reconstruction capability of this future ID MTR algorithm is expected. A combination of both algorithm is under discussion. Nevertheless, an significant improvement in the reconstruction of muons is anticipated.

7.3 Conclusion

The analysis in this thesis demonstrated, that correlations between neutron, muon and ^{11}C are present in Borexino's data, and can be utilized to reject cosmogenic background. Although the configuration of the experiment in the analyzed time period was not sufficient to reduce the cosmogenic ^{11}C background to the required level of *pep*- and *CNO- ν* detection, this configuration just represents the first steps of Borexino in achieving this goal. The detector has been greatly modified to improve the efficiency of the TFC technique, and recent developments in neutron detection and muon track reconstruction have significantly enhanced the efficiency of this powerful technique. Further improvements in muon track reconstruction are at hand, which will provide an additional tool to tag cosmogenic radionuclides in the data. According to these results, it is anticipated that Borexino will succeed in reducing the cosmogenic ^{11}C background via the TFC technique to the necessary level for *pep*- and *CNO- ν* detection.

Thus also in the future, studies on correlations between neutrons, muons and ^{11}C (respectively ^{10}C) will provide crucial information on the reliability of the TFC technique and the efficiency of the improved configuration of Borexino.

List of Figures

1.1	Schematics of the pp -chain	7
1.2	Schematics of the $CNO-I$ cycle	8
1.3	Expected solar neutrino spectrum	9
1.4	Solar neutrino survival probability in the LMA scenario	10
2.1	Schematics of the Borexino experiment	21
2.2	Expected electron-recoil spectrum in Borexino	24
2.3	Measured electron-recoil spectrum in Borexino	25
3.1	Timing sequence of the analogue neutron trigger	28
3.2	Schematics of the Outer Detector electronics racks	30
3.3	<i>High Voltage Decoupler</i> frame with integrated <i>Pulser System Connectors</i>	32
3.4	Interior of the <i>High Voltage Decoupler</i> frame	33
3.5	Outer detector electronics with integrated Pulser System	34
4.1	Fit of the energy spectrum of Borexino	44
4.2	Schematics of the Three-fold Coincidence	48
4.3	Integrator output after a muon pulse	50
5.1	Charge spectrum of Borexino	59
5.2	Charge spectrum of ^{11}C	60
5.3	Charge spectrum of ^{10}C	61
5.4	Distribution of neutron multiplicities	63
5.5	Distribution of distance of consecutive neutrons	65
5.6	Number of hits of neutron candidates	67
5.7	Number of hits of badly reconstructed neutron candidates	67
5.8	Lateral distance of neutron events to muon track	69

List of Figures

5.9	Multiple-exponential fit of neutron time distribution	70
5.10	Single-exponential fit of neutron time distribution	72
5.11	Schematics of muon, neutron and ^{11}C correlations	74
5.12	Deformation of the ^{11}C time profile	80
5.13	Deformed time profiles for different run durations	81
5.14	Model of summed time profiles	81
5.15	Neutron- ^{11}C distance (time difference $< 1.5 h$)	85
5.16	Neutron- ^{11}C distance (time difference $> 1.5 h$)	85
5.17	Neutron- ^{11}C distance (time difference $< 1.5 h$, meantime $< 100 ns$)	86
5.18	Neutron- ^{11}C distance (time difference $< 1.5 h$, meantime $> 100 ns$)	86
5.19	Neutron- ^{11}C z-displacement	87
5.20	Fit of ^{11}C mean lifetime	89
5.21	Fit of ^{11}C rates based on neutron correlations	90
5.22	Lateral ^{11}C activation profile	93
5.23	Muon- ^{11}C distance (time difference $< 1.5 h$)	95
5.24	Muon- ^{11}C distance (time difference $> 1.5 h$)	95
5.25	Fit of ^{11}C rates based on muon correlations	97
5.26	Schematics of ^{11}C production during deadtime between runs	99
5.27	Charge spectrum before and after ^{11}C rejection	101

List of Tables

1.1	Expected solar neutrino fluxes	10
4.1	Neutrino windows in Borexino	43
4.2	Half-life times of cosmogenic radionuclides	46
4.3	Cosmogenic background and solar neutrino rates	46
5.1	^{11}C production channels	73
5.2	^{11}C rates based on neutron correlations	92
5.3	^{11}C rates for different distances	92
5.4	^{11}C rates based on muon correlations	98

Bibliography

- [1] B. T. Cleveland *et al.*, *Astrophys. J.* **496**, 505 (1998).
- [2] Super-Kamiokande, J. Hosaka *et al.*, *Phys. Rev.* **D74**, 032002 (2006), hep-ex/0604011.
- [3] A. A. Aguilar-Arevalo and J. C. D'Olivo, *Phys. Rev.* **D66**, 113009 (2002), hep-ph/0211091.
- [4] The KamLAND Collaboration, (2008), arXiv:0801.4589 [hep-ex].
- [5] Super-Kamiokande, T. Kajita, *Nucl. Phys. Proc. Suppl.* **77**, 123 (1999), hep-ex/9810001.
- [6] N. Schmitz, *Neutrino Physik* (Teubner Studienbuecher, Stuttgart, 1987).
- [7] S. P. Mikheyev and A. Y. Smirnov, *Prog. Part. Nucl. Phys.* **23**, 41 (1989).
- [8] L. Wolfenstein, *Phys. Rev.* **D17**, 2369 (1978).
- [9] A. Y. Smirnov, *Phys. Scripta* **T121**, 57 (2005), hep-ph/0412391.
- [10] Particle Physics Booklet, *Journal of Physics G* **33**, 1 (2006).
- [11] T. Lewke, Diploma Thesis, Technische Universitaet Muenchen, 2007 .
- [12] J. Bahcall, Home Page: <http://www.sns.ias.edu/jnb/> (2008).
- [13] J. N. Bahcall and A. M. Serenelli, *Astrophys. J.* **626**, 530 (2005), astro-ph/0412096.
- [14] J. N. Bahcall and C. Pena-Garay, *JHEP* **11**, 004 (2003), hep-ph/0305159.
- [15] D. D'Angelo, Doctor Thesis, Technische Universitaet Muenchen, 2006 .
- [16] O. G. Miranda, M. A. Tortola, and J. W. F. Valle, *AIP Conf. Proc.* **917**, 100 (2007).

- [17] GNO, M. Altmann *et al.*, Phys. Lett. **B616**, 174 (2005), hep-ex/0504037.
- [18] P. A. Sturrock and D. O. Caldwell, Astropart. Phys. **26**, 174 (2006), hep-ph/0409064.
- [19] SAGE, J. N. Abdurashitov *et al.*, J. Exp. Theor. Phys. **95**, 181 (2002), astro-ph/0204245.
- [20] Kamiokande collaboration, Phys. Rev. Lett. **77**, 1683 (1996), hep-ex/9810001.
- [21] Super-Kamiokande, S. Fukuda *et al.*, Phys. Lett. **B539**, 179 (2002), hep-ex/0205075.
- [22] SNO, B. Aharmim *et al.*, Phys. Rev. **C72**, 055502 (2005), nucl-ex/0502021.
- [23] S. Dev and S. Kumar, Mod. Phys. Lett. **A20**, 2957 (2005), hep-ph/0504237.
- [24] Borexino, G. Alimonti *et al.*, Astropart. Phys. **16**, 205 (2002), hep-ex/0012030.
- [25] BOREXINO, C. Arpesella *et al.*, Astropart. Phys. **18**, 1 (2002), hep-ex/0109031.
- [26] G. Alimonti *et al.*, Nucl. Instrum. Meth. **A406**, 411 (1998).
- [27] G. Bellini *et al.*, Eur. Phys. J. **C19**, 43 (2001), nucl-ex/0007012.
- [28] Borexino, H. O. Back *et al.*, Phys. Lett. **B563**, 23 (2003), hep-ex/0302002.
- [29] H. O. Back *et al.*, JETP Lett. **78**, 261 (2003).
- [30] Borexino, H. O. Back *et al.*, Eur. Phys. J. **C37**, 421 (2004), hep-ph/0406252.
- [31] Borexino, M. Balata *et al.*, Eur. Phys. J. **C47**, 21 (2006), hep-ex/0602027.
- [32] H. Back *et al.*, Phys. Rev. **C74**, 045805 (2006).
- [33] D. Franco, Doctor Thesis, Universita degli Studi di Milano.studi, February 2005 .
- [34] Borexino Collaboration, Phys. Lett. **B658**, 101 (2008), arXiv:0708.2251 [astro-ph].
- [35] R. Horvat and K. Pisk, Phys. Rev. **D38**, 1325 (1988).
- [36] Super-Kamiokande, D. W. Liu, Int. J. Mod. Phys. **A20**, 3110 (2005).

- [37] G. Fiorentini, M. Lissia, and F. Mantovani, *Phys. Rept.* **453**, 117 (2007), arXiv:0707.3203 [physics.geo-ph].
- [38] L. Cadonati, F. P. Calaprice, and M. C. Chen, *Astropart. Phys.* **16**, 361 (2002), hep-ph/0012082.
- [39] OPERA, R. Acquafredda *et al.*, *New J. Phys.* **8**, 303 (2006), hep-ex/0611023.
- [40] V. D. Barger *et al.*, *Phys. Rev.* **D65**, 053016 (2002), hep-ph/0110393.
- [41] OPERA, R. Zimmermann, *Acta Phys. Polon.* **B37**, 1947 (2006), physics/0604101.
- [42] ICARUS, A. Badertscher, *Nucl. Instrum. Meth.* **A535**, 129 (2004).
- [43] Princeton University, Internal meeting of the Borexino collaboration, July 2007.
- [44] M. Pallavicini, Internal note within the Borexino collaboration, July 2007.
- [45] The ROOT System, <http://root.cern.ch/>.
- [46] M. Wurm, Provided internally in the Borexino collaboration; date of version: November 2007.
- [47] T. Hagner, Doctor Thesis, Technische Universitaet Muenchen, 2000 .
- [48] G. Imbriani *et al.*, *Astron. Astrophys.* **420**, 625 (2004), astro-ph/0403071.
- [49] C. Galbiati *et al.*, *Phys. Rev.* **C71**, 055805 (2005), hep-ph/0411002.
- [50] O. Smirnov, Internal analysis within the Borexino collaboration, February 2008.
- [51] The FLUKA Code, <http://www.fluka.org/>.
- [52] M. Deutsch, "Proposal for a Cosmic Ray Detection System for the Borexino Solar Neutrino Experiment", Massachusetts, 2008.
- [53] I. Machulin, Internal analysis within the Borexino collaboration, October 2007.
- [54] A. Razzetto *et al.*, Internal studies on Borexino's capability to detect muon-induced neutrons, July 2007.
- [55] A. Chavarria *et al.*, Internal studies on Borexino's capability to detect muon-induced neutrons, July 2007.

Acknowledgments

Zu allererst möchte ich Herrn Prof. Franz von Feilitzsch danken, der mich an seinem Lehrstuhl herzlich willkommen geheißen hat, und mir diese Diplomarbeit erst ermöglichte.

Des Weiteren gilt mein Dank Prof. Lothar Oberauer für das Stellen dieses Diplomarbeitsthemas. Es war sehr spannend, in der ereignisreichen Anfangsphase der Datennahme von Borexino dabei zu sein. Dem Detektor so manches Geheimnis zu entlocken hat mir sehr viel Spaß gemacht. Ich möchte Lothar Oberauer auch dafür danken, dass er immer ein offenes Ohr für wissenschaftliche Fragenstellungen hatte, noch viel mehr aber habe ich die privaten Gespräche genossen.

Im Besonderen möchte ich mich bei meinen Bürokollegen bedanken: Teresa Marrodán Undagiotia, Michael Wurm, Jürgen Winter und Timo Lewke. Die Zusammenarbeit mit ihnen hat mir sehr viel Freude bereitet. Nicht nur die gegenseitige Unterstützung war hervorragend - sei es nun die Diskussion über theoretische Modelle oder auch nur die Hilfe bei Computerproblemen - sondern auch privat schätze ich sie sehr. Besonderer Dank gilt ihnen auch für ihre freundschaftliche Hilfe beim Erstellen dieser Diplomarbeit.

Ich danke allen Mitgliedern des E15 Lehrstuhls für die angenehme Atmosphäre und die Hilfsbereitschaft. Ich habe mich im vergangenen Jahr dieser Diplomarbeit an diesem Lehrstuhl sehr wohl gefühlt.

Ich möchte mich auch bei den Mitgliedern der Borexino Kollaboration für die gute Zusammenarbeit bedanken. Besonderer Dank gilt Davide D'Angelo, der sich immer wieder die Zeit genommen hat, Fragen zu dem Experiment zu beantworten.

Mein größter Dank gilt meiner Familie, auf die ich mich immer bedingungslos verlassen konnte. Vor allem danke ich meinen Eltern, die mich in der Wahl einer wissenschaftlichen Laufbahn bestärkt und stets unterstützt haben.